Progress in DNP Theory and Hardware

by

Anniek van der Drift, Dipl. Phys.

Thesis submitted to the University of Nottingham
for the degree of Doctor of Philosophy

July 2012

To my family

Abstract

DYNAMIC NUCLEAR POLARISATION is a technique that allows one to increase the signal-to-noise ratio in an NMR experiment substantially, by transferring the inherently larger electron polarisation to the nuclei. Quantum mechanical models of this effect have thus far been limited to the description of only a few nuclei. This is due to the exponential scaling of the matrices involved in the description of the system. In this thesis methods of reducing the state space needed to accurately describe the simulation of solid effect DNP were explored and tested. Krylov Bogoliubov averaging has been used to remove high frequency oscillations from the system Hamiltonian and confine the trajectory of the dynamics to the zero quantum coherence subspace. Truncation of the basis spanning the Liouville space to low spin correlation orders has been tested and a condition for a minimum truncation level was found. A strategy based on a projection method, which allows one to describe the spin polarisation transient with multi-exponential functions, is introduced. This results in a linear scaling of the propagator with the number of spins. The influence of the parameters involved in the solid effect on the dynamics of the polarisation build up is discussed.

The second part of this thesis is concerned with a novel approach to detecting fast molecular dynamics with the use of multiple RF receive and transmit coils. A proof of principle probe with two decoupled RF coils is presented, as well as a field map based shimming strategy and fast 2D data acquired with the probe. Lastly a probe with six RF coils, based on the design of the dual coil probe, will be presented, and initial data shown. The potential for using this probe in hyper-polarisation experiments for protein binding and folding studies will be discussed.

Contents

Introduction

In the past decades Nuclear Magnetic Resonance (NMR) spectroscopy has become a versatile tool used in a wide range of areas, including chemistry, material science, and biomedical research. It enables to measure molecular properties such as inter-nuclear distances or torsion angles between bonds, diffusion constants, correlation times and more.

A great advantage of NMR over other molecular structure determination methods is that it is non-invasive, hence the molecules can be studied in their natural environment.

One drawback is the inherently low signal-to-noise ratio (SNR) due to the small Boltzmann factor of the nuclei. This is aggravated when the experiment is performed on NMR active nuclei of low natural abundance and gyromagnetic ratio, like the biologically relevant ^{13}C and ^{15}N isotopes, or when limited sample volumes are available, as is often the case for larger proteins in biomedical research.

Dynamic Nuclear Polarisation (DNP) is one strategy to overcome this limitation. Using DNP, the nuclear signal can be greatly enhanced by doping the sample with paramagnetic impurities, such as electrons. The intrinsically larger electron polarisation is exploited by transferring it to the nuclei, a step which is driven by microwave irradiation. This makes it possible to achieve a signal enhancement of theoretically up to 660 for ^{1}H nuclei, which can become even larger depending on the polarisation strategy.

In chapter 1 a brief introduction to the principles of NMR will be given, followed by an overview of DNP theory and different polarisation strategies in chapter 2.

The polarisation step of the DNP-NMR experiment is rather time consuming, its time scale is on the same order as the nuclear relaxation time T_1, which can be up to hours for a cooled solid state sample. Hence it is desirable to optimise this stage to yield the largest polarisation in the shortest time possible. Currently DNP experiments are largely carried out in the continuous wave fashion, where the microwave irradiation is constantly on and set to the same frequency. The polarisation transfer could be accelerated by implementing suitable pulse sequences incorporating field modulations and phase changes. To devise such sequences, the availability of a quantum mechanical theoretical model of DNP is paramount, whereas the description of DNP in the past has been based on a thermodynamical approach.

Applying the full quantum mechanical treatment is challenging as the matrices needed to describe the interactions within the system scale with 4^N, N being the number of nuclei considered plus the electron. This quickly yields unmanageable matrix sizes and long processing times. Simulations on a desktop computer with 8 GB RAM are restricted to six nuclei and one electron, the processing of which takes around 26 hours. Aside from time being the practical issue, in order to make the picture more realistic more spins have to be included.

In chapter 3 three methods are presented, that greatly reduce the operator size necessary to accurately describe the spin system. Coming back to the above example of six nuclei and one electron, the two first methods reduce the operator size by a factor of 50 which results in a speed up of the processing time by a factor of around 3000. This is achieved by using Krylov-Bogoliubov averaging theory as well as truncation of the basis of the operators describing the behaviour of the spin system. For ^{13}C nuclei with their lower gyromagnetic ratio, the interactions scale more favourably with regard to the matrix size re-

duction techniques mentioned above, hence it is now possible to simulate up to 25 ^{13}C nuclei and one electron within 26 hours as well as fewer nuclei on a much faster time scale than before possible.

At the end of chapter 3 the performance of a new strategy will be tested, which enables to reduce dimension of the state space even more dramatically to the size N, where N is the number of spins involved in the simulation. This is based on a projection method which results in a multi-exponential description of the polarisation build up curves of the nuclei. Conditions for the validity of the method as well as error analysis will be shown.

The second part of this thesis is concerned with a novel approach to detecting fast molecular dynamics. Usually the repetition of an experiment is limited by the relaxation time required for the sample to return to thermal equilibrium, a time characterised by T_1. As this can be on the order of seconds for liquid state NMR it is impossible to observe faster protein dynamics in this way. In chapter 4 the feasibility of using more than just one radio frequency (RF) coil to acquire spectroscopic data from various positions of the sample is explored. With the availability of more than one RF coil, the experiment can be carried out in an arrayed fashion, avoiding having to wait for one experiment to finish before the next one is started. A prototype with two decoupled RF coils will be presented, as well as shimming strategies and fast 2D data acquired with the prototype. Additionally initial data from a six coil probe-head, developed in collaboration with Bruker, will be shown. The possibility to combine this approach with DNP in order to utilise more of the polarised sample as well as the potential for using this technique in protein binding and folding studies will also be discussed in this chapter.

Introductory NMR theory

NMR is a technique which is routinely used for sample analysis in chemistry, biology and medicine. It relies on the manipulation of the intrinsic angular momentum (spin) of the atomic nuclei in a magnetic field, using appropriate RF transmitters and receivers. NMR signals reveal information about the electronic and nuclear environment of the observed spins. Sophisticated experiments allow to extract information like coupling strengths, distances, temperature, diffusion coefficients and more.

In the following sections an introduction into the signal origin of the NMR spectrum and useful concepts will be described. As the presence of a paramagnetic impurity such as a radical containing a free electron is important for DNP, some useful properties of the electron spin will also be discussed. A more in depth review can be found in the textbooks of M. Levitt [1], R.R. Ernst and G. Bodenhausen [2], and A.A. Abragam [3].

1.1 The nuclear spin

Spin is a quantum mechanical property that is described analogously to quantum mechanical angular momentum. The total spin of a particle is hence given

by $I^{tot} = \hbar[I(I+1)]^{\frac{1}{2}}$, where I can take integer or, unlike classical angular momentum, half integer values. A particle with spin I has then (2I+1) sub levels, which take the values $m = -I, \ldots, I$. Analogously to the case of the angular momentum, m is the azimuthal angular momentum quantum number, which indicates the projection of the total angular momentum onto the z-axis[1]. Not all nuclei possess spin, and the value of I depends on the number of protons and neutrons in the nucleus, where an uneven number of either or both results in a non-zero spin. As a consequence of having spin, the nucleus possesses a magnetic moment which interacts with the surrounding magnetic field. The magnetic moment of the nucleus is given by

$$\hat{\mu} = \gamma \hbar \hat{I} \tag{1.1.1}$$

where γ is the gyromagnetic ratio of the nucleus and $\hbar$ is the Planck constant divided by 2π. This thesis will only be concerned with spin $\frac{1}{2}$ particles, for which the allowed m are $-\frac{1}{2}$ and $\frac{1}{2}$. As the potential energy of a magnetic dipole in an external magnetic field $\vec{B}_0$ is given by

$$E = -\hat{\mu} \cdot \vec{B}_0 \tag{1.1.2}$$

there are two possible energy levels for a spin $\frac{1}{2}$ particle:

$$E = -\gamma \hbar |\vec{B}_0| m, \qquad m = [-\frac{1}{2}, \frac{1}{2}].$$

This energy level splitting, which is degenerate for $\vec{B}_0 = 0$, is called the Zeeman splitting. Transitions between the two levels can be induced by applying an electromagnetic field which matches the resonance condition

$$\Delta E = -\hbar \gamma |\vec{B}_0| = \hbar \omega. \tag{1.1.3}$$

ω is called the Larmor frequency. For nuclei, ω lies in the radio frequency range for typical high resolution NMR magnetic field strengths.

---

[1] Without loss of generality the z axis is chosen by convention.

1.2   The electron spin

Electrons possess spin analogously to the nuclear spin, with the difference that m always equals $\pm\frac{1}{2}$. As opposed to the nuclei, which are assumed to be fixed in space and have no orbital angular momentum, the electron spin is a superposition of its intrinsic spin and the orbital angular momentum. The energy difference between the two energy levels is given by

$$\Delta E = g\mu_b|\vec{B}_0|, \qquad (1.2.1)$$

where g is the Landè g factor which contains the spin and orbital angular momentum and $\mu_b = \frac{e\hbar}{2m_e}$ is the Bohr magneton. For the free electron g is isotropic and equal to 2.0023. The electron gyromagnetic ratio is obtained by comparing equation (1.1.3) and (1.2.1): $\gamma_e = \frac{g\mu_b}{\hbar}$. The Bohr magneton is a constant but the g factor is modified by the electronic environment of the free electron and can become anisotropic, which in turn provides information on the surroundings of the free electron. The electron gyromagnetic ratio has an opposite sign to most nuclei, with the exception of a few which will not be encountered in this thesis.

1.3   Spin Precession

The bulk magnetisation of a sample can be modelled as the sum of the expectation values of all contributing magnetic moments:

$$\vec{M} = \sum_i <\hat{\mu}_i>$$

Exposed to an external magnetic field the magnetisation vector experiences a torque $\vec{T} = -\vec{M} \times \vec{B}_0$ towards the lowest energy conformation, parallel to the field. With $\vec{T} = \hbar\dfrac{d\hat{I}}{dt}$ this gives a differential equation describing the motion of the magnetisation vector:

$$\frac{d}{dt}\vec{M} = \gamma\vec{M} \times \vec{B}_0. \qquad (1.3.1)$$

Transferring this equation to a coordinate system that rotates with angular frequency ω, where ω is parallel to $\vec{B}_0$ one finds:

$$\frac{d}{dt}\vec{M}_{rot} = \frac{d}{\partial t}\vec{M}_{lab} + \vec{M} \times \vec{\omega} = \vec{M} \times (\gamma\vec{B}_0 + \vec{\omega})$$

Evidently $\vec{M}$ becomes static in the rotating frame for $\vec{\omega} = -\gamma\vec{B}_0$, which in turn means that in the laboratory frame $\vec{M}$ rotates around the direction of $\vec{B}_0$ with a precession frequency $\vec{\omega} = -\gamma\vec{B}_0$, the Larmor frequency from (1.1.3). By convention the external static magnetic field is aligned with the z-axis. The magnetisation vector $\vec{M}$ can be manipulated by adding an oscillating magnetic field $\vec{B}_1$, which is perpendicular to the main external magnetic field. This is done with a coil positioned around the sample. When the magnetisation vector has been tilted into the xy-plane, the precession of $\vec{M}$ induces an electromotive force (*emf*) which is measured as a voltage across the coil proportional to $\vec{M}(0)\cos\omega t$.

1.4 Density operator formalism

Interacting spins are not sufficiently described by one magnetisation vector, so a quantum mechanical treatment has to be employed. The standard equation of motion for a particle wave function $|\psi(t)\rangle$ is the Schrödinger equation, but as NMR experiments are usually conducted on a large ensemble of spins this is not practical. Instead the density matrix formalism is used, where ensemble averages of the wave function are considered. The central limit theorem implies, that while the state of an individual spin may be uncertain, for a collection of many spins the average state may still be known to a high degree of accuracy [4]. This leads to the Liouville-von Neuman equation of motion, which describes the evolution of the ensemble average.

1.4.1   From wave function to density operator

Each wave function $|\psi(t)\rangle$ representing the state of N interacting spins can be written as a linear combination of orthonormal basis eigenfunctions:

$$|\psi(t)\rangle = \sum_{n=1}^{N} c_n |n\rangle \quad \text{and its transposed complex conjugate is: } \langle\psi(t)| = \sum_{n=1}^{N} c_n^* \langle n|.$$

The coefficients c_n, c_n^* can be found using $c_n = \langle n|\psi\rangle$ and $c_n^* = \langle\psi|n\rangle$, where $\langle a|b\rangle$ is the Dirac notation for the scalar product $\int a^* b \, dt$. Operators can be defined as $n \times n$ matrices with elements

$$Q_{mn} = \langle n|\hat{Q}|m\rangle.$$

The expectation value of the operator $\hat{Q}$ for the spin system with wave function $|\psi\rangle$ is

$$
\begin{aligned}
\langle\hat{Q}\rangle =& \langle\psi|\hat{Q}|\psi\rangle = \sum_n \sum_m c_n c_m^* \langle m|\hat{Q}|n\rangle \\
=& \sum_n \sum_m \langle n|\psi\rangle\langle\psi|m\rangle\langle m|\hat{Q}|n\rangle \\
=& \sum_n \langle n|\psi\rangle\langle\psi|\hat{Q}|n\rangle \\
=& Tr(|\psi\rangle\langle\psi|\hat{Q}).
\end{aligned}
$$

The expression $|\psi\rangle\langle\psi|$ completely describes the state of the system and gives the density operator. For a sample containing a large number of spins, the average over all the states is used and the matrix elements of the density operator are:

$$\rho_{nm} = \overline{\langle n|\psi\rangle\langle\psi|m\rangle} = \overline{c_n c_m^*} = \langle n|\hat{\rho}|m\rangle$$

and the expectation value of an operator is given by

$$\langle\hat{Q}\rangle = Tr(\hat{\rho}\hat{Q}).$$

As an example, the general state of an ensemble of non-interacting spin-$\frac{1}{2}$ particles is given by:

$$|\psi\rangle = c_\alpha|\alpha\rangle + c_\beta|\beta\rangle = c_\alpha \begin{pmatrix} 1 \\ 0 \end{pmatrix} + c_\beta \begin{pmatrix} 0 \\ 1 \end{pmatrix},$$

where $|\alpha\rangle$ and $|\beta\rangle$ are the orthonormal basis vectors of the density operator. Hence the density operator corresponding to this state is:

$$\begin{pmatrix} \overline{c_\alpha c_\alpha^*} & \overline{c_\alpha c_\beta^*} \\ \overline{c_\alpha^* c_\beta} & \overline{c_\beta c_\beta^*} \end{pmatrix}. \tag{1.4.1}$$

The state vector of N coupled spin $\frac{1}{2}$ particles can be constructed by

$$|\psi\rangle = |\psi_1\rangle \otimes |\psi_2\rangle \otimes \ldots \otimes |\psi_N\rangle$$

and hence the density operator is a $2^N \times 2^N$ matrix, given by $\overline{|\psi\rangle\langle\psi|}$.

1.4.2 Time evolution - the Liouville-von Neuman equation of motion

The equation of motion for $|\psi(t)\rangle$ is given by the Schrödinger equation:

$$-i\hbar \frac{d}{dt}|\psi(t)\rangle = \hat{\mathscr{H}}|\psi(t)\rangle, \tag{1.4.2}$$

where $\hat{\mathscr{H}}$ is the Hamiltonian operator describing the interactions within the spin system, its eigenvalues are the energy levels. Hamiltonians will be described in more detail in section 1.5. Using equation (1.4.2) and its transpose, one gets

$$\begin{aligned} \frac{d}{dt}|\psi(t)\rangle\langle\psi(t)| &= (\frac{d}{dt}|\psi(t)\rangle)\langle\psi(t)| + |\psi(t)\rangle\frac{d}{dt}\langle\psi(t)| \\ &= i\hbar(-\hat{\mathscr{H}}|\psi(t)\rangle\langle\psi(t)| + |\psi(t)\rangle\langle\psi(t)|\hat{\mathscr{H}}) \\ &= -\frac{i}{\hbar}\left[\hat{\mathscr{H}}, |\psi(t)\rangle\langle\psi(t)|\right] \end{aligned}$$

This relation is also true for linear combinations of $|\psi(t)\rangle\langle\psi(t)|$ and hence for $\hat{\rho}(t)$:

$$\frac{d}{dt}\hat{\rho}(t) = -\frac{i}{\hbar}\left[\hat{\mathscr{H}}, \hat{\rho}\right], \tag{1.4.3}$$

which is the Liouville-von Neuman equation of motion. If the Hamiltonian is time-independent, the solution to equation (1.4.3) is

$$\hat{\rho}(t) = U(t)\rho(0)U(t)^{-1} = e^{-\frac{i}{\hbar}\hat{\mathscr{H}}t}\hat{\rho}(0)e^{\frac{i}{\hbar}\hat{\mathscr{H}}t}. \tag{1.4.4}$$

For many encountered problems, if $\hat{\mathscr{H}}$ varies with time, a frame of reference can be found in which it becomes time independent. If the density operator is expressed in the eigenbasis of the Hamiltonian the off diagonal elements indicate a coherence between two states, whereas diagonal elements indicate the fractional populations of the energy levels.

It is customary in NMR to speak of energies in terms of frequencies, hence as $E = \hbar\omega$, the $\hbar$ term will be absorbed into the Hamiltonian, which then contains elements in units of angular frequency.

1.4.3 Spin operators and properties

Analogously to the classical angular momentum, spin also can be described by operators which obey the same commutation relations:

$$\left[\hat{I}_k, \hat{I}_l\right] = i\varepsilon_{klm}\hat{I}_m, \quad \text{where } k, l, m \in [x,y,z],$$

and ε_{klm} is the Levi Civita tensor. The single spin operators are given by $\hat{I}_k = \frac{1}{2}\sigma_k$, where σ_k is one of the Pauli matrices:

$$\sigma_x = \begin{pmatrix} 0 & 1 \\ 1 & 0 \end{pmatrix} \quad \sigma_y = \begin{pmatrix} 0 & -i \\ i & 0 \end{pmatrix} \quad \sigma_z = \begin{pmatrix} 1 & 0 \\ 0 & -1 \end{pmatrix}.$$

The quantum numbers m that were introduced at the start of this chapter are the eigenvalues of the operator $\hat{I}_z$, whereas $I(I+1)$ is the eigenvalue of the total angular momentum operator $\hat{I} = \hat{I}_x^2 + \hat{I}_y^2 + \hat{I}_z^2$.

The operator describing the energy of a spin-$\frac{1}{2}$ particle in a magnetic field aligned along the z axis can be expressed in terms of the spin operator $\hat{I}_z$:

$$\hat{\mathscr{H}} = -\frac{1}{2}\gamma B_0 \sigma_z = -\gamma B_0 \hat{I}_z$$

This operator is the Zeeman Hamiltonian, derived from (1.1.1) and (1.1.2). Together with the unity operator $\hat{E} = \begin{pmatrix} 1 & 0 \\ 0 & 1 \end{pmatrix}$ the operators $\hat{I}_x, \hat{I}_y$ and $\hat{I}_z$ form a complete basis, called the Cartesian basis, in which the density operator and Hamiltonians can be expressed. For a two spin-$\frac{1}{2}$ system, the Cartesian basis operators

can be constructed from Table 1.1. In general for an N-spin$\frac{1}{2}$ ensemble the basis

Table 1.1: Construction of the Cartesian two spin basis from the single spin operator.

	$\hat{E}_2$	$\hat{I}_{2x}$	$\hat{I}_{2y}$	$\hat{I}_{2z}$
$\hat{E}_1$	$\hat{E}_1 \otimes \hat{E}_2$	$\hat{E}_1 \otimes \hat{I}_{2x}$	$\hat{E}_1 \otimes \hat{I}_{2y}$	$\hat{E} \otimes \hat{I}_{2z}$
$\hat{I}_{1x}$	$\hat{I}_{1x} \otimes \hat{E}_2$	$\frac{1}{2}\sigma_{1x} \otimes \sigma_{2x}$	$\frac{1}{2}\sigma_{1x} \otimes \sigma_{2y}$	$\frac{1}{2}\sigma_{1x} \otimes \sigma_{2z}$
$\hat{I}_{1y}$	$\hat{I}_{1y} \otimes \hat{E}_2$	$\frac{1}{2}\sigma_{1y} \otimes \sigma_{2x}$	$\frac{1}{2}\sigma_{2y} \otimes \sigma_{2x}$	$\frac{1}{2}\sigma_{2y} \otimes \sigma_{2z}$
$\hat{I}_{1z}$	$\hat{I}_{1z} \otimes \hat{E}_2$	$\frac{1}{2}\sigma_{1z} \otimes \sigma_{2x}$	$\frac{1}{2}\sigma_{1z} \otimes \sigma_{2y}$	$\frac{1}{2}\sigma_{1z} \otimes \sigma_{2z}$

operators are given by [2]:

$$B_s = 2^{(q-1)} \prod_{k=1}^{N} (I_{k\alpha})^{a_{ks}},$$

where $\alpha = x, y$ or z, q is the number of operators in the product and $a_{ks} = 1$ for q of the spins and $a_{ks} = 0$ for the remaining $N - q$ spins [2]. From $\hat{I}_x$ and $\hat{I}_y$ the raising and lowering operators can be obtained, which increase or decrease the quantum number m of a particular state $|\psi\rangle$ by one:

$$\hat{I}_+ = \hat{I}_x + i\hat{I}_y = \begin{pmatrix} 0 & 1 \\ 0 & 0 \end{pmatrix} \quad \text{and} \quad \hat{I}_- = \hat{I}_x - i\hat{I}_y = \begin{pmatrix} 0 & 0 \\ 1 & 0 \end{pmatrix}.$$

For example $\hat{I}_-|\alpha\rangle = |\beta\rangle$. The operators $\hat{I}_z$, $\hat{I}_+$, $\hat{I}_-$ and $\hat{E}$ also form a complete basis for a single spin $\frac{1}{2}$, called the shift basis, which can be extended to a basis for a higher number of spins by building product operators as in Table 1.1.

1.4.4 Thermal equilibrium, spin polarisation and spin temperature

The thermal equilibrium of the undisturbed spin system is given by the Boltzmann distribution:

$$\rho_{eq} = \sum_{i=1}^{N} Z^{-1} e^{-\frac{E_i}{k_b T}},$$

where Z is the partition function of the system, k_b the Boltzmann factor and T the absolute temperature. For the spin-$\frac{1}{2}$ ensemble the thermal equilibrium density operator is hence given by

$$\rho_{eq} = Z^{-1} \begin{pmatrix} \exp\left(-\frac{\hbar\gamma B_0}{2k_b T}\right) & 0 \\ 0 & \exp\left(\frac{\hbar\gamma B_0}{2k_b T}\right) \end{pmatrix},$$

with

$$Z = \exp\left(\frac{\hbar\gamma B_0}{2k_b T}\right) + \exp\left(-\frac{\hbar\gamma B_0}{2k_b T}\right).$$

A high temperature approximation can be made when the Zeeman energy is much smaller than the thermal energy, so when $\frac{\hbar\gamma B_0}{k_b T} \ll 1$. This is the case for nuclei even down to temperatures of a few Kelvin. The exponential function can then be expanded in a Taylor series and all higher order terms after the second are neglected. Then the equilibrium density operator is

$$\rho_{eq} = \frac{1}{2}\left(\hat{E} + \frac{\hbar\gamma B_0}{k_b T}\hat{I}_z\right). \tag{1.4.5}$$

Even though it was indicated in section 1.3 that all spins precess at the characteristic Larmor frequency, this is not evident from the equilibrium density operator as the precessing spins do not possess phase coherence (the off diagonal elements are averaged to zero). Phase coherence can be induced by applying a time varying magnetic field perpendicular to the main magnetic field, as will be shown in section 1.8.

The polarisation of a spin system is given by the fractional differences of the

populations, so the equilibrium polarisation for a spin-$\frac{1}{2}$ ensemble is

$$P_0 = Z^{-1} \left[\exp\left(\frac{\hbar\gamma B_0}{2k_b T}\right) - \exp\left(-\frac{\hbar\gamma B_0}{2k_b T}\right) \right] = \tanh\left(\frac{\hbar\gamma B_0}{2k_b T}\right). \qquad (1.4.6)$$

The higher the polarisation, the larger the initial magnetisation $M_0 = N\mu P_0 = \frac{N}{2}\gamma\hbar P_0$ and hence the signal to noise ratio (SNR), which is proportional to

$$SNR \propto M_0 \eta \sqrt{\frac{Q\omega V_c}{T_c}}. \qquad (1.4.7)$$

Here η is the filling factor of the coil, Q is the quality factor of the coil, V_c the volume of sample, and T_c the temperature of the coil. From the selection of thermal polarisation values of ^{1}H, ^{13}C and electrons given in Table 1.2 it can be seen that NMR is inherently insensitive, which is due to the small Boltzmann factor $\frac{\hbar\gamma B_0}{k_b T}$.

Table 1.2: Equilibrium spin polarisations at B_0=9.4 Tesla for ^{1}H and ^{13}C nuclei as well as electrons.

Temperature [K]	$P_0(^1H)$	$P_0(^{13}C)$	$P_0(e^-)$
300	9.7e-5	8.1e-6	2.1e-2
1	9.7e-3	2.4e-3	1

It can be seen from equation (1.4.6) and Table 1.2 that the spin polarisation is temperature dependent. One can assign a spin temperature T_S to the system, which is equal to the external temperature T for a spin system, that is not polarised by means other than changing the temperature T or the external magnetic field B_0. If however the polarisation is increased, for example by DNP, the temperature at which the same population difference would occur without DNP is much lower than the external temperature T of the sample. Then the spin temperature T_S is smaller than the sample temperature T. The spin temperature can also become larger than the sample temperature and even negative, for example

when the populations are affected using RF pulses. The negative spin temperature occurs for an RF inversion pulse. Instead of using T_S, the inverse spin temperature $\beta = (k_b T_S)^{-1}$ is often used.

1.5 Hamiltonians

Hamiltonians are the generators of time evolution [5]: it could be seen in section 1.4.2 that the density operator undergoes changes under the influence of a Hamiltonian operator. Hamiltonians are Hermitian operators that describe the interactions in the system, such as the interaction of the spin with the external magnetic field or with other spins. The spectrum of a sample is uniquely determined by the Hamiltonians involved and hence information on coupling strengths and distances can be deduced.

1.5.1 Zeeman Hamiltonian

Nuclear spins solely subjected to an external magnetic field evolve under the aforementioned Zeeman Hamiltonian

$$\hat{\mathscr{H}}_Z = -\gamma B_0 \hat{I}_z = -\omega \hat{I}_z.$$

For ^{1}H nuclei $\gamma = 42.57$ MHz/T, and for ^{13}C $\gamma = 10.71$ MHz/T. Electrons have a much larger gyromagnetic ratio due to their small mass, as well as an opposite sign which stems from the negative charge of the electron. For a free electron the gyromagnetic ratio is $\gamma_e = -g\mu_b = -28.03$ GHz/T. The electronic Zeeman interaction can be anisotropic, in which case instead of one g factor the tensor **g** has to be used:

$$\hat{\mathscr{H}}_Z = -\mathbf{g}\mu_b B_0 \hat{S}_z.$$

In order to avoid confusion, the electron spin operators are denoted as $\hat{S}$.

1.5.2 Chemical shift

In liquid state NMR the molecules are tumbling rapidly on a time scale much faster than the acquisition time scale. Hence orientation dependent short distance interactions, which will be introduced in section 1.5.5, are averaged out and only isotropic contributions remain. The most dominant interaction in liquid state is the chemical shift. The nuclear Larmor frequency is modified by the surrounding electron cloud of the atom. The external magnetic field induces circular motion of the electrons in their orbitals, resulting in a small shielding magnetic field in the opposite direction to the external field (Lenz rule). Hence the resonance frequency is shifted by the isotropic shielding constant σ.

$$\omega = -\gamma(1 - \sigma)B_0$$

As the electron cloud in a molecule is dependent on the electro-negativity of the involved nuclei, the chemical shift is one indicator of the components in the molecule. In order to enable comparison of data acquired at different external magnetic fields a field independent expression for the chemical shift, measured in parts per million (ppm), exists. It is given by

$$\delta = \frac{\omega - \omega_{ref}}{\omega_{ref}}, \tag{1.5.1}$$

where ω_{ref} is the resonance frequency of a reference compound, commonly Tetramethylsilane $(CH_3)_4$ Si.

1.5.3 J-coupling

Another important interaction in the liquid state is J-coupling. This is an indirect interaction of neighbouring spins via their electronic environment. For an s-type electron orbital there is a non-vanishing probability density at the nucleus, known as the Fermi contact term. The electron spin state therefore has an influence on the nuclear spin state. Consider a nuclear spin pair I_A and I_B covalently bonded via electrons with spins S_A and S_B. I_A is aligned either parallel

or anti-parallel to the external magnetic field and so the magnetic moment of its electrons will align accordingly either parallel or anti-parallel to I_A. Following the Pauli exclusion principle the second electronic term will align anti-parallel to S_A. The two possible configurations of I_B now have two different energies, resulting in peak splitting in the spectrum. The strength of the J-coupling is field independent. In liquids the rapid molecular tumbling averages out any directional information so J is a scalar. The Hamiltonian for J-coupling is

$$\hat{\mathscr{H}}_J = 2\pi J \hat{I}_{1z} \hat{I}_{2z},$$

where J is the coupling strength in Hz.

1.5.4   RF and microwave Hamiltonian

Transitions between energy levels levels can be introduced by applying a time varying field perpendicular to the main magnetic field, that matches the resonance condition. Depending on whether the spin species concerned are electrons or nuclei, the resonance condition lies in the microwave or radio frequency range respectively for magnetic fields of several Tesla. The nuclear RF Hamiltonian is given by

$$\hat{\mathscr{H}}_{rf} = \omega_1 e^{-i\omega_{irr}\hat{I}_z t} \hat{I}_x e^{i\omega_{irr}\hat{I}_z t}, \tag{1.5.2}$$

where ω_1 is the strength of the applied field and ω_{irr} is the irradiation frequency. Without loss of generality the $\vec{B}_1$ field in the given Hamiltonian is aligned along the x axis, but this can easily be changed by replacing $\hat{I}_x$ with $\hat{I}_y$ or a superposition of both, if necessary. The structure of the microwave Hamiltonian is exactly the same, just the irradiation frequency has to be changed.

1.5.5 Orientation dependent spin-spin interaction Hamiltonians

In the solid state the direction dependency of the interaction between two spins is conserved. As the DNP effect that is encountered in this thesis takes place in the solid state, it is important to introduce the following two interactions, which average out for liquid state experiments.

Hyperfine interaction

The first important interaction is that of the nuclei with free electron spins such as free radicals. This is the hyperfine interaction and the Hamiltonian for one electron and N nuclei is

$$\hat{\mathscr{H}}_{hfi} = \frac{1}{2} \sum_k^N \frac{\gamma_I \gamma_S}{r_k^3} \left[\hat{I}_k \cdot \hat{S} - 3(\hat{I}_k \cdot \hat{r}_k)(\hat{S} \cdot \hat{r}_k) \right],$$

where r_k is the connection vector between the kth nucleus and the electron. This can be brought into the form of the 'dipolar alphabet' [6]

$$\hat{\mathscr{H}}_{hfi} = \sum_k^N \frac{\gamma_I \gamma_S}{r_k^3} \left(a_k + b_k + c_k + d_k + e_k + f_k \right),$$

where

$$a_k = \hat{I}_{kz} \hat{S}_z (1 - 3\cos^2 \theta_k)$$

$$b_k = -\frac{1}{4} \left[\hat{I}_{k-} \hat{S}_+ + \hat{I}_{k+} \hat{S}_- \right] (1 - 3\cos^2 \theta_k)$$

$$c_k = -\frac{3}{2} \left[\hat{I}_{k+} \hat{S}_z + \hat{I}_{kz} \hat{S}_+ \right] \sin \theta_k \cos \theta_k e^{-i\phi_k} \qquad (1.5.3)$$

$$d_k = -\frac{3}{2} \left[\hat{I}_{k-} \hat{S}_z + \hat{I}_{kz} \hat{S}_- \right] \sin \theta_k \cos \theta_k e^{i\phi_k}$$

$$e_k = -\frac{3}{4} \hat{I}_{k+} \hat{S}_+ \sin^2 \theta_k e^{-2i\phi_k}$$

$$f_k = -\frac{3}{4} \hat{I}_{k-} \hat{S}_- \sin^2 \theta_k e^{2i\phi_k},$$

where θ_k is the angle between the z-axis and r_k and ϕ_k the polar angle between the x-axis and r_k. At high magnetic fields the electron Zeeman interaction is

much larger than the nuclear terms, hence first order perturbation theory can applied and only the secular parts with respect to the electron Zeeman interaction need to be kept. These secular terms are the ones that commute with the electron Zeeman Hamiltonian, so the hyperfine interaction Hamiltonian reduces to:

$$\hat{\mathscr{H}}'_{hfi} = \sum_k^N A_k \hat{I}_{kz} \hat{S}_z + B_{k+} \hat{I}_{k+} \hat{S}_z + B_{k-} \hat{I}_{k-} \hat{S}_z,$$

with the constants

$$A_k = \frac{\gamma_I \gamma_S}{r_k^3} (1 - 3 \cos^2 \theta_k) \tag{1.5.4}$$

and

$$B_{k\pm} = -\frac{3}{2} \frac{\gamma_I \gamma_S}{r_k^3} \sin \theta_k \cos \theta_k e^{\mp i \phi_k}.$$

The term containing A_k is responsible for level splitting and the one containing $B_{k\pm}$ indicates how well the levels are mixed. It is evident that $B_{k-} = B_{k+}^*$. From now on the truncated hyperfine Hamiltonian will be used and the prime will be dropped. The modulation of the interaction constants A_k and $B_{k\pm}$ with the angle θ is shown in figure 1.1. The black lines, which indicate where the interaction constant A_k is zero, mark the so called magic angles.
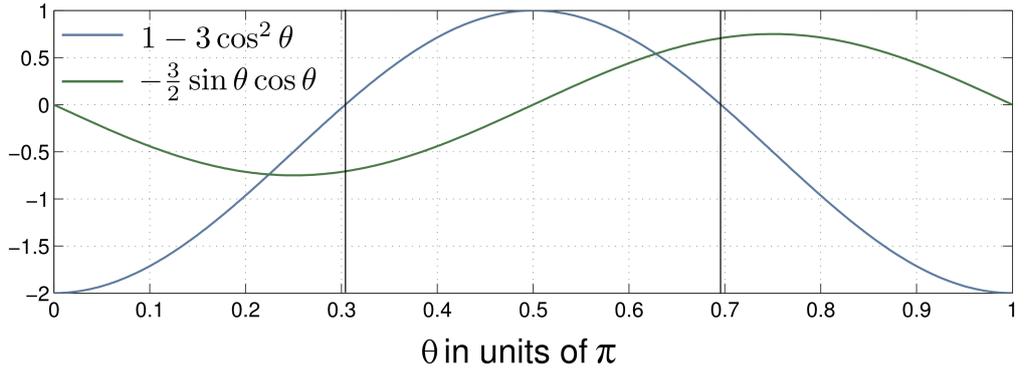
Figure 1.1: Modulation of the hyperfine interaction constants A_k and $B_{k\pm}$ with the angle θ.

Nuclear dipole-dipole coupling

The second important interaction, the nuclear dipole-dipole interaction, has the same structure as the hyperfine Hamiltonian:

$$\hat{\mathscr{H}}_{DD} = \frac{1}{2}\sum_{i,j}^{N} \frac{\gamma_I^2}{r_{ij}^3} \left[\hat{I}_i \cdot \hat{I}_j - 3(\hat{I}_i \cdot \hat{r}_{ij})(\hat{I}_j \cdot \hat{r}_{ij})\right],$$

where $\hat{r}_{ij}$ is the internuclear distance unit vector. Again a secular approximation can be made, as the nuclear Zeeman interaction is much larger than the dipolar terms. As a result all terms that do not commute with the nuclear Zeeman Hamiltonian can be neglected. The truncated Hamiltonian is then

$$\hat{\mathscr{H}}_{DD}' = \frac{1}{2}\sum_{i,j}^{N} d_{ij} \left[2\hat{I}_{iz}\hat{I}_{jz} - \frac{1}{2}\left(\hat{I}_{i+}\hat{I}_{j-} + \hat{I}_{i-}\hat{I}_{j+}\right)\right], \tag{1.5.5}$$

where $d_{ij} = \frac{1}{2}\gamma_I^2(1 - 3\cos^2\theta_{ij})r_{ij}^{-3}$ is the dipolar coupling strength between spin $\hat{I}_i$ and $\hat{I}_j$ in Hertz and θ_{ij} is the angle between the z axis and the internuclear distance vector $\hat{r}_{ij}$. Again the prime will be dropped and from now on the dipolar Hamiltonian from equation (1.5.5) will be used.

1.6 Typical interaction strengths

It is instructive to consider the typical strengths of the interactions mentioned before. In Table 1.3 an overview of typical values for ^{1}H nuclei can be found, where for the field dependent interactions a magnetic field on the order of several Tesla is assumed. ^{13}C nuclei have an approximately four times smaller gyromagnetic ratio, resulting in four times smaller hyperfine interaction constants with respect to protons, a four times smaller Larmor frequency as well as a sixteen times smaller nuclear dipole interaction.

Table 1.3: Typical numerical values for interaction strengths.

Interaction type	Typical range of values in Hz
J coupling	$10^0 - 10^2$
Nuclear dipole dipole coupling	$10^0 - 10^3$
Hyperfine interaction	$10^3 - 10^6$
Nuclear Zeeman	10^8
Electron Zeeman	10^{10}

1.7 Interaction Representation of Hamiltonians

For Hamiltonians which contain a strong $\hat{\mathscr{H}}_0$ and comparatively weak interaction terms $\hat{\mathscr{H}}_1$ one can remove the effect of the strong interaction by a transformation into an interaction or rotating frame:

$$\hat{\mathscr{H}}^T(t) = e^{i\hat{\mathscr{H}}_0 t}\hat{\mathscr{H}}_1(t)e^{-i\hat{\mathscr{H}}_0 t}, \tag{1.7.1}$$

where the index T indicates a transformation into an interaction frame. The density matrix also has to be transformed into this frame:

$$\hat{\rho}^T(t) = e^{i\hat{\mathscr{H}}_0 t}\hat{\rho}(t)e^{-i\hat{\mathscr{H}}_0 t} \qquad \frac{\partial \hat{\rho}^T(t)}{\partial t} = -i\left[\hat{\mathscr{H}}^T(t), \hat{\rho}^T(t)\right].$$

This has the effect that the terms in the new $\hat{\mathscr{H}}^T(t)$ are much smaller, which, as the time step that is necessary to accurately calculate $\hat{\rho}(t)$ is on the order of $\frac{1}{||\mathscr{H}||}$, brings computational advantages. Additionally, in most cases it is possible to remove explicit time dependence of a Hamiltonian by choosing the correct rotating frame.

If the Hamiltonian is written in terms of irreducible tensor operators $\hat{T}_{lm}$ (see appendix A) one can transform it using the following commutation relation [7]:

$$\left[\hat{I}_z, \hat{T}_{lm}\right] = m\hat{T}_{lm}, \tag{1.7.2}$$

which results in the interaction frame transformation:

$$e^{i\omega\hat{I}_z t}\hat{T}_{lm}e^{-i\omega\hat{I}_z t} = e^{-im\omega t}\hat{T}_{lm} \tag{1.7.3}$$

A few examples will be shown in the next sections.

1.7.1 The Microwave Hamiltonian in the Electron Interaction frame

The microwave Hamiltonian in the lab frame is given by:

$$\hat{\mathscr{H}}_{mw} = \omega_1 e^{-i\omega_{\mu w}\hat{S}_z t}\hat{S}_x e^{i\omega_{\mu w}\hat{S}_z t} = \frac{\omega_1}{2}e^{-i\omega_{\mu w}\hat{S}_z t}\left(\hat{S}_- + \hat{S}_+\right)e^{i\omega_{\mu w}\hat{S}_z t}, \tag{1.7.4}$$

where ω_1 is the microwave field strength and $\omega_{\mu w}$ the irradiation frequency. Using (1.7.3) one can rewrite (1.7.4) as:

$$\hat{\mathscr{H}}_{mw} = \frac{\omega_1}{2}\left(e^{-i\omega_{\mu w}t}\hat{S}_- + e^{i\omega_{\mu w}t}\hat{S}_+\right)$$

The transformation into the electron Zeeman interaction frame $\mathscr{H}_0 = \omega_S\hat{S}_z$, where ω_S is the electron Larmor frequency, gives:

$$\left[\hat{S}_z,\hat{S}_-\right] = \sqrt{2}\left[\hat{S}_z,\hat{T}_{1-1}\right] = -\sqrt{2}\hat{T}_{1-1} = -\hat{S}_- \rightarrow e^{i\omega_S\hat{S}_z t}\,\hat{S}_-\,e^{-i\omega_S\hat{S}_z t} = e^{i\omega_S t}\hat{S}_-$$

$$\left[\hat{S}_z,\hat{S}_+\right] = \sqrt{2}\left[\hat{S}_z,\hat{T}_{11}\right] = -\sqrt{2}\hat{T}_{11} = \hat{S}_+ \rightarrow e^{i\omega_S\hat{S}_z t}\hat{S}_+e^{-i\omega_S\hat{S}_z t} = e^{-i\omega_S t}\hat{S}_+$$

so

$$\hat{\mathscr{H}}^T_{mw} = \frac{\omega_1}{2}\left(e^{i\Delta t}\hat{S}_- + e^{-i\Delta t}\hat{S}_+\right), \quad \Delta = \omega_S - \omega_{\mu w}. \tag{1.7.5}$$

If $\omega_{\mu w} = \omega_S$ the offset becomes zero and one obtains the microwave term $\hat{\mathscr{H}}^T_{mw} = \frac{\omega_1}{2}\left(\hat{S}_- + \hat{S}_+\right) = \omega_1\hat{S}_x$, which appears to be static in the rotating frame.

1.7.2 Pseudo-secular Hyperfine Interaction Hamiltonian in the doubly rotating frame

The pseudo-secular[2] hyperfine interaction Hamiltonian $\hat{\mathscr{H}}_{hfi}$ is already secular with respect to the electron Zeeman term, so one only has to calculate the transformation into the nuclear rotating frame.

$$\hat{\mathscr{H}}_{hfi} = \sum_k^N \left[A_k \hat{I}_{kz} \hat{S}_z + \frac{1}{2} \left(B_{k-} \hat{I}_{k-} + B_{k+} \hat{I}_{k+} \right) \hat{S}_z \right].$$

Transformation into the nuclear Zeeman frame $\hat{\mathscr{H}}_0 = \omega_I \hat{I}_z$ gives analogously to (1.7.5):

$$\hat{\mathscr{H}}_{hfi}^T = \sum_k^N \left[A_k \hat{I}_{kz} \hat{S}_z + \frac{1}{2} \left(e^{i\omega_I t} B_{k-} \hat{I}_{k-} + e^{-i\omega_I t} B_{k+} \hat{I}_{k+} \right) \right] \hat{S}_z.$$

These examples will be encountered again in chapter 3.

1.8 The NMR experiment

The starting point, the equilibrium density operator, is given by equation (1.4.5). In order to simplify calculations, the numerical factors and the unity matrix are neglected and $\hat{\rho}_{eq}$ is taken to be $\hat{I}_z$. In order to bring the system out of equilibrium an RF pulse has to be applied. In the rotating frame the density matrix after an on resonant $90°$ pulse of duration τ is given by:

$$\hat{\rho}(\tau) = U_{rf}(\tau) \hat{\rho}_{eq} U_{rf}^{-1}(\tau) = e^{-i\frac{\pi}{2}\hat{I}_x} \hat{I}_z e^{i\frac{\pi}{2}\hat{I}_x} = -\hat{I}_y,$$

where the RF field strength ω_1 has been chosen in such a way, that the flip angle of the magnetisation is $\beta = \omega_1 \tau = \frac{\pi}{2}$. In the laboratory frame the spins precess with the Larmor frequency in the xy plane, which induces an *emf* in the detector coil. The spectrometer mixes the recorded signal with a carrier frequency ω_{ref}

---

[2]Secular with respect to the electron Zeeman Hamiltonian

close to the Larmor frequency, in order to enable detection an an analogue digital converter. The signal is then given by

$$\hat{\rho}(t) = U_Z(t)\hat{\rho}(\tau)U_Z^{-1}(t) = -e^{-i\Omega\hat{I}_z t}\hat{I}_y e^{i\Omega\hat{I}_z t} = -\hat{I}_y\cos(\Omega t) + \hat{I}_x\sin(\Omega t) \qquad (t > \tau),$$

with $\Omega = (\omega - \omega_{ref})$. Fourier transformation yields the spectrum with the frequencies that are characteristic for the molecule. This is illustrated in figure 1.2, where a spectrum of Ethanol is displayed. On the left one can see the signal induced in the receive coil, the free induction decay (FID). Due to the presence of more than one resonance frequency in the sample, modulations of the amplitude are visible. On the right the Fourier transform displays the various chemical shift frequencies and J coupling splittings.
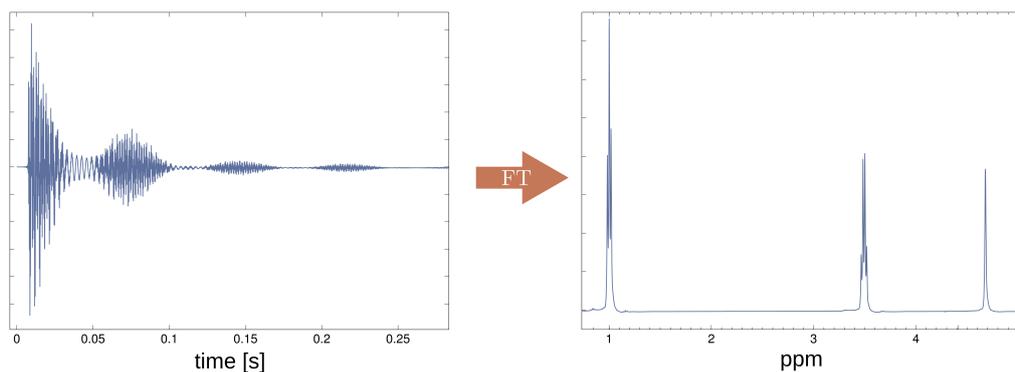
Figure 1.2: FID and resulting spectrum of Ethanol.

Bloch equations with relaxation

The excited spins will eventually return to the thermal equilibrium due to relaxation processes. The simplest way to describe this is by employing the magnetisation vector model introduced in section 1.3 for uncoupled spins. Equation (1.3.1) is modified by introducing a relaxation matrix which enables the return of the magnetisation vector to the initial position $\vec{M}_0$.:

$$\frac{d}{dt}\vec{M} = \gamma\vec{M}(t) \times \vec{B}(t) - \hat{R}(\vec{M}(t) - \vec{M}_0),$$

23

with

$$\hat{R} = \begin{pmatrix} \frac{1}{T_1} & 0 & 0 \\ 0 & \frac{1}{T_2} & 0 \\ 0 & 0 & \frac{1}{T_2} \end{pmatrix}. \qquad (1.8.1)$$

$\frac{1}{T_1}$ is the longitudinal relaxation rate which indicates how fast the thermal equilibrium z-magnetisation is restored. Longitudinal relaxation is induced by fluctuations of the surrounding magnetic field at the Larmor frequency, that have a component in the xy plane. The transverse relaxation rate $\frac{1}{T_2}$ indicates how fast the component of the magnetisation vector in the xy plane decays. This is caused by a loss of coherence of the spins due to fluctuations of the surrounding magnetic field with a component in the z direction. These fluctuations cause some spins to precess faster and some slower, resulting in an overall dephasing of the spins and hence loss of coherence. $\vec{B}(t)$ in equation (1.8.1) is now the sum of the external static magnetic field $\vec{B}_0$ and the time varying excitatory magnetic field $\vec{B}_1$. The separate x y and z components of equation 1.8.1 are well known as the Bloch equations.

An important source of relaxation in the liquid state is molecular tumbling, where the dipolar interaction between nuclei acts as the mediator of the resulting fluctuations in the magnetic field. In the solid state the rapid fluctuations of the electronic spin state are felt by the nuclei via the hyperfine interaction, which as a result are a main cause of relaxation for the nuclei in this case [3].

1.9 Relaxation and the Liouville space

The Bloch equations (1.8.1) are only valid for uncoupled spin systems, for coupled spins a more in depth treatment has to be employed. For a full description of relaxation processes one would have to include the surrounding particles that are the origin of local magnetic field fluctuations, such as phonons and electrons, in the density operator. As this leads to a very large state space, and

hence a large density operator, this is not practical. Instead, a treatment that is called semi-classical by Ernst and Bodenhausen [2], where the influence of the surroundings is represented by a randomly fluctuating term, is useful for most applications. It is based on defining a Hamiltonian that represents the small random fluctuations, and then perturbation theory is applied. An important concept for the description of incoherent processes such as relaxation is the Liouville space, the adjoint map to the Hilbert space in which the theory presented up to this point has resided. Hilbert space in general is a vector space which has a metric defined on it. The Liouville space is spanned by the 2^N basis states of the Hilbert space [8]. In Liouville space the density operator is represented by a vector. Liouville space operators, also called superoperators and defined from Hamiltonians, are acting on it to generate time evolution. One advantage of making the transition to the Liouville space is: The commutator in the equation of motion (1.4.3) is replaced by a left hand multiplication of the initial density operator with a superoperator. This in turn means that the solution is given only by a left hand multiplication with a propagator, very much analogous to the solution to the Schrödinger equation. Additionally, commutators play a role in the Redfield relaxation theory that will be introduced in this section, which can thus be removed by a transition to the Liouville space.

1.9.1 Liouville space

Liouville space operators are derived from Hilbert space ('normal') operators by

$$\hat{\hat{I}}_k = \left[\hat{I}_k, \hat{E}\right] = \hat{I}_k \otimes \hat{E} - \hat{E} \otimes \hat{I}_k.$$

The double hat above the operator indicates a Liouville space operator. The Hamiltonian in the Liouville space is constructed in the same way. The dimension of the new superoperators and Hamiltonians is now 4^N as opposed to 2^N, which is a large penalty in computational terms but in order to describe relax-

ation behaviour of coupled spins, the transition to Liouville space is necessary. The density matrix has to be transformed into a density state vector with basis operators. For example the equilibrium density matrix for a two spin system

$$\hat{\rho}_{eq} = \frac{1}{2}\left(\hat{E} + \frac{\hbar\gamma B_0}{k_b T}\hat{I}_z\right) = \begin{pmatrix} \frac{1}{2} + \frac{\hbar\gamma B_0}{k_b T} & 0 \\ 0 & \frac{1}{2} - \frac{\hbar\gamma B_0}{k_b T} \end{pmatrix}$$

turns into

$$|\hat{\rho}_{eq}\rangle = \begin{pmatrix} \frac{1}{2} + \frac{\hbar\gamma B_0}{k_b T} \\ 0 \\ 0 \\ \frac{1}{2} - \frac{\hbar\gamma B_0}{k_b T} \end{pmatrix}, \text{ with the basis operators: } \begin{pmatrix} |\alpha\rangle\langle\alpha| \\ |\alpha\rangle\langle\beta| \\ |\beta\rangle\langle\alpha| \\ |\beta\rangle\langle\beta| \end{pmatrix}.$$

Generally the density state vector can be expressed by the basis operators: $|\hat{\rho}(t)\rangle = \sum_{k=1}^{N^2} b_k(t)\hat{\hat{B}}_k$, where $\{\hat{\hat{B}}_k\}$ is a complete set of basis superoperators. The Hamiltonian superoperator, also commonly called Liouvillian with symbol $\hat{\hat{\mathscr{L}}}$, must then be expressed in the same basis.

Equation of motion in the Liouville space

When making a transformation into the Liouville space the commutator in the Liouville equation of motion, (1.4.3), is absorbed into the Liouvillian operator:

$$\frac{d}{dt}|\hat{\rho}(t)\rangle = -i\hat{\hat{\mathscr{L}}}|\hat{\rho}(t)\rangle. \tag{1.9.1}$$

Equation (1.9.1) is now analogue to the Schrödinger equation in the way that $\hat{\hat{\mathscr{L}}}$ is an operator acting on a vector. The solution for a time independent $\hat{\hat{\mathscr{L}}}$ is now given by a left hand side multiplication with a propagator:

$$|\hat{\rho}(t)\rangle = e^{-i\hat{\hat{\mathscr{L}}}t}|\hat{\rho}(0)\rangle.$$

Interaction representation of Liouvillians

The Liouvillian can be transformed just as the Hamiltonian into an interaction representation in order to remove large terms or time dependency. Analogously

to equation (1.7.1) the effect of a large term $\hat{\hat{\mathscr{L}}}_0$ can be removed by

$$\hat{\hat{\mathscr{L}}}^T(t) = e^{i\hat{\hat{\mathscr{L}}}_0 t}\hat{\hat{\mathscr{L}}}_1(t)e^{-i\hat{\hat{\mathscr{L}}}_0 t}$$

and the density state vector is transformed as

$$|\hat{\rho}^T\rangle = e^{i\hat{\hat{\mathscr{L}}}_0 t}|\hat{\rho}\rangle.$$

So the Liouville space equation of motion in the interaction frame is:

$$\frac{d}{dt}|\hat{\rho}^T(t)\rangle = -i\hat{\hat{\mathscr{L}}}^T|\hat{\rho}^T(0)\rangle.$$

1.9.2 Redfield relaxation theory

To start with, the Redfield relaxation theory will be presented in the Hilbert space, then a transformation to the Liouville space will be made. The notation used here was taken from [2]. The effect of the surrounding lattice is represented by the fluctuation Hamiltonian

$$\hat{\mathscr{H}}_1 = \sum_q F^{(q)}(t)\hat{A}^{(q)},$$

where $F^{(q)}(t)$ is the function describing the fluctuations of the corresponding operator $\hat{A}^{(q)}$. The index q indicates the coherence order. $\hat{\mathscr{H}}_1$ is hermitian and assumed to have zero time average. The total Hamiltonian is then given by the sum of the spin interaction and Zeeman terms contained in $\hat{\mathscr{H}}_0$ and the comparatively small random fluctuations $\hat{\mathscr{H}}_1$. A transition into the interaction frame of $\hat{\mathscr{H}}_0$ removes the large interaction terms:

$$\hat{\mathscr{H}}_1^T(t) = e^{i\hat{\mathscr{H}}_0 t}\hat{\mathscr{H}}_1(t)e^{-i\hat{\mathscr{H}}_0 t} = \sum_{p,q} e^{-i\omega_p^{(q)}t}\hat{A}_p^{(q)} \tag{1.9.2}$$

The last step is taken according to equation (1.7.3). If there are different operators with the same coherence order q involved, the additional index p is used to distinguish the characteristic frequencies. As an example the basis operators

$\hat{I}_z\hat{S}_z$, $\hat{I}_+\hat{S}_-$ and $\hat{I}_-\hat{S}_+$ all have the same coherence order $q = 0$ but their frequencies are, according to (1.7.3), 0, $-\omega_I + \omega_S$ and $\omega_I - \omega_S$ respectively. The index p is used to account for this. The equation of motion in the interaction frame is:

$$\frac{d}{dt}\hat{\sigma}^T(t) = -\left[\hat{\mathscr{H}}_1^T(t), \hat{\sigma}^T(t)\right]. \qquad (1.9.3)$$

The density operator is described by σ instead of ρ in order to emphasise the fact that this is not the full but a reduced density operator, as the effect of the lattice terms have been moved into $\hat{\mathscr{H}}_1(t)$ rather than being included explicitly. Equation (1.9.3) can be integrated and the solution re-substituted in order to yield a second order time dependent perturbation approximation:

$$\frac{d}{dt}\hat{\sigma}^T(t) = -\int_0^\infty \overline{\left[\hat{\mathscr{H}}_1^T(t), \left[\hat{\mathscr{H}}_1^T(t-\tau), \sigma^T(t)\right]\right]}d\tau. \qquad (1.9.4)$$

The time average of the fluctuation terms $F^{(q)}(t)$ in equation (1.9.4) are described by the correlation functions $g^{(q,q')}(\tau) = \overline{F^{(q)}(t)F^{(q'*)}(t+\tau)}$. With (1.9.2) the equation of motion becomes:

$$\frac{d}{dt}\hat{\sigma}^T(t) = -\frac{1}{2}\sum_{q,q',p,p'}\left[\hat{A}_p^{(q)}, \left[\hat{A}_{p'}^{(q')}, \hat{\sigma}^T(t)\right]\right]J_{q,-q'}\left(\omega_{p'}^{(q')}\right)\exp(i(\omega_p^{(q)} + \omega_{p'}^{(q')})t),$$
$$(1.9.5)$$

where $J_{q,-q'}(\omega_{p'}^{(q)})$ is the spectral density at the frequency $\omega_{p'}^{(q')}$ which is defined by

$$J_{q,-q'}(\omega) = \int_{-\infty}^{\infty}g^{(q,q')}(\tau)e^{-i\omega\tau}d\tau. \qquad (1.9.6)$$

Equation (1.9.5) can be simplified by two assumptions:

- There is no correlation between terms of different coherence order q. This excludes cross correlation, which has the effect that all terms of different index q are zero and the fluctuating terms that are left are $\overline{F^{(q)}(t)F^{(q*)}(t+\tau)} = \overline{F^{(q)}(t)F^{(-q)}(t+\tau)}$.

- The terms that cause the oscillation $\exp(i(\omega_p^{(q)} + \omega_{p'}^{(q')})t)$ are simplified to $\exp(i(\omega_p^{(q)} - \omega_{p'}^{(q)})t)$ by the first assumption. If the difference $(\omega_p^{(q)} -$

$\omega_{p'}^{(q)})$ is large, the exponential term is oscillating rapidly which means that its contribution is insignificant. Only the terms for which $p = p'$, which are the secular terms, will survive as the phase oscillation is zero.

Looking at equation (1.9.5) one can see the advantage of making the transformation to the Liouville space: the double commutator turns into a simple operator multiplication:

$$\frac{d}{dt}|\hat{\sigma}^T(t)\rangle = -\frac{1}{2}\sum_{q,p}\hat{\hat{A}}_p^{(q)}\hat{\hat{A}}_p^{(-q)}J_q\left(\omega_p^{(q)}\right)|\hat{\sigma}^T(t)\rangle = \hat{\hat{\Gamma}}|\hat{\sigma}^T(t)\rangle, \qquad (1.9.7)$$

where the two assumptions have already been incorporated. $\hat{\hat{\Gamma}}$ is the relaxation superoperator. As the terms in $\hat{\hat{\Gamma}}$ are secular a transformation back into the laboratory frame does not change it and gives the equation of motion with relaxation in the Liouville space:

$$\frac{d}{dt}|\hat{\sigma}(t)\rangle = -i\hat{\hat{\mathscr{L}}}_0|\hat{\sigma}(t)\rangle - \hat{\hat{\Gamma}}\left(|\hat{\sigma}(t)\rangle - |\hat{\sigma}_{eq}(t)\rangle\right). \qquad (1.9.8)$$

The difference term $|\hat{\sigma}(t)\rangle - |\hat{\sigma}_{eq}(t)\rangle$ ensures that the system relaxes back to thermal equilibrium. A method developed by M.Levitt et al. enables to convert equation (1.9.8) to a homogeneous equation of motion by modifying the relaxation operator $\hat{\hat{\Gamma}}$ [9]. This makes it possible to solve the differential equation with the use of a simple matrix exponential.

CHAPTER 2

DNP - principles and strategies

As could be seen in section 1.4.4, NMR suffers from an inherently low sensitivity due to the small Boltzmann factor. It was also shown that the spin polarisation, which is directly proportional to the SNR, scales with $\tanh(\frac{\hbar \gamma B_0}{2k_b T})$. From this, two obvious strategies to boost the SNR are to increase the external magnetic field strength or decrease the temperature. It is possible to cool down samples to the Millikelvin regime but the resulting extremely long relaxation times are a major experimental drawback [10]. There is also a limit to increasing the magnetic field, a commercial 1GHz spectrometer has recently been developed [11] but material costs increase substantially.

In 1953, only seven years after the first acquisition of NMR spectra in the liquid and solid state by Bloch [12] and Purcell [13], Albert Overhauser proposed the possibility of transfering polarisation from one spin species with high gyromagnetic ratio to another with low γ [14]. This was experimentally verified by C. Slichter and T. Carver as a transfer of electron polarisation to metallic Lithium nuclei within the same year [15], see figure 2.1. The effect was termed Dynamic Nuclear Polarisation (DNP).

For the experiment temperatures of a few Kelvin[1] are used in order to achieve high electron polarisation which can then be transferred to the nuclei via the

---

[1]which increases the nuclear T_1 to more practical values compared to the Millikelvin range
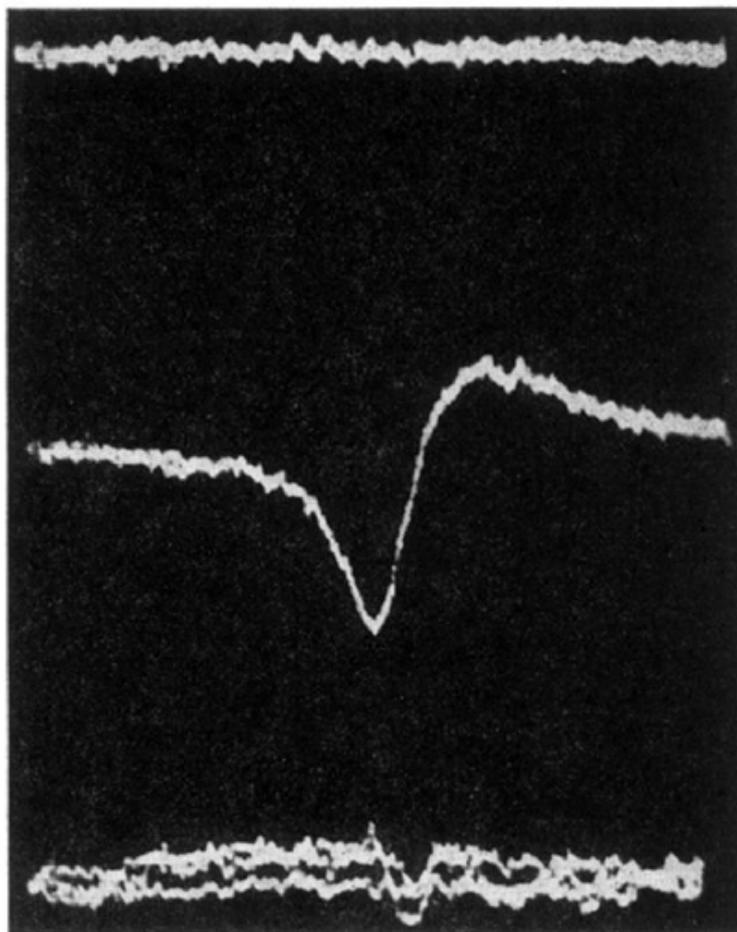
Figure 2.1: First published DNP signal enhancement [15]. Original figure caption: "Oscilloscope picture of 50 kc/sec nuclear resonance absorption vs static magnetic field. Field excursion 0.2 gauss. Top line: ^{7}Li resonance (lost in noise). Middle line: ^{7}Li resonance enhanced by electron saturation. Bottom line: Proton resonance in glycerine sample." The bottom line was recorded with an identical receiver gain as the two others for reference. The ratio of proton to lithium nuclei present in the sample was 8, which in combination with the fact that the gyromagnetic ratio of protons is approximately 2.6 times larger than that of Lithium nuclei, demonstrates the strong enhancement of the Lithium signal (estimated to be $\varepsilon \approx 100$).

hyperfine interaction using appropriate microwave irradiation. The necessary polarising agents - the free electron spins - were provided by the conducting band. This strategy has since been extended to provide polarisation also directly in the liquid state as well as in insulators, where the sample is doped with paramagnetic impurities in order to provide the polarisation source. The precise polarisation transfer pathways differ in each case, and the major ones will be introduced in this chapter. A few polarisation strategies combining the introduced pathways with temperature or magnetic field jumps will be covered briefly. A comprehensive review of the different DNP processes can be found, for example, in [10] and [6].

Other polarisation techniques exist, for example parahydrogen induced polarisation (PHIP), where a polarised parahydrogen pair is transferred onto a target molecule by a chemical reaction [16]. Although very high polarisation can be generated, this procedure is limited to a small range of model systems. It is also possible to use optical pumping in order to enhance the polarisation of Xe or He gas [17] which is done by transferring the angular momentum of polarised laser light onto the nuclear spins. The main application for this technique has become lung imaging in magnetic resonance imaging and the study of surfaces.

DNP stands out as it is widely applicable to a large range of molecules in the liquid and solid state at room temperature and under cryo-conditions. All that is required is the presence of a paramagnetic impurity in the sample, with a concentration on the order of mM.

2.1 Overhauser Effect

The transfer of polarisation from electrons to nuclei is possible through the hyperfine interaction (1.5.4), which enables cross relaxation. For this a time dependent modulation of the hyperfine interaction on the times scale of the electron

Larmor frequency is needed. Hence the Overhauser effect is only observed in liquids, where the modulations originate from molecular tumbling, or metals, where high electron mobility is given. The energy level diagram of a model system containing one nucleus coupled to an electron is given in figure 2.2. The lowest energy level is $|\beta\alpha\rangle$ as the electron gyromagnetic ratio has an opposite sign. Microwave irradiation equalises the populations of energy levels $|\alpha\beta\rangle$ and
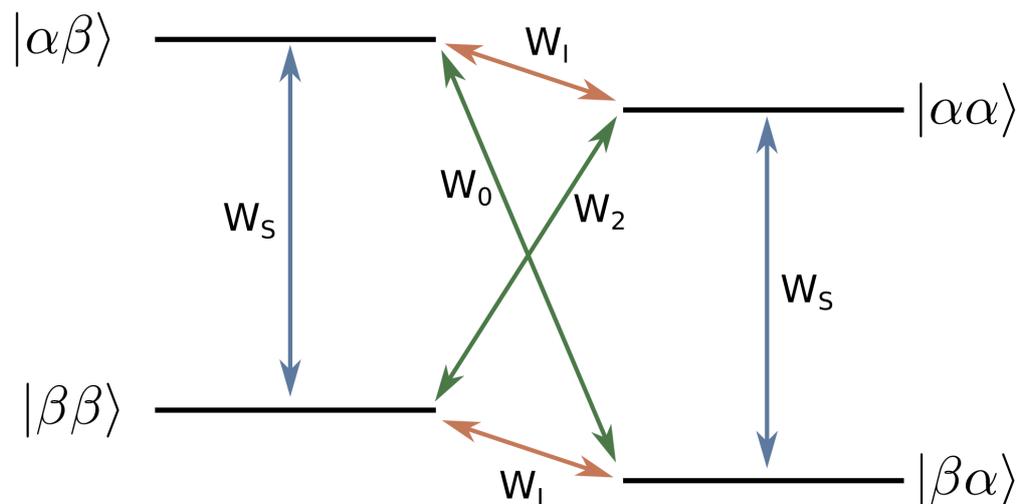
Figure 2.2: Energy level diagram of a coupled electron nucleus pair. The factors W_i indicate the transition rates between the energy levels, W_I and W_S are the nuclear and electron transition rate respectively whereas W_0 and W_2 are the single and double quantum rates. The states are shown in the form form $|m_S m_I\rangle$.

$|\beta\beta\rangle$ as well as $|\alpha\alpha\rangle$ and $|\beta\alpha\rangle$. When the microwaves are switched off, relaxation takes place with the rates indicated in the figure, so the nuclear populations return to their initial state with the rate W_I and the electron populations with W_S. Additionally cross relaxation with the rates W_0 and W_2 occurs which is the driver of the polarisation build up on the nuclei. Using the Solomon equation [18] one can set up a system of coupled rate equations which lead to the enhancement factor [19]

$$\varepsilon = \frac{\langle \hat{I}_z \rangle}{\hat{I}_{z0}} = 1 - \zeta s f \frac{|\gamma_S|}{\gamma_I},$$

where $\langle \hat{I}_z \rangle$ is the average of the dynamic nuclear polarisation, $\hat{I}_{z0}$ is the equilibrium polarisation. The factor ζ

$$\zeta = \frac{W_2 - W_0}{W_0 + W_2 + 2W_1} \quad \in [-1, 0.5]$$

is the coupling factor which becomes equal to -1 for a purely scalar reaction and 0.5 for a purely dipolar reaction, and takes a value in between for a mixture of both. The factor s indicates how well the electron resonance is saturated:

$$s = \frac{\langle S_0 \rangle - \langle S_z \rangle}{\langle S_0 \rangle} \quad \in [0, 1]$$

and becomes equal to 1 for a full saturation. f indicates the amount of leakage from the nuclear polarisation that is not caused by the electron:

$$f = \frac{W_0 + W_2 + 2W_1}{W_0 + W_2 + 2W_1 + W^0} = 1 - \frac{T_{1n}^{+S}}{T_{1n}^{-S}}, \tag{2.1.1}$$

where $T_{1n}^{-S} = \frac{1}{W^0}$ is the nuclear relaxation time in the absence of the electron spin, and T_{1n}^{+S} analogously the nuclear relaxation time in the presence of the spin. Ideally the nuclear relaxation is much faster when electrons are present and the leakage factor becomes 1. The Overhauser effect is also commonly used for polarisation transfer from high γ nuclei, mostly protons, to low γ nuclei such as ^{13}C and ^{15}N. The enhancement scales with $\frac{1}{r^3}$ which makes molecular distance measurements possible. This technique is routinely used in protein structure determination.

2.2 Solid Effect

As opposed to the Overhauser effect, the solid effect does not depend on modulations of the hyperfine interaction by motion. Instead, the pseudosecular part of the hyperfine Hamiltonian is used to drive the polarisation transfer from the electrons to the nuclei. In the solid state the terms $B_k \hat{I}_{kx} \hat{S}_z$ are not averaged out and the nuclear quantisation axis is no longer along the Zeeman axis. This is
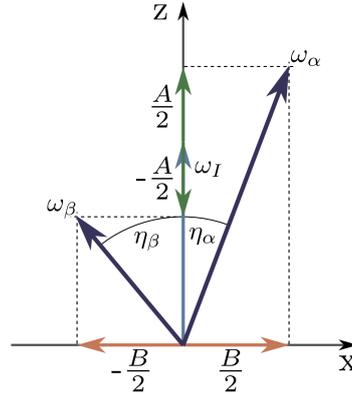
Figure 2.3: The nuclear spin has a different quantisation axis depending on the electronic state.

illustrated in figure 2.3 for an electron coupled to a single nucleus. The $A\hat{I}_z\hat{S}_z$ term gives an energy level splitting for the nucleus along the Zeeman axis but the $B\hat{I}_x\hat{S}_z$ induces a different quantisation axis for the nuclear 'up' or 'down' state, depending on which state the electron is in. The factors from figure 2.3 are

$$\eta_\alpha = \arctan \frac{-B}{A+2\omega_I}$$
$$\eta_\beta = \arctan \frac{-B}{A-2\omega_I}.$$

Hence the energy levels are not given by the pure product states anymore but contain admixtures of other states of the same electronic but different nuclear configuration (see figure 2.4). The new states are then given by:

$$|1\rangle = \cos\frac{\eta_\beta}{2}|\beta\alpha\rangle + \sin\frac{\eta_\beta}{2}|\beta\beta\rangle$$
$$|2\rangle = \cos\frac{\eta_\beta}{2}|\beta\beta\rangle - \sin\frac{\eta_\beta}{2}|\beta\alpha\rangle$$
$$|3\rangle = \cos\frac{\eta_\alpha}{2}|\alpha\alpha\rangle + \sin\frac{\eta_\alpha}{2}|\alpha\beta\rangle$$
$$|4\rangle = \cos\frac{\eta_\alpha}{2}|\alpha\beta\rangle - \sin\frac{\eta_\alpha}{2}|\alpha\alpha\rangle.$$

The transitions between the levels $|1\rangle$ and $|4\rangle$, as well as $|2\rangle$ and $|3\rangle$, that were forbidden by the selection rule $\Delta m = \pm 1$ are now slightly probable, with $W_2, W_0 \propto \sin^2\left(\frac{\eta_\alpha-\eta_\beta}{2}\right) \propto \omega_I^{-2}$. So the solid effect efficiency decreases with

$$|4\rangle = \cos\tfrac{\eta_\alpha}{2}|\alpha\beta\rangle - \sin\tfrac{\eta_\alpha}{2}|\alpha\alpha\rangle$$

$$|3\rangle = \cos\tfrac{\eta_\alpha}{2}|\alpha\alpha\rangle + \sin\tfrac{\eta_\alpha}{2}|\alpha\beta\rangle$$

$$|2\rangle \cos\tfrac{\eta_\beta}{2}|\beta\beta\rangle - \sin\tfrac{\eta_\beta}{2}|\beta\alpha\rangle$$

$$|1\rangle = \cos\tfrac{\eta_\beta}{2}|\beta\alpha\rangle + \sin\tfrac{\eta_\beta}{2}|\beta\beta\rangle$$
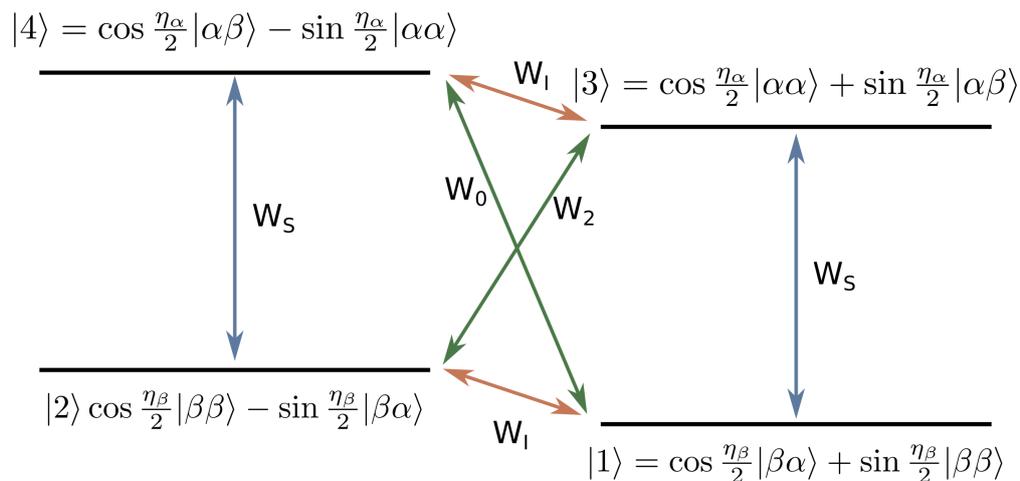
Figure 2.4: Energy level diagram of a coupled electron nucleus pair for the solid effect. As before, the factors W_i indicate the transition rates between the energy levels, W_I and W_S are the nuclear and electron transition rate respectively whereas W_0 and W_2 are the single and double quantum rates.

larger external magnetic fields. Microwave irradiation on the frequencies $\omega_S \pm \omega_I$, which correspond to the transitions W_2 and W_0, causes the nuclear and electron spin to flip simultaneously, either as double or a zero quantum spin flips. In the ideal case the continuous microwave irradiation equalises the populations of the levels $|1\rangle$ and $|4\rangle$, or $|2\rangle$ and $|3\rangle$ depending on whether the frequency $\omega_S + \omega_I$ or $\omega_S - \omega_I$ is used. This already leads to a relative increase of the nuclear population difference. The system then drives the nuclear polarisation up further as it tries to maintain a Boltzmann distribution for the electrons, so between levels $(|1\rangle+|2\rangle)$ and $(|3\rangle+|4\rangle)$, by using T_{1e} relaxation. This is shown schematically in figure 2.5, where the double quantum transition was irradiated. In order to avoid cancellation of polarisation due to a simultaneous double and zero quantum transition the line width of the electron transition δ has to be smaller than the nuclear Larmor frequency ω_I. This is the case for example for the polarising agent Trityl, which is very symmetric and, as a result, has a small g tensor anisotropy and hence narrow line width (see section 2.5). A typical sweep curve,
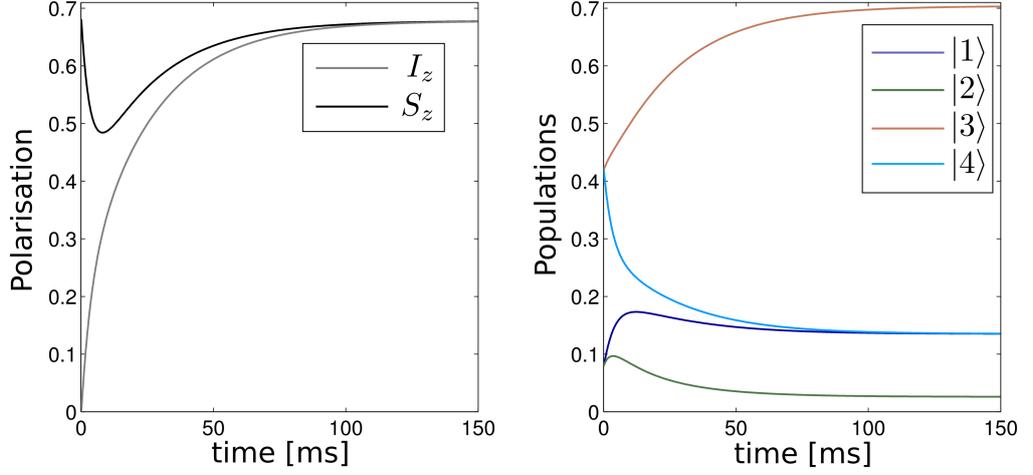
Figure 2.5: Left: Polarisation build up curves. Right: Fractional populations of the four different states. States $|3\rangle$ and $1\rangle$ are driven up and down in order to maintain the electron Boltzmann factor between $|1\rangle$ and $|4\rangle$ respectively. Parameters: ω_1=80 kHz, the distance between electron and proton is 8Åand azimuthal angle $\theta = \frac{\pi}{4}$, resulting in the hyperfine coupling constants A=94 kHz and |B|=0.2 MHz. Relaxation parameters: $r_{1n} = 10^2 \frac{\text{rad}}{\text{s}}$, $r_{2n} = 10^4 \frac{\text{rad}}{\text{s}}$, $r_{1e} = 0.5 \frac{\text{rad}}{\text{s}}$, $r_{2e} = 10^4 \frac{\text{rad}}{\text{s}}$.

where the enhancement is plotted against the irradiation frequency is shown in figure 2.6. For a single nucleus coupled to an electron Abragam and Goldman derive the following rate equations [10]:

$$\frac{\mathrm{d}P_e}{\mathrm{d}t} = -\frac{1}{T_{1e}}\left(P_e - P_0\right) \qquad \frac{\mathrm{d}P_n}{\mathrm{d}t} = -\frac{1}{T_{1n}}P_n,$$

with P_0 being the equilibrium Polarisation of the electron. The effects of microwave off resonance saturation of the electron single quantum transition has been neglected for these equations but can be incorporated as well. The longitudinal relaxation rates are derived from the transition probabilities of the spin system. These are scaled by a thermal factor $r = \exp(\frac{-\hbar(\omega_S \pm \omega_I)}{k_b T})$ to ensure that a transition towards a lower energy state has a higher probability than vice versa. Then for example W_0 is the probability for a transition from the higher energy state to the lower, and rW_0 indicates the likelihood of a transition the other way.
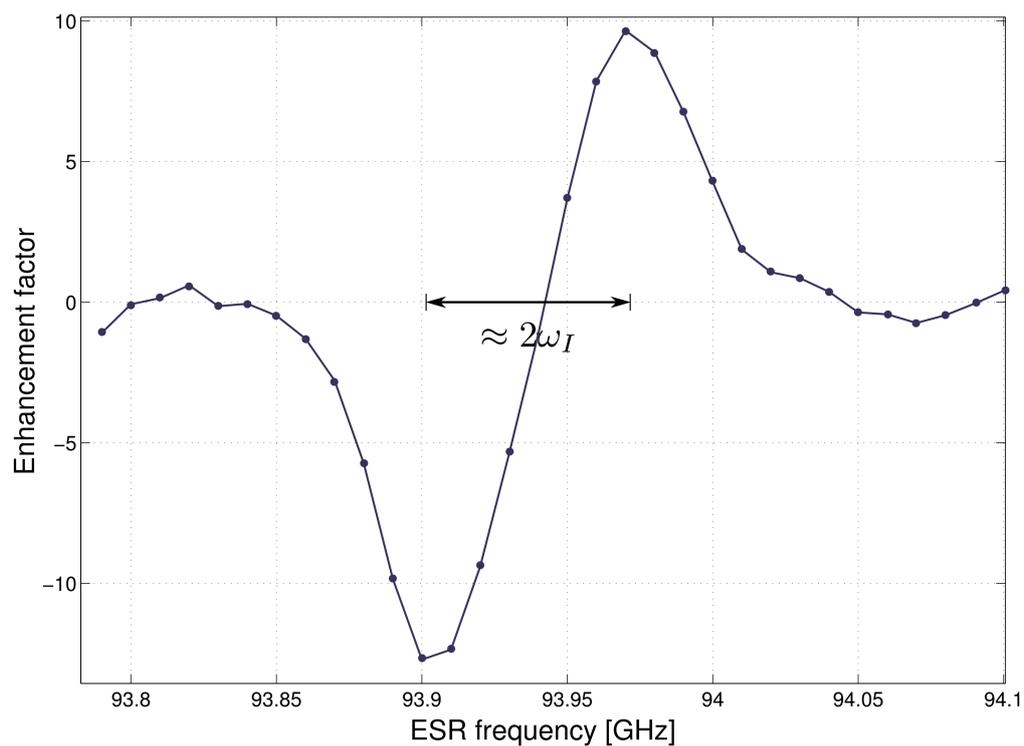
Figure 2.6: Frequency dependency of the DNP enhancement. Sample: 1mM ^{13}C-labelled Acetate with 15mM Ox63 Trityl in 1:1 water glycerol mixture. The polarisation time was one minute. The fact that the maxima are 70 MHz apart, which corresponds to approximately $2\omega_I$, indicates that the main enhancement mechanism is the solid effect.

The relaxation times are given as

$$\frac{1}{T_{1e}} \approx (1+r)W_S \qquad \frac{1}{T_{1n}} \approx (1+r)W_0(1 - P_e P_0).$$

It is assumed that the nuclear dipole interaction distributes the polarisation evenly throughout the sample.

The dynamics of the solid effect will be discussed in more detail in chapter 3.

2.3 Cross Effect

The cross effect (CE) is a three spin mechanism of two coupled electrons and one nucleus. The condition for polarisation transfer is that the resonance frequencies of the two electrons are separated by the nuclear Larmor frequency, so [20]:

$$|\omega_{S1} - \omega_{S2}| = \omega_I. \qquad (2.3.1)$$

This condition is fulfilled when the EPR line of the polarising agent is broader than ω_I. This broadening has to be inhomogeneous, so it has to originate from an overlay of separate electron resonances, whose line width is smaller than ω_I in order to avoid cancellation effects. Alternatively the condition can be met with specially designed bi-radicals, which have electron resonances separated by ω_I. This has been done by connecting two nitroxide radicals, where the bond length controls the coupling strength [21, 22]. In figure 2.7 the energy levels of a three spin system obeying the condition (2.3.1) are shown, so the levels $|4\rangle$ and $|5\rangle$ are degenerate. Unlike the solid effect, the cross effect is based on allowed transitions, as it is based on three spin flips with $\Delta m = \pm 1$ [23]. Figure 2.7 shows a schematic for the case of positive and negative enhancement. The polarisation build up is, just as in the case of the solid effect, a combination of the equilibration of populations of energy levels spaced by the irradiation frequency ω_{CE} as shown in figure 2.7, as well as the electron populations trying to obey the Boltzmann statistics. As the EPR lines spread out with higher field

strength, condition (2.3.1) becomes harder to satisfy, so the enhancement scales with ω_I^{-1}[23]. This is more favourable for higher field strengths as the ω_I^{-2} scaling of the solid effect.

2.4   Thermal mixing

The thermal mixing effect is an extension of the cross effect with the inclusion of more electrons and nuclei. It is currently described in thermodynamical terms as a large number of spins is involved. The spin system is divided into three interacting parts, the electron Zeeman bath (EZB), the nuclear Zeeman bath (NZB) and the electron dipolar bath (EDB) each with their own inverse spin temperature.The EPR line width δ is comparable to or larger than the nuclear Larmor Frequency. Under microwave irradiation close to but slightly off the electron resonance frequency the electron spins become more ordered and hence the dipolar entropy decreases. As a result the spin temperature of the EDB is lowered. Energy conserving three spin (electron-electron-nuclear) exchange processes [24] with the electrons that have not been saturated by the microwaves then cool the NZB, which means the nuclear polarisation is increased.

When the high temperature approximation can be made, thermal mixing can be described quantitatively with Provotorov theory [25]. This is not possible any more for lower temperatures.
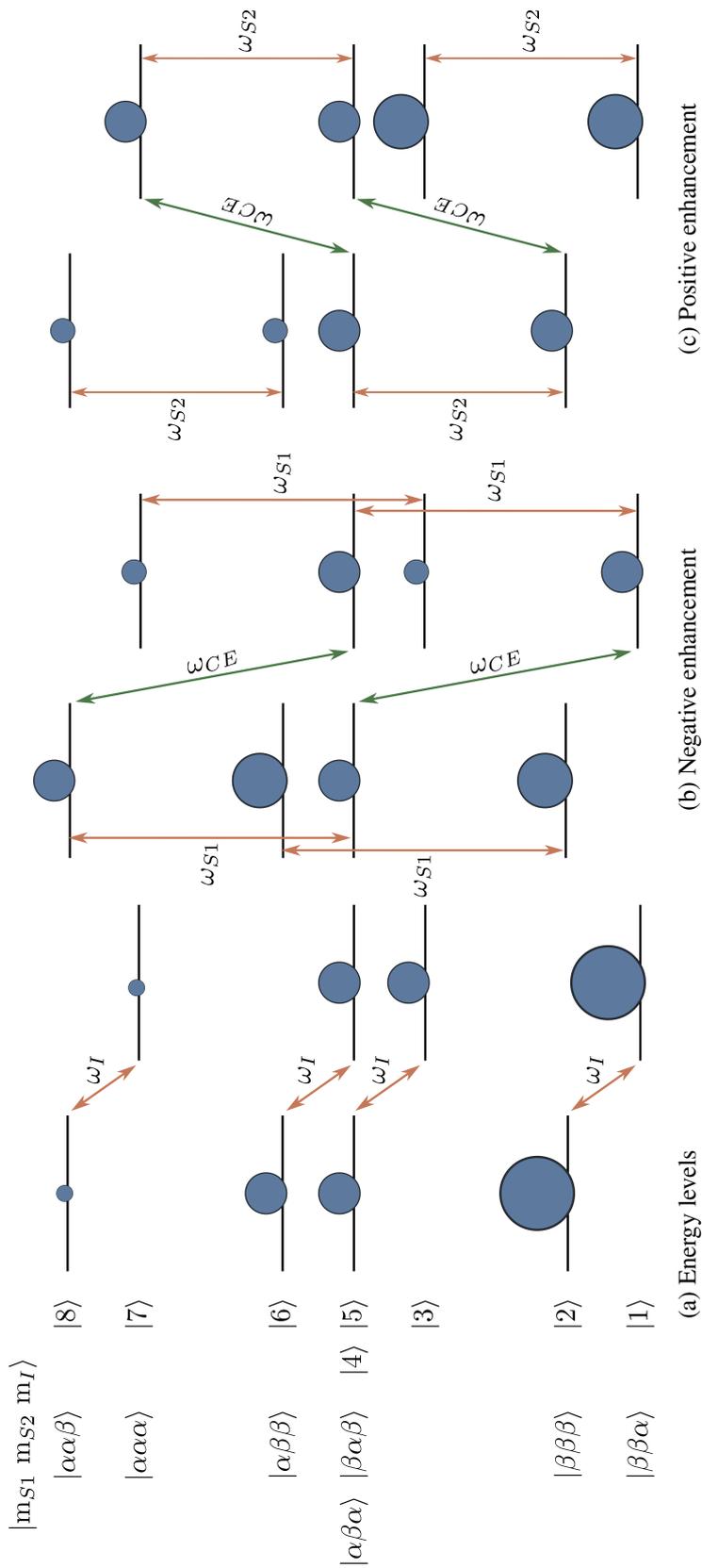
Figure 2.7: Cross effect. Figure from [23]. The size of the circle represents the relative population of the energy level. It is clear to see that in 2.7b all nuclear higher energy levels are more populated than the lower levels, resulting in a negative enhancement, whereas for the positive enhancement the opposite holds.

2.5   Polarising agents

Two frequently used carriers of paramagnetic impurities in DNP experiments are the radicals Ox63 Trityl[2] and 4-amino TEMPO[3]. The 4-amino TEMPO radical has a large ESR linewidth of approximately 411 MHz at 3.35 T compared to the nuclear Larmor frequency of 144 MHz, making the cross effect and thermal mixing the dominant mechanisms [24]. In contrast to this, the line width of the Ox63-Trityl is very narrow, with a full width at half maximum of approximately 30 MHz at 3.35 T. This results in the solid effect being the main polarisation transfer pathway. The narrow line width is caused by the near-isotropic g-tensor ($g_{xx} = 2.0034$, $g_{yy} = 2.0031$, $g_{zz} = 2.0027$), which originates from its high symmetry. The structure of the molecule shields the electron from the surrounding nuclei, keeping line broadening due to hyperfine interaction with the surrounding magnetically active nuclei small (see figure 2.8). The closest distance of approach for nuclei outside the radical is approximately 12Å, calculated from in house density functional theorem (DFT) simulations using ORCA [26]. The narrow line ensures a better EPR saturation compared to TEMPO and avoids partial cancellation of the positive and negative enhancement maximum.

2.6   Polarisation strategies

In practice various polarisation strategies exist, owing to the wide applicability of DNP. In the next section a brief overview over four approaches to DNP enhanced NMR are given. This is by no means a complete review of all available techniques but it is instructive to consider the advantages and disadvantages of these different strategies.

---

[2]tris (8-carboxyl-2, 2,6,6-tetra(hydroxyethyl) - benzo[1,2-d:4, 5-d]bis(1,3)-dithiole-4-yl) methyl sodium salt

[3](2,2,6,6-Tetramethylpiperidin-1-yl)oxyl
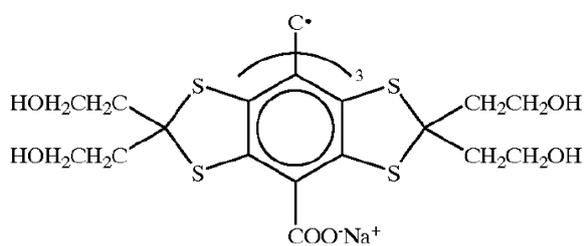
(a) Structure of Trityl Ox63, taken from [27].
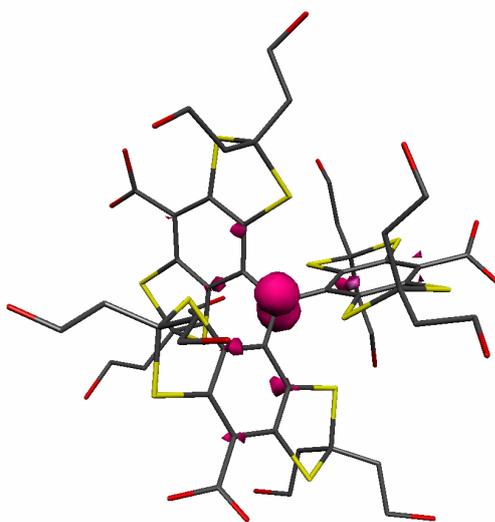
(b) 3D model for Trityl with the probability density function $|\psi|^2$ of the electron being depicted in pink. Image obtained from ORCA DFT simulation by W. Köckenberger.
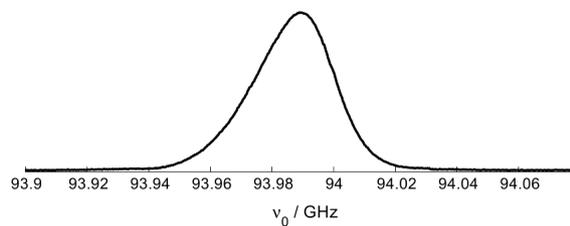
(c) ESR absorption spectrum, taken from [28]

Figure 2.8: Structure and ESR spectrum for the Trityl radical Ox 63.

2.6.1   High field liquid state DNP

The polarisation is generated with Overhauser DNP at high magnetic field (9.4 T) in the liquid state with the use of a high power (20W) gyrotron at 260 GHz. Main investigator into this approach is the T. Prisner group [29]. The high field results in high spectral resolution. The aim is to obtain spectra from biomolecules and large proteins in aqueous solution. The main advantages are the possibility of repeating the experiments enabling averaging and 2D NMR. One of the main difficulties encountered is sample heating. This is due to the fact that high microwave powers are needed for efficient enhancement in order to saturate the fast relaxing electrons in the liquid state but the high insertion loss in water causes sample heating. In order to alleviate this effect the sample volume is kept small. A double resonant probe for simultaneous DNP and NMR is used, which consists of a slotted cylindrical microwave cavity, where the slotted cylinder serves also as the RF coil [30]. The probe has been designed to minimise sample heating. Enhancements of -29 have been reported in Fremy's salt, which interestingly is larger than was expected from low field extrapolations of the Overhauser effect.

2.6.2   Field Jump Overhauser DNP

In this approach, used by the C. Griesinger group ([31, 32]), the higher efficiency of the Overhauser effect at lower fields is exploited. The polarisation takes place at 0.34 T, then the sample is shuttled to a 14 T observe magnet. An additional benefit is the lower microwave frequency of 9.5 GHz, which is technically more easy to achieve with standard ESR equipment. Heating is also not a serious issue at lower field. The polarisation takes only a few seconds due to short relaxation times. The transfer time of the sample is on the order of 110 milliseconds, which includes the shuttling time plus time for the sample to settle. It is possible to repeat the experiment, so averaging and 2D NMR are available. One drawback

is that due to the shuttling from low to high field the effective enhancement is scaled by $\frac{B_{pol}}{B_{obs}}$ due to the smaller Boltzmann factor at lower field. The highest enhancement reported so far is -3.7 although the system is still in development and higher values are expected in the future.

2.6.3 Solid State MAS DNP

In the solid state SE, CE and TM DNP effects are exploited. The group of R. Griffin has been working on optimisation of solid state MAS NMR with DNP for biological samples at cryogenic temperatures of down to 85 K [33, 34]. Specially designed biradicals have been developed in order to optimise the cross effect leading to enhancements of up to 300 [20, 21]. Due to the longer relaxation times at low temperatures the polarisation stage is more time consuming than in the liquid state. By polarising ^{1}H nuclei and transferring the polarisation to the lower γ nuclei, which typically have slower polarisation build up rates, time savings can be made with respect to directly polarising these nuclei. The sample remains in situ during the experiment, which enables to use averaging and 2D experiments. One potential disadvantage is, that the sample is frozen, so investigated proteins and ligands are not in their native environment. This problem can be overcome by incorporating melting of the sample by an infra-red laser after the polarisation step [35, 36]. This way samples are observed with liquid state resolution at room temperature. Additionally this method benefits from the larger Boltzmann factor at the lower temperature, hence increasing the effective enhancement by a factor of $\frac{T_{obs}}{T_{pol}}$.

2.6.4 Dissolution DNP

Dissolution DNP is based on polarising the sample at very low temperature (~ 1.4 K) and magnetic fields in the range of 3.4 T to 5 T . This yields large

45

polarisation factors on the order of hundreds using relatively inexpensive ESR equipment. Then the sample is rapidly dissolved and transferred to a high field observe magnet. Due to the temperature jump effective enhancements of more than 10,000 have been reported [37]. Chemical reaction dynamics ([38, 39]), and metabolomics [40] can been studied with this technique. It is also possible to inject the sample into animals for in vivo NMR and MRI applications, which is currently used for cancer and stroke research [41–43]. The group of S.J. Nelson at the UCSF is working on establishing this technique for in vivo cancer diagnostics in humans [44, 45].

In order to minimise the sample shuttling time as well as to avoid an unknown magnetic field profile along the shuttling path a novel two centre spectrometer has been built in Nottingham [46]. This has been shown to be able to resolve resonances with very short T_1 relaxation times due to the faster shuttling than the typical stand alone polariser set up [47]. One drawback is the single shot nature of the experiment, as the recycling of the sample after the dissolution is not viable. One way to overcome this issue and to be able to obtain 2D spectra is to use the ultra fast 2D sequences by L. Frydman [48–50]. Another way, presented in this thesis, is the use of a probe with multiple RF coils at different spatial positions of the sample tube, all tuned to the same resonance frequency. Using this strategy makes it possible to take advantage of the polarised sample that would otherwise lay outside the sensitive coil region. One can perform independent experiments: Either all signals from the same experiment can be used for averaging, or if the same experiment is repeated with a small delay which is incremented for each coil, this could be used to resolve fast dynamical processes in the sample for example protein-ligand binding or protein folding. The multi-coil probe will be discussed in more detail in chapter 4. Another drawback might be that not all molecules survive the freezing and dissolution step, but many small ligands and biochemically relevant molecules have thus far shown to be robust enough for this type of experiment [51, 52]. Larger proteins,

that are more sensitive to the treatment during polarisation and dissolution, can be placed in the sample tube in the observe magnet and binding can be observed by NOE effects when the polarised ligand has been injected.

2.6.5 Summary

All the strategies introduced above are still undergoing development and optimisation. The large range of applications in the fields of chemistry, material science and the biomedical sciences make all these DNP techniques well worth exploring. Currently the theoretical understanding of the solid state DNP effects is limited to qualitative statements, no quantitative predictions of the polarisation build up can be made as of date[4]. This is due to the difficulty of having a large number of spins involved, which makes the density operator and Hamiltonians describing the system too large to compute. In the next chapter approaches to tackling this issue will be presented.

---

[4]with the exception of the high temperature description of thermal mixing

Solid effect simulations in the Liouville space

Dynamic Nuclear Polarisation (DNP) has widely gained popularity in the recent years for its ability to greatly increase the NMR signal available in an experiment. In order to optimise the polarisation step of the experiment it would be beneficial to be able to simulate the evolution of the spin system during DNP. However, the full quantum mechanical treatment is challenging as the Liouvillian operator describing the interactions within the spin system scales with 4^N, where N is the number of spins in the system. This quickly yields unmanageable matrix sizes.

Abragam and Goldman dealt with this issue by applying a thermodynamical model [10]. The rate equations introduced in chapter 2 have been derived from the transition diagram of a two spin system, assuming the nuclear dipole interaction mediates the distribution of polarisation to all nuclei. This description is unable to incorporate properties of individual radicals. Recent progress in the development of EPR hardware allows DNP with pulsed microwave fields [53] and efforts are made to find appropriate optimised pulses for polarisation transfer [54]. However, also here the thermodynamical model is not suitable to make predictions and a quantum mechanical model has to be employed.

Shimon Vega and co-workers published a quantum mechanical approach in the Hilbert space, using rate equations for the populations. This reduces the system dimensionality to 2^N[55, 56].

It has been found that the propagator in the Liouville space is sparse for most NMR applications. Not all of its components need to be considered in order to obtain accurate simulation results. The concept of reducing the size of the state space has first been used by R.R. Ernst and R. Brushweiler for short term propagation [57]. Restricting the simulation to basis elements containing only low order spin correlations has been investigated by I Kuprov [58, 59]. Furthermore it has been used by L. Emsley and co-workers [60, 61] for the investigation into spin diffusion. Basis truncation to lower spin order correlations results in polynomial as opposed to exponential scaling of the state space.

In this chapter, three methods are presented to reduce the dimension of the matrices involved in the calculation of the system dynamics. The solid effect is used as a test case, for it has the most simple Hamiltonian out of the three solid state DNP mechanisms. The methods that will be presented have also been found to be applicable to the cross effect, and an extension to thermal mixing is very likely possible.

The first strategy uses an averaged Hamiltonian for the solid effect. The averaged Hamiltonian that will be presented in section 3.4.1 confines the trajectory of the density operator to the zero quantum subspace, hence all higher coherence order subspaces can be discarded. The error introduced by using the averaged Hamiltonian has been found to be less than 1% for a large range of parameters that were tested.

The second strategy presented here is restriction of the basis size by truncation up to a user specified spin correlation order. Whilst basis truncation as a strategy for state space size reduction has been previously presented [58, 60, 61], conditions for safe truncation, resulting in a certain error tolerance have now been

found [62].

The methods described above allow the simulation of the evolution of spin systems comprising of up to 25 ^{13}C nuclei and one electron in the Liouville space, where before the largest number reported was 10 spins in total. The reduction in size of the spin system decreases the computation time, for example in the case of six nuclei and one electron by up to a factor of 50.

At the end of the chapter a new and very promising approach based on subspace projections will be presented. This method, recently proposed by A. Karabanov, makes it possible to reduce the dimension of the propagator to the number of spins involved in the simulation. The conditions for the validity of the method as well as error analysis will be shown.

All simulations were carried out using the SPINACH package [59], which provides an easy to use library for the simulation of a large range of NMR experiments. The theoretical framework presented here was developed by Alexander Karabanov and Walter Köckenberger, all simulations were carried out by the author.

3.1   Solid Effect Hamiltonian and Liouvillian

The full Hamiltonian for the solid effect, involving one electron and many nuclei, includes the Zeeman term of the nuclei and the electron, the coupling between all particles, as well as the microwave irradiation.

$$\hat{\mathscr{H}} = \hat{\mathscr{H}}_Z + \hat{\mathscr{H}}_{IS} + \hat{\mathscr{H}}_{II} + \hat{\mathscr{H}}_{MW}, \qquad (3.1.1)$$

The expressions in 3.1.1 are given by:

$$\hat{\mathscr{H}}_Z = \omega_S \hat{S}_z + \sum_k \omega_I \hat{I}_{zk}$$

$$\hat{\mathscr{H}}_{IS} = \sum_k \left(A_k \hat{I}_z \hat{S}_z + B_k \hat{I}_x \hat{S}_z \right)$$

$$\hat{\mathscr{H}}_{II} = \sum_{j<k} d_{jk} \left[2\hat{I}_{jk}\hat{I}_{zk} - \frac{1}{2} \left(\hat{I}_{j-}\hat{I}_{k+} + \hat{I}_{j+}\hat{I}_{k-} \right) \right]$$

$$\hat{\mathscr{H}}_{MW} = \frac{\omega_1}{2} \left(e^{-i\omega_{\mu w} t} \hat{S}_- + e^{i\omega_{\mu w} t} \hat{S}_+ \right)$$

The concentration and hence the average separation of the electrons is assumed to be small enough to allow for omission of electron-electron coupling terms, which would otherwise result in CE or TM DNP. For a realistic 15 mM concentration of the Trityl radical the electron-electron distance is on average 48Å, which results in a maximum electron dipole interaction of 1.15 MHz. This is on the same order as some of the hyperfine interaction terms of nuclei close to the electron. Hence it can be assumed that at this concentration the DNP mechanism is not a pure solid effect. Nonetheless, in order to simplify the treatment at this stage the electron dipole interaction will be neglected. As an additional simplification the assumption of an isotropic g-tensor is made, hence the electron has only one resonance frequency. Only the secular and pseudosecular terms are included in the interaction Hamiltonians. The corresponding Liouvillian is calculated from $\hat{\hat{\mathscr{L}}} = [\hat{\mathscr{H}}, \hat{E}]$.

An electron rotating frame, with the electron having an offset of $\pm\omega_I$, is chosen as an interaction representation (see section 1.7). Then the Hamiltonian loses the explicit time dependency:

$$\hat{\mathscr{H}}^T = \omega_I \left(\hat{I}_z \pm \hat{S}_z \right) + \sum_k \left(A_k \hat{I}_z S_z + B_k \hat{I}_x \hat{S}_z \right)$$

$$+ \sum_{j<k} d_{jk} \left[2\hat{I}_{jk}\hat{I}_{zk} - \frac{1}{2} \left(\hat{I}_{j-}\hat{I}_{k+} + \hat{I}_{j+}\hat{I}_{k-} \right) \right] + \frac{\omega_1}{2} \left(\hat{S}_- + \hat{S}_- \right).$$

The sign of the electron Zeeman term in (3.1) determines whether a zero quantum or a double quantum DNP irradiation takes place. The difference will be the sign of the nuclear polarisation.

51

3.2 Relaxation operator for solid effect simulations

During the DNP experiment the sample temperature is low (around 1.4 K), hence the main source of nuclear relaxation is not the tumbling of nuclear dipoles as it is in the liquid state. The electrons are assumed to relax via electron-phonon coupling with the lattice and interaction with other electrons. For the solid effect to occur, the electron concentration has to be low enough for the electronic dipolar coupling to be negligible, hence this will be ignored as a relaxation pathway. The nuclear relaxation is dominated by electron fluctuations which are mediated through the hyperfine interaction. Following Abragam and Goldman [10], and neglecting secular terms with respect to the electron, the electronic relaxation can be described by the following superoperator:

$$\hat{\hat{\Gamma}}_S = R_1(\hat{\hat{S}}_+\hat{\hat{S}}_- + \hat{\hat{S}}_-\hat{\hat{S}}_+) + R_2\hat{\hat{S}}_z^2$$

which has the following effect on the longitudinal and transversal components of the electron spin:

$$\hat{\hat{\Gamma}}_S\hat{\hat{S}}_z = 4R_1\hat{\hat{S}}_z = r_{1e}\hat{\hat{S}}_z = \frac{1}{T_{1e}}\hat{\hat{S}}_z$$

$$\hat{\hat{\Gamma}}_S\hat{\hat{S}}_\pm = (R_2 + 2R_1)\hat{\hat{S}}_\pm = r_{2e}\hat{\hat{S}}_z = \frac{1}{T_{2e}}\hat{\hat{S}}_\pm.$$

r_{1e} and r_{2e} are the electronic longitudinal and transversal relaxation rates, which are taken from experimental data. As in a typical experiment $\omega_S^2 \gg r_{2e}^2$, the nuclear relaxation is assumed to be caused by the random fluctuations of the electron longitudinal component $\hat{S}_z$, which is transferred to the nuclei via the hyperfine interaction:

$$\hat{\mathscr{H}}'_{hfi} = W\hat{S}_z, \text{ with } W = A_k\hat{I}_{kz} + \frac{1}{2}\left(B_{k+}\hat{I}_+ + B_{k-}\hat{I}_-\right).$$

The prime over $\hat{\mathscr{H}}_{hfi}$ indicates the restriction of the hyperfine interaction to the longitudinal electronic components. These fluctuations have to be added to the total Hamiltonian as:

$$\gamma(t)W + \gamma(t)W^*,$$

where $\gamma(t)$ is a randomly fluctuating time function with a correlation time close to the longitudinal electronic relaxation time: $\tau_c = T_{1e}$. Keeping only secular terms with respect to the nuclear Zeeman interaction, the nuclear relaxation is then described by:

$$\hat{\hat{\Gamma}}_I = \sum_k r_1 \frac{1}{4} B_k^2 \left[\hat{\hat{I}}_{k-} \hat{\hat{I}}_{k+} + \hat{\hat{I}}_{k+} \hat{\hat{I}}_{k-} \right] + \sum_k r_2 A_k^2 \hat{\hat{I}}_{kz}^2,$$

with (3.2.1)

$$r_1 = \frac{\delta r_{1e}}{r_{1e}^2 + \omega_I^2} + \delta\tau', \qquad r_2 = \frac{\delta}{r_{1e}},$$

with $B_k^2 = |B_{k+}|^2 = |B_{k-}|^2$. The parameter δ is dimensionless and indicates the squared amplitude of the fluctuations of the $\hat{S}_z$ components, while τ' is a spin diffusion correction term with the dimension of time, containing the electronic spin concentration, spin diffusion coefficient and the internuclear distance [10, 63].The full relaxation operator is obtained by adding the nuclear and electron terms:

$$\hat{\hat{\Gamma}} = \hat{\hat{\Gamma}}_S + \hat{\hat{\Gamma}}_I.$$

So the average relaxation rates $r_{1n} = \dfrac{1}{T_{1n}}$ and $r_{2n} = \dfrac{1}{T_{2n}}$ are given by:

$$r_{1n} = r_1 \langle |B_k|^2 \rangle \qquad r_{2n} = r_2 \langle A_k^2 \rangle + \frac{r_{1n}}{2}. \tag{3.2.2}$$

The ratio of the nuclear relaxation rates is given by

$$\frac{r_{1n}}{r_{2n}} \sim \frac{r_1}{r_2} \sim \frac{r_{1e}}{\omega_I} + \tau' r_{1e},$$

so typically as $r_{1e} \ll \omega_I$, the nuclear longitudinal relaxation rate is smaller than the nuclear transversal relaxation rate. For example if one takes $r_{1e} = 10^3 \frac{\text{rad}}{s}$, $\omega_I \approx 10^8 \frac{\text{rad}}{s}$ and $\tau^{-1} \approx 10^6 \frac{\text{rad}}{s}$ then for $r_{2n} = 10 \frac{\text{rad}}{s}$ one gets $r_{1n} = 10^{-2} \frac{\text{rad}}{s}$. One can estimate δ by taking the above user defined values with (3.2.2)

$$\delta \approx \frac{r_{2n} r_{1e}}{\langle A_k^2 \rangle_k}.$$

Assuming $A_k \sim 10^6$ one gets $\delta \sim 10^{-8}$.

One can also introduce rates with which the double and zero quantum transitions relax, resulting in a smaller overall enhancement, but in order to keep the problem as simple as possible these have been ignored for the time being. Their effect on the steady state polarisation has been shown to be similar to that of the nuclear longitudinal relaxation rates by S. Vega and co-workers for cross relaxation rates smaller than the electron longitudinal relaxation rate [56].

For some simulations it can be instructive to exclude the scaling of the nuclear relaxation with the hyperfine interaction and assume the same relaxation rate for all nuclei. The nuclear relaxation operator is then

$$\hat{\hat{\Gamma}}_I = r_1(\hat{\hat{I}}_+\hat{\hat{I}}_- + \hat{\hat{I}}_-\hat{\hat{I}}_+) + r_2\hat{\hat{I}}_z^2, \tag{3.2.3}$$

using empirical relaxation constants for r_1 and r_2. Whenever this relaxation operator is used it will be referred to as the constant relaxation operator, as opposed to the relaxation operator derived from the electronic fluctuations being transferred to the nuclei via hyperfine interaction. This will be called the scaled relaxation operator. If the specific operator used in a simulation is not explicitly mentioned, the scaled relaxation operator was used by default.

The scaled relaxation operator results in unrealistically small nuclear relaxation terms for large distances from the electron as well as for certain orientations. For example is the nuclear longitudinal relaxation rate r_{1n} equal to zero for $\theta = 0$ and $\theta = \pi$. One can circumvent this by using a combination of a relaxation operator with constant and scaled terms. This has been done for example in [56].

3.3   SPINACH

All simulations have been carried out in the SPINACH package developed by I.Kuprov and co-workers [59]. This freely available MATLAB® function library enables to define spin geometry, the type of nuclei and interactions in-

volved as well as other parameters, then the trajectory of the spin system is calculated in the Liouville space by propagating the system repeatedly by Δt

$$|\hat{\rho}(k\Delta t)\rangle = \exp\left(-(i\hat{\mathscr{L}}+\hat{\Gamma})\Delta t\right)|\hat{\rho}([k-1]\Delta t)\rangle \quad k \in [1, n_{\text{steps}}]$$

until the final time $n_{\text{steps}}\Delta t$ defined by the user is reached. The inhomogeneity of $\hat{\Gamma}|\hat{\rho}_{eq}\rangle$ in the equation of motion has been removed by using a relaxation operator which has been modified in such a way that the system is relaxing to thermal equilibrium without the inhomogeneous term $|\hat{\rho}_{eq}\rangle$ ([9, 64]). The evolution of the spin system in SPINACH does not rely on diagonalisation of the Liouvillian, instead the propagator exponential is calculated using Taylor expansion [65]. The DNP Hamiltonian is now available in the library but in order to keep flexibility it was defined by the author.

Processing time   The time required for processing spin systems with a propagator of dimension N is plotted in figure 3.1. The limit a computer with 8 GB RAM can process lies at around N=16 K, which enables to simulate the dynamics of 7 spins using the full state space. Using a computer equipped with a 2.6 GHz processor, this calculation is rather time consuming and takes 14 hours. The processing time depends largely on the magnitude of the entries in the product of the Liouvillian and the time step $-i\hat{\mathscr{L}}\Delta t$. This stems from the aforementioned fact that SPINACH calculates the propagator $\exp(-i\hat{\mathscr{L}}\Delta t)$ by Taylor expansion. For the Taylor series to converge, the exponential term has to be smaller than one. In SPINACH the term $-i\hat{\mathscr{L}}\Delta t$ is hence scaled down by a factor s containing its largest Eigenvalue l: $s = \ln_2 l$, then the expansion is carried out. Conversion is ensured by checking that the largest term in the highest expansion order is smaller than a user defined tolerance, which is typically set to 10^{-14}.

After that, the obtained scaled propagator $\exp(-i\hat{\mathscr{L}}\Delta t/s)$ has to be squared s times to obtain the full propagator $\exp(-i\hat{\mathscr{L}}\Delta t)$. It is these matrix multiplica-

tions that are costly in time. The number of scaling steps hence depends also on Δt. The rest of the processing time depends on the number of time steps set by the user.
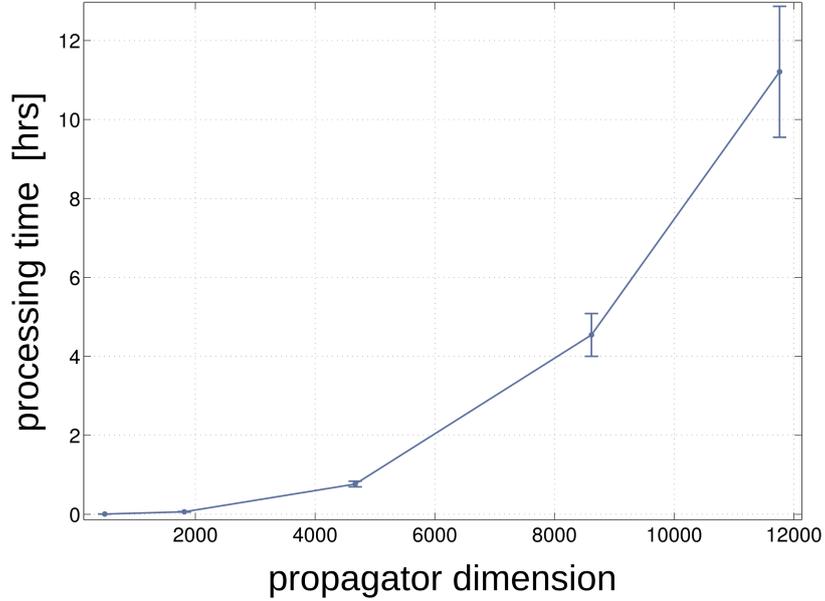
Figure 3.1: Propagator dimension versus processing time in hours. The variance is caused by the difference in performance of certain computers in the cluster and how many other jobs were carried out by the computer node at the same time as the simulation was running.

Basis of the Liouville space in SPINACH   The basis in which the Liouvillian and the density operator are expressed in SPINACH is the shift basis comprising of $\hat{\hat{I}}_z, \hat{\hat{I}}_-, \hat{\hat{I}}_+$ and $\hat{\hat{E}}$. Higher spin correlation orders are given by product operators of the basis operators. The basis operators can be ordered by spin correlation order and quantum coherence order as shown in figure 3.2. The symbol $\mathfrak{L}_k$ denotes the subspace containing all spin correlation orders k, the symbol $\mathfrak{L}^k$ the subspace containing all quantum coherence orders k.

It is worth noting that the choice of basis in terms of operators, rather than Zeeman-states, is crucial for the truncation methods that will be presented. In
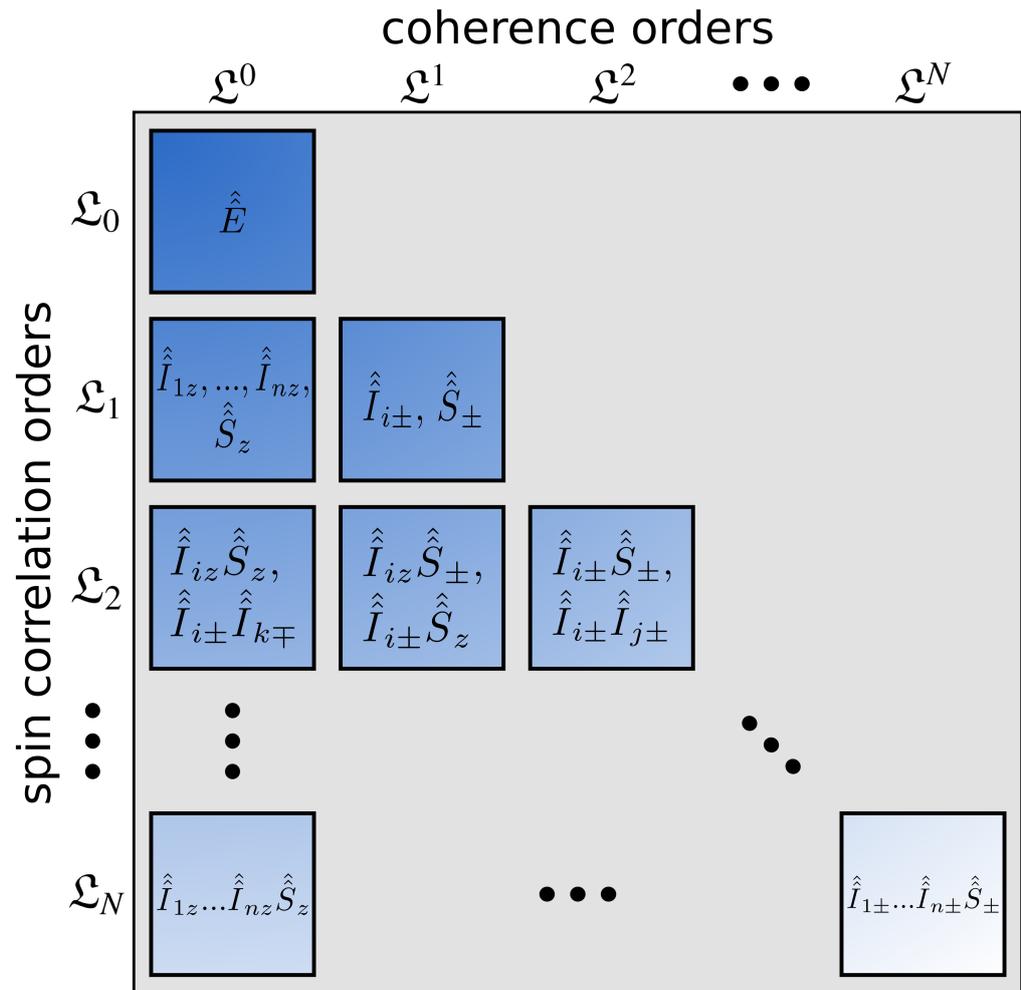
Figure 3.2: Liouville space ordered by spin correlation order and coherence order with example operators.

the next section an averaged Hamiltonian will be introduced which restricts the evolution of the density operator to the zero quantum subspace $\mathfrak{L}^0$, so the first column in figure 3.2. After that, the truncation of the basis to a certain spin correlation order will be discussed.

3.4 Averaged Hamiltonian

The dynamics of the solid effect can be modelled by an averaged Hamiltonian which restricts the system trajectory to the zero quantum subspace. The implementation of this reduces the dimension of the space by a factor of $\sim \sqrt{\pi N}$. The full theory can be found in [66], here a brief overview of the main points will be given.

3.4.1 Averaged Hamiltonian Theory

Starting point is the Hamiltonian given in section 3.1. The following theory is equivalent for both the zero and double quantum DNP transition, for the double quantum transition the nuclear spin polarisation occurs with an inverted sign. As an example the zero quantum transition case is demonstrated. A second transition of the initial Hamiltonian (3.1) into the doubly rotating frame frame gives:

$$
\begin{aligned}
\hat{\mathscr{H}}' = \sum_k & \left[A_k \hat{I}_{kz} \hat{S}_z + \frac{1}{2} B_k \left(e^{i\omega_I t} \hat{I}_{k-} + e^{-i\omega_I t} \hat{I}_{k+} \right) \hat{S}_z \right] + \frac{\omega_1}{2} \left(e^{i\omega_I t} \hat{S}_- + e^{-i\omega_I t} \hat{S}_+ \right) \\
& + \sum_{j<k} d_{jk} \left[2\hat{I}_{jk} \hat{I}_{zk} - \frac{1}{2} \left(\hat{I}_{j-} \hat{I}_{k+} + \hat{I}_{j+} \hat{I}_{k-} \right) \right] \\
& =: \hat{\mathscr{H}}_0 + e^{-i\omega_I t} \hat{\mathscr{H}}_+ + e^{i\omega_I t} \hat{\mathscr{H}}_-,
\end{aligned}
$$

where

$$\hat{\mathscr{H}}_0 = \sum_{j<k} d_{jk} \left[2\hat{I}_{jk}\hat{I}_{zk} - \frac{1}{2}\left(\hat{I}_{j-}\hat{I}_{k+} + \hat{I}_{j+}\hat{I}_{k-}\right) \right] + \sum_k A_k \hat{S}_z$$

$$\hat{\mathscr{H}}_\pm = \frac{1}{2}\sum_k B_k \hat{I}_{k\pm}\hat{S}_z + \frac{\omega_1}{2}\hat{S}_\pm.$$

A temporal transformation $\tau = \omega_I t$ of the equation of motion yields with $\dfrac{\partial|\hat{\rho}\rangle}{\partial\tau}\dfrac{\partial\tau}{\partial t} = \omega_I\dfrac{\partial|\hat{\rho}\rangle}{\partial\tau}$:

$$\frac{\partial|\hat{\rho}(\tau)\rangle}{\partial\tau} = \frac{1}{\omega_I}\left[\left(-i\hat{\mathscr{H}}'(\tau) - \hat{\Gamma}\right)|\hat{\rho}(\tau)\rangle + \hat{\Gamma}|\hat{\rho}_{th}\rangle\right]. \qquad (3.4.1)$$

This can be rewritten as

$$\frac{\partial|\hat{\rho}(\tau)\rangle}{\partial\tau} = \varepsilon\left[\left(\hat{\hat{h}}_0 + e^{-i\tau}\hat{\hat{h}}_+ + e^{i\tau}\hat{\hat{h}}_-\right)|\hat{\rho}(\tau)\rangle + \hat{\hat{\gamma}}|\hat{\rho}_{th}\rangle\right] \qquad (3.4.2)$$

introducing the positive, dimensionless parameter ε which indicates the order of magnitude of the interactions, relaxation rates and microwave power. $\hat{\hat{h}}_0, \hat{\hat{h}}_\pm$ and $\hat{\hat{\gamma}}$ are given by:

$$\hat{\hat{h}}_0 = -\frac{\hat{\hat{\Gamma}} + i\hat{\hat{\mathscr{H}}}_0}{\varepsilon\omega_I} \qquad \hat{\hat{h}}_\pm = -\frac{i\hat{\hat{\mathscr{H}}}_\pm}{\varepsilon\omega_I} \qquad \hat{\hat{\gamma}} = \frac{\hat{\hat{\Gamma}}}{\varepsilon\omega_I}$$

In this form the Krylov-Bogoliubov averaging method [67] can be applied, in order to average out the fast oscillating terms, $\hat{\hat{h}}_-$ and $\hat{\hat{h}}_+$, in (3.4.2). A more detailed description of the averaging method can be found in appendix B. The result is a Hamiltonian which only contains zero quantum coherence terms:

$$\hat{\hat{\mathscr{H}}}^{av} = \hat{\hat{\mathscr{H}}}_1 + \hat{\hat{\mathscr{H}}}_2 + \hat{\hat{\mathscr{H}}}_3,$$

where $\quad \hat{\hat{\mathscr{H}}}_1 = \hat{\hat{\mathscr{H}}}_0,$

$$\hat{\hat{\mathscr{H}}}_2 = \frac{1}{\omega_I}\left[\hat{\hat{\mathscr{H}}}_+, \hat{\hat{\mathscr{H}}}_-\right]$$

$$= \frac{1}{4\omega_I}\left(\left[\frac{1}{2}\sum_k B_{k+}\hat{\hat{I}}_+, \frac{1}{2}\sum_k B_{k-}\hat{\hat{I}}_-\right]\right. \qquad (3.4.3)$$

$$\left. + 2\omega_1^2\hat{\hat{S}}_z - 2\omega_1\left(\frac{1}{2}\sum_k B_{k-}\hat{\hat{I}}_-\hat{\hat{S}}_+ + \frac{1}{2}\sum_k B_{k+}\hat{\hat{I}}_+\hat{\hat{S}}_-\right)\right),$$

and $\quad \hat{\hat{\mathscr{H}}}_3 = \frac{1}{\omega_I^2}\left(\hat{\hat{\mathscr{H}}}_+\left[\hat{\hat{\mathscr{H}}}_-, \hat{\hat{L}}_0\right] + \hat{\hat{\mathscr{H}}}_-\left[\hat{\hat{\mathscr{H}}}_+, \hat{\hat{L}}_0\right]\right),$

with $\quad \hat{\hat{L}}_0 = i\hat{\hat{\Gamma}} - \hat{\hat{\mathscr{H}}}_0.$

Note that the last term of $\hat{\hat{\mathcal{H}}}_2$ contains the expression for the effective microwave strength $s\omega_1 = \frac{1}{2}\omega_1|B_\pm|\omega_I^{-1}$, found by S.Vega and co-workers [56].

As the initial thermal equilibrium state belongs to the zero quantum subspace the trajectory of the state vector will remain in this subspace for all times. In SPINACH it is easy to discard the subspaces of higher coherence order by multiplication of the Liouvillian and density operator with a suitable projection operator before the evolution is calculated. The effect of the averaged Hamiltonian can be seen in figure (3.3): all the components of the density operator outside the zero quantum coherence subspace remain zero, additionally the fast oscillations are averaged out. Although it appears in figure (3.3) that the norm decreases, this is just an initial dip. Over the course of a full DNP simulation to the steady state, the norm of the density operator increases to values of larger than one. This is expected as the nuclear polarisation builds up due to the system receiving energy in the form of microwaves.

3.4.2   Error associated with the averaged Hamiltonian

The Hamiltonian given in (3.4.3) contains up to 3rd order averaging terms. In the following section it will be shown that the 3rd order approximation is indeed sufficient for all parameters encountered in the simulations. The averaged Hamiltonian has been tested for a wide range of input parameters. This includes the microwave power ω_1, the interaction strengths A_k, B_k, d_{jk} and the relaxation parameters $r_{1n}, r_{2n}, r_{1e}, r_{2e}$. For error analysis a comparison to the evolution of the system under the full Liouvillian is needed. Due to the memory requirements of this full Liouvillian, the analysis was limited to spin systems containing up to six spins, so five nuclei and one electron. Seven spins would have been possible but the simulation time would have become unreasonably large. In figure 3.4 the polarisation build up for a spin system under the influence of a full Hamiltonian and the residual of $|\rho(t)\rangle_{|\hat{\hat{\mathcal{H}}}} - \rho(t)_{|\hat{\hat{\mathcal{H}}}^{av}}$, corresponding to the polarisation
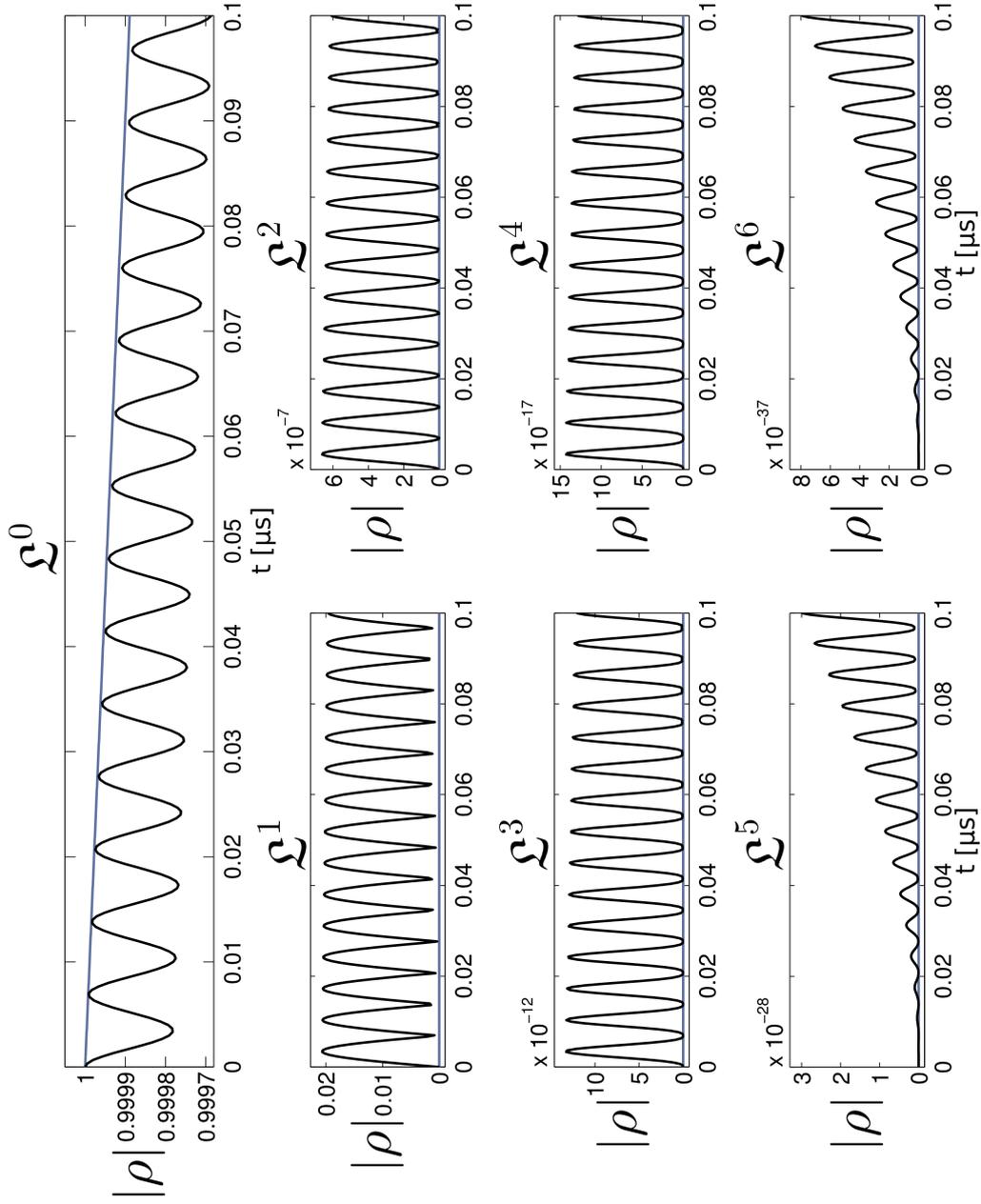
Figure 3.3: Evolution of the norm squared for the different quantum coherence subspaces. Comparison of the averaged Hamiltonian (blue line) *vs.* the full Hamiltonian (black line) . The dynamics are shown for the first $0.1\mu s$ in order to resolve the small oscillations of the norm evolving under the full Hamiltonian.

build-up under the influence of $\hat{\hat{\mathcal{H}}}$ minus the polarisation build-up under the influence of $\hat{\hat{\mathcal{H}}}^{av}$ is shown for three different sets of input parameters. The simulation parameters are given in the figure caption. The errors associated with the simulations shown in 3.4 are listed in Table 3.1. The absolute error of the spin system evolving under the averaged Hamiltonian is on the order of 10^{-3} or smaller in all cases. Additional error analysis of a large range of input parameters is given in appendix C. For these input parameters the largest absolute error encountered is on the order of 10^{-3}, in most cases the largest relative error is around 1% or less. When the relative error is larger, it turns out that the polarisation build-up for the tested input parameters is very small, hence resulting in a division by a small number, making the relative error large.

Table 3.1: Errors of the simulations shown in figure 3.4. The errors shown are the largest error over the time of the simulation.

	relative error [%]	absolute error
a	0.7	$4.5 \cdot 10^{-3}$
b	0.6	$2.4 \cdot 10^{-3}$
c	0.8	$2.5 \cdot 10^{-3}$

3.4.3 Conclusions

The use of averaging Hamiltonians has previously been presented by Haeberlen and Waugh [68]. Their approach was applied for the investigation of periodic pulse sequences that would result in averaging of spin interactions. In their strategy only coherent mechanisms are considered, whereas in the case of the solid effect relaxation is caused by incoherent fluctuations of the local magnetic field around the spins, as was discussed in section 3.2. The incoherent effects

are accounted for using the KBA method described above.

The main advantage of using the averaged Hamiltonian is that it confines the trajectory of the density operator to the zero quantum subspace. It can be shown that the dimension of a subspace with coherence order q is given by

$$\dim(\mathfrak{L}^q) = \binom{N+q}{2N} = \frac{(2N)!}{(N-q)!(N+q)!},$$ (3.4.4)

where N is the number of spins in the simulation. As a result, the dimension of the Liouvillian can a priori be reduced to

$$\dim(\mathfrak{L}^0) = \frac{(2N)!}{(N!)^2} \sim \frac{4^N}{\sqrt{\pi N}}.$$

For the last step the Stirling formula has been used. This truncation translates into a significant reduction of processing time, for example for the simulations shown in figure 3.4 from around 45 minutes to 30 seconds.

There is an additional factor that plays a role in the reduction in simulation time. The largest terms in the full Hamiltonian are on the order of the nuclear Larmor frequency ω_I, whereas one can see from equation 3.4.3 that the averaged Hamiltonian contains only the smaller spin spin interaction, relaxation and microwave terms scaled by the inverse of ω_I and higher orders thereof. This has a positive effect on the calculation of the propagator by reducing the scaling factor s and hence the number of squaring steps, so matrix multiplications, that SPINACH has to carry out. The fact that the high frequency modulations have been removed by the averaged Hamiltonian has also been seen in figure 3.3.

In the derivation of the averaged Hamiltonian the condition $\Delta = \pm\omega_I$ has been assumed, which means the microwave frequency was chosen to be on resonant with the DNP frequency. The application of the KBA strategy is not strictly limited to this condition but can be used for slightly off-resonant irradiation, as long as the deviation is small, for example up to 20% of $|\omega_I|$.

The KBA averaging method is not restricted to the application of the solid effect only. Progress has been made recently by A. Karabanov to also formulate

the Cross Effect Hamiltonian in this way. The requirement using the averaged method is, that all spin interactions and relaxation constants remain small with respect to the nuclear Larmor frequency. The most critical parameter for the cross effect is hence the electron dipole interaction constant but it has been found in initial tests, that even with values of up to 25 MHz, accurate results are still obtained, making it possible to consider bi-radicals. The subspace to which the trajectory is confined to in this case contains all basis elements which commute with $\omega_I(\sum_k \hat{I}_{kz} + \hat{S}_{k2})$, where $\hat{S}_{k2}$ is the electron which is on the same offset frequency as the nucleus. This work will be presented in a future publication after systematic testing of all input parameters has been carried out.
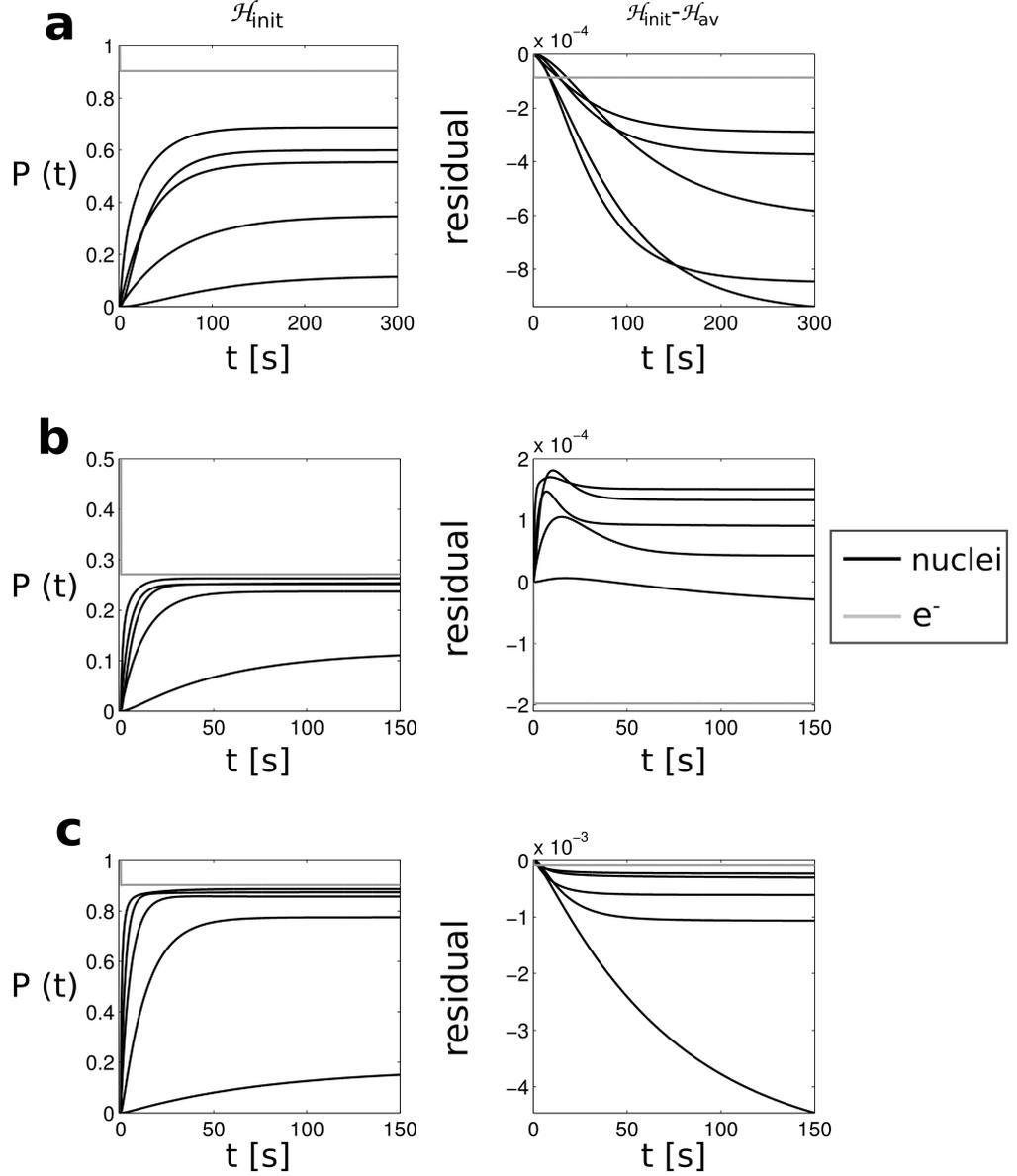
Figure 3.4: The polarization build-up and the corresponding error dynamics for various input parameters. Left: evolution of polarisations under the initial Hamiltonian. Right: difference between polarisation build up using initial and averaged Hamiltonian. **(a)** $\omega_1 = 1.5\,\text{MHz}$. **(b)** $\omega_1 = 5\,\text{MHz}$. **(c)** Nucleus-electron distances halved, which results in an eight times increase in the hyperfine interaction strength. The microwave strength has been set back to $\omega_1 = 1.5\,\text{MHz}$. Simulation parameters: 5 protons and one e^- in a pyramid configuration (see appendix C.1), relaxation parameters: $r_{1n} = 0.01\,\frac{\text{rad}}{\text{s}}$, $r_{2n} = 10\,\frac{\text{rad}}{\text{s}}$, $r_{1e} = 10^3\,\frac{\text{rad}}{\text{s}}$, $r_{2e} = 10^6\,\frac{\text{rad}}{\text{s}}$.

65

3.5   Basis truncation

Throughout the DNP process, higher spin correlations get populated due to the action of the orientation dependent Hamiltonians. At the same time, the relaxation operator ensures the depletion of these higher correlation order states, so that a steady state balance is reached. It turns out that due to relaxation, higher spin correlation order states are weakly populated, making it possible to truncate the basis of the density operator and Liouvillian to a certain order ([62, 66]). As a result the propagator size scales polynomially as opposed to exponentially (see figure 3.5). In this section the theory and numerical results justifying the basis truncation are presented. Firstly the conditions for basis truncation to a certain spin correlation order will be derived. It will be shown that the ratio of the relaxation and interaction parameters for a given spin system plays an important role in determining the largest order to which the basis operators have to be kept. Then numerical results, confirming the basis truncation conditions will be presented.

3.5.1   Basis truncation theory

Hamiltonians in general can be divided into two categories, either containing a single spin operator or products of two spin operators. Examples for the single spin Hamiltonian are the Zeeman interaction and the Microwave or RF Hamiltonian. Two spin Hamiltonians describe couplings, for example the nuclear dipole dipole coupling or the hyperfine interaction. One can section the Liouville space into spin order subspaces such that the direct sum of these subspaces give the full state space again:

$$\mathfrak{L} = \mathfrak{L}_0 \oplus \mathfrak{L}_1 \oplus \ldots \oplus \mathfrak{L}_k \oplus \ldots \oplus \mathfrak{L}_N,$$

where N is the number of spins, and k is the number of operators in the product basis. For example, $\mathfrak{L}_0$ contains only the unity operator $\hat{\mathrm{E}}$, whereas the single
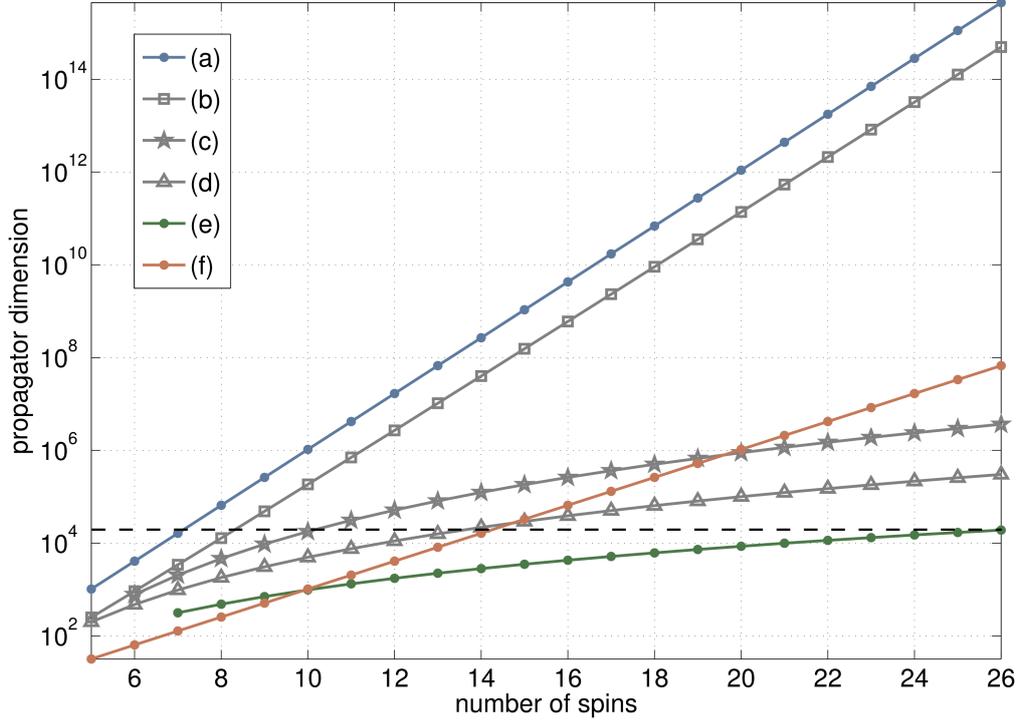
Figure 3.5: Scaling of the propagator size with number of spins for the cases of using the full basis in the Liouville space (a) and the averaged Hamiltonian (b) as well as the averaged Hamiltonian plus basis truncation: (c) 5th order, (d) 4th order and (e) 3rd order basis truncation. The scaling for the Hamiltonian in the Hilbert space is also shown (f). One can see that for eleven spins using the averaged Hamiltonian and 3rd order basis truncation the scaling becomes more favourable than the Hilbert space scaling. The black dashed line indicates the limit for a computer with 8 GB RAM.

spin subspace contains $\hat{\hat{S}}_{\pm}$, $\hat{\hat{S}}_z$ and $\hat{\hat{I}}_{k\pm}$, $\hat{\hat{I}}_{kz}$(see figure 3.2). The result of a single spin Hamiltonian $\hat{\hat{\mathscr{H}}}_{SO}$ acting on a subspace of a given spin correlation remains within this subspace:

$$\hat{\hat{\mathscr{H}}}_{SO}\mathfrak{L}_k \subset \mathfrak{L}_k.$$

This is due to the fact that $\hat{\hat{\mathscr{H}}} = \left[\hat{\mathscr{H}}, \hat{E}\right]$, and a commutator containing two single spin operators will never result in an operator containing more than one spin. Using the same considerations one can see that a double spin Hamiltonian

$\hat{\hat{\mathscr{H}}}_{DO}$ can change the spin correlation order k by plus or minus one, or it can leave it unchanged:

$$\hat{\hat{\mathscr{H}}}_{DO}\mathfrak{L}_k \subset \mathfrak{L}_{k-1} \oplus \mathfrak{L}_k \oplus \mathfrak{L}_{k+1}.$$

The relaxation operator defined in section 3.2 contains only single spin orders, so its action also remains confined to the same subspace.

$$\hat{\hat{\Gamma}}\mathfrak{L}_k \subset \mathfrak{L}_k.$$

The density operator can also be expressed as a sum of the different spin order contributions: $|\hat{\rho}\rangle = |\hat{\rho}_1\rangle + |\hat{\rho}_2\rangle + ...|\hat{\rho}_N\rangle$. Using this notation one can rewrite the Liouville-von-Neuman equation of motion as

$$\frac{\mathrm{d}}{\mathrm{d}t}|\hat{\rho}_1\rangle = -i\hat{\hat{\mathscr{H}}}_{SO}|\hat{\rho}_1\rangle - i\hat{\hat{\pi}}_1\hat{\hat{\mathscr{H}}}_{DO}(|\hat{\rho}_1\rangle + |\hat{\rho}_2\rangle) + \hat{\hat{\Gamma}}\left(|\hat{\rho}_1\rangle - |\hat{\rho}_{eq}\rangle\right)$$

$$\ldots$$

$$\frac{\mathrm{d}}{\mathrm{d}t}|\hat{\rho}_k\rangle = -i\hat{\hat{\mathscr{H}}}_{SO}|\hat{\rho}_k\rangle - i\hat{\hat{\pi}}_k\hat{\hat{\mathscr{H}}}_{DO}\left(|\hat{\rho}_{k-1}\rangle + |\hat{\rho}_k\rangle + |\hat{\rho}_{k+1}\rangle\right) + \hat{\hat{\Gamma}}|\hat{\rho}_k\rangle$$

$$\ldots$$

$$\frac{\mathrm{d}}{\mathrm{d}t}|\hat{\rho}_N\rangle = -i\hat{\hat{\mathscr{H}}}_{SO}|\hat{\rho}_N\rangle - i\hat{\hat{\pi}}_N\hat{\hat{\mathscr{H}}}_{DO}\left(|\hat{\rho}_{N-1}\rangle + |\hat{\rho}_N\rangle\right) + \hat{\hat{\Gamma}}|\hat{\rho}_N\rangle,$$

where $\hat{\hat{\pi}}_k$ is a superoperator projecting the Hamiltonian into the kth order subspace. As an approximation, the thermal equilibrium density operator resides in $\mathfrak{L}_1$, which is reasonable as the electron thermal polarisation is much larger than the nuclear polarisation. Hence one can neglect the higher order terms and assume that $|\hat{\rho}_{eq}\rangle = \hat{\hat{S}}_z$. In order to investigate to which extent the higher spin order terms become populated during the simulation, it is instructive to observe the norm of the density operator in the various subspaces. With $|\hat{\rho}_k|^2 = \langle \hat{\rho}_k, \hat{\rho}_k\rangle$,

$\langle X, Y \rangle = Tr\{X^*, Y\}$ and $i\langle X, \hat{\mathscr{H}}_{DO}Y \rangle = -i\langle Y, \hat{\mathscr{H}}_{DO}X \rangle$ one gets

$$\frac{\mathrm{d}}{\mathrm{d}t}|\hat{\rho}_1|^2 = -2\mathfrak{Im}\left(\langle \hat{\rho}_2, \hat{\mathscr{H}}_{DO}\hat{\rho}_1 \rangle\right) + 2\langle \hat{\rho}_1, \hat{\Gamma}\hat{\rho}_1 \rangle - 2\mathfrak{Re}\left(\langle \hat{\rho}_1, \hat{\Gamma}\hat{\rho}_{eq} \rangle\right)$$

$$\dots$$

$$\frac{\mathrm{d}}{\mathrm{d}t}|\hat{\rho}_k|^2 = -2\mathfrak{Im}\left(\langle \hat{\rho}_k, \hat{\mathscr{H}}_{DO}(\hat{\rho}_{k-1} + \hat{\rho}_{k+1}) \rangle\right) + 2\langle \hat{\rho}_k, \hat{\Gamma}\hat{\rho}_k \rangle$$

$$\dots$$

$$\frac{\mathrm{d}}{\mathrm{d}t}|\hat{\rho}_N|^2 = -2\mathfrak{Im}\left(\langle \hat{\rho}_N, \hat{\mathscr{H}}_{DO}\hat{\rho}_{N-1} \rangle\right) + 2\langle \hat{\rho}_N, \hat{\Gamma}\hat{\rho}_N \rangle,$$

where $\mathfrak{Re}(x)$ denotes the real part, and $\mathfrak{Im}(x)$ the imaginary part of x. The action of the single spin Hamiltonian has disappeared from the equations. One can remove the double spin Hamiltonian and the relaxation operator from the equations by using eigenvalue equations for the particular subspace. Then

$$\frac{\langle \hat{\rho}_1, \hat{\Gamma}\hat{\rho}_{eq} \rangle}{|\hat{\rho}_1|} = g \quad \frac{\langle \hat{\rho}_k, \hat{\Gamma}\hat{\rho}_k \rangle}{|\hat{\rho}_k|} = r_k x_k \quad i\frac{\langle \hat{\rho}_k, \hat{\mathscr{H}}_{DO}\hat{\rho}_j \rangle}{|\hat{\rho}_k|} = C_{kj}x_j,$$

where r_k is the average eigenvalue of the projection of the relaxation operator into the kth subspace and C_{kj} is a transfer rate between the kth and j^{th} subspace. With $\frac{\mathrm{d}}{\mathrm{d}t}|\hat{\rho}_k|^2 = 2|\hat{\rho}_k|\frac{\mathrm{d}}{\mathrm{d}t}|\hat{\rho}_k|$ and using the notation $x_k = |\hat{\rho}_k|$ one gets

$$\frac{\mathrm{d}}{\mathrm{d}t}x_1 = -c_2 x_2 - r_1 x_1 + g$$

$$\dots$$

$$\frac{\mathrm{d}}{\mathrm{d}t}x_k = -c_k x_{k-1} - c_{k+1}x_{k+1} - r_k x_k \tag{3.5.1}$$

$$\dots$$

$$\frac{\mathrm{d}}{\mathrm{d}t}x_N = -c_N x_{N-1} - r_N x_N.$$

The parameters c_k depend on the transition coefficients C_{kj}. In the next paragraph it will be shown that the average eigenvalue of the kth subspace of the relaxation operator is proportional to $2r_0 k$, where r_0 contains the dominant electron r_{2e} of the relaxation operator. The coefficients c_k can be replaced by a constant c_0, as the transition rates of $\hat{\mathscr{H}}_{DO}$ do not strongly depend on the spin order. These parameters will be discussed in more detail below.

Equations (3.5.1) can be combined into a single dissipative transport equation, describing the flow of magnetisation through the spin order subspaces, if the number of spins is large:

$$\frac{\partial x}{\partial t} = -c_0 \frac{\partial x}{\partial \kappa} - 2r_0 \kappa x + g(\kappa). \tag{3.5.2}$$

The coefficient κ now describes the spin correlation order and $g(\kappa) = g_0 \delta(\kappa - 1)$ is the thermal correction factor which is only non-zero for $\kappa = 1$. The steady state solution of 3.5.2 is obtained by setting the left hand side to zero and integrating with respect to κ:

$$x_\infty(\kappa) = x_0 \exp\left(-\frac{r_0}{c_0}\kappa^2\right), \tag{3.5.3}$$

with $x_0 = \frac{g_0}{c_0} H(x-1) \exp\left(\frac{r_0}{c_0}\right)$, where $H(x-1)$ is the Heaviside step function. It can be seen from equation(3.5.3) that the norm decreases quadratically with spin correlation order. Hence it is possible to truncate the basis to a certain spin correlation order without influencing the lower order dynamics appreciably. The error ξ incurred from truncation at a certain spin correlation order level κ is then given by

$$\frac{\int\limits_m^\infty \exp\left(-\chi\kappa^2\right) d\kappa}{\int\limits_1^\infty \exp\left(-\chi\kappa^2\right) d\kappa} = \frac{\mathrm{erfc}(\sqrt{\chi}m)}{\mathrm{erfc}(\sqrt{\chi})} \leq \xi \quad \text{using } \chi = \frac{r_0}{c_0}. \tag{3.5.4}$$

The parameter χ, the ratio of relaxation to interaction strength in a spin system, indicates the ratio of depletion and population of the correlation order subspaces. The larger χ, the smaller the amount of magnetisation that can be expected to be transferred to the higher correlation order subspaces and hence one can expect to be able to truncate the Liouville space at a lower spin correlation order, whilst incurring only a small error. In turn, for a small χ, corresponding to small relaxation rates and a large transfer rate of magnetisation into higher spin correlation orders, the basis truncation order can expected to be higher. This is illustrated in figure 3.8.

Coefficients of the basis truncation error estimate

As indicated above, in order to find the largest error that is incurred by truncating the basis to a certain spin correlation order k, one has to consider the largest transfer rate of magnetisation into higher spin correlation orders by $\hat{\mathscr{H}}_{DO}$ and the smallest relaxation from these higher orders, which means when χ is minimal. The coefficients r_k in (3.5.1) had been replaced by $2r_0k$ in the dissipative transport equation. r_0 can be estimated using the following considerations: The average relaxation rate for each subspace $\mathfrak{L}_k$ can be calculated from

$$r_k = \left\langle \frac{\left|\hat{\hat{\Gamma}}\hat{O}_k\right|}{\left|\hat{O}_k\right|} \right\rangle,\tag{3.5.5}$$

where the average is over all basis operators $\hat{O}_k$ contained in the kth subspace. The electronic transverse relaxation rate by far dominates $\hat{\hat{\Gamma}}$, hence r_k can be estimated by splitting the basis operators in terms containing $\hat{\hat{S}}_{\pm}$ and terms not containing $\hat{\hat{S}}_{\pm}$:

$$\frac{\left|\hat{\hat{\Gamma}}\hat{O}_k\right|}{\left|\hat{O}_k\right|} \geq r_{2e} \quad \text{for} \quad \hat{O}_k = \hat{\hat{S}}_{\pm} \prod_{j}^{k-1} \hat{\hat{I}}_{\alpha j}$$

$$\frac{\left|\hat{\hat{\Gamma}}\hat{O}_k\right|}{\left|\hat{O}_k\right|} > 0 \quad \text{for} \quad \hat{O}_k \neq \hat{\hat{S}}_{\pm} \prod_{j}^{k-1} \hat{\hat{I}}_{\alpha j}$$

where α can be z and $\pm$. As the number of $\hat{\hat{S}}_{\pm}$ operators contained in the subspace grows linearly with the spin order this results in

$$r_k \geq \frac{2k}{3N}r_{2e}, \quad \text{so} \quad r_0 \geq \frac{r_{2e}}{3N}.\tag{3.5.6}$$

From figure 3.6a it can be seen that r_k is indeed linearly proportional to k and that the relation from equation (3.5.6) is very close to being an equality. This is due to the fact that the electronic relaxation rate r_{2e} is much larger than the other rates in the relaxation operator. The average eigenvalues of the relaxation operator defined in section 3.2 do not depend very strongly on the hyperfine

interaction constants as the electronic relaxation rates dominate over the nuclear rates. For the relaxation operator from figure 3.6a $r_0 = 4.8 \cdot 10^4 \frac{rad}{s}$ with $r_{2e} = 10^6 \frac{rad}{s}$. When the averaged Hamiltonian from section 3.4.1 is used, the basis is restricted to comprising only zero quantum coherence operators. This influences the estimation for r_0 but it can be seen from figure 3.6b that the slope of the curve is then larger than $\frac{2r_{2e}}{3N}$, hence the relation in 3.5.6 remains true.

(a)   (b)
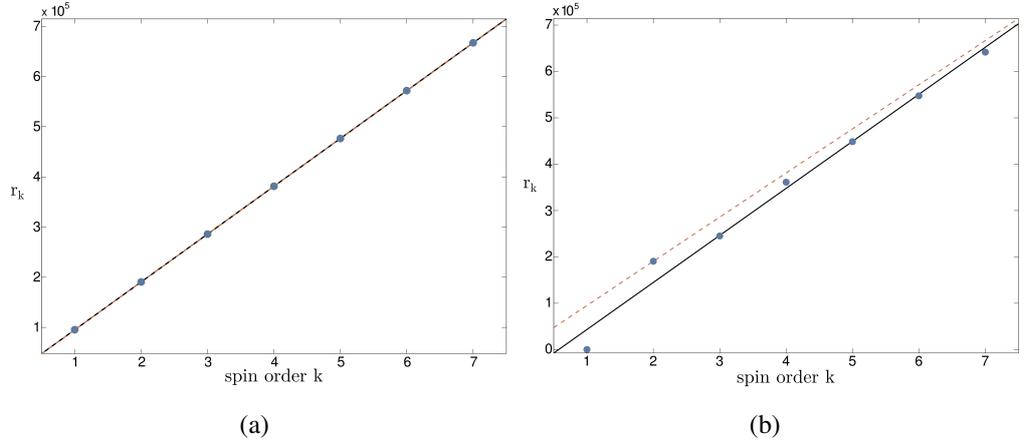
Figure 3.6: Average eigenvalue r_k of the full (a) and the zero quantum truncated (b) relaxation operator for the different spin order subspaces. The blue dots represent the calculated average eigenvalue in units of $\frac{rad}{s}$, the black line a linear fit to the average eigenvalues and the orange dashed line the theoretically predicted curve with slope $\frac{r_{2e}}{3N}$.

For c_0 one needs to find an upper limit in order to minimise χ and hence find the upper limit for ξ. The transfer amplitudes from one spin order subspace to another depend strongly on the hyperfine and dipolar interaction strengths. In figure 3.7 the transfer amplitudes of an interaction Hamiltonian $\hat{\hat{\mathscr{H}}}_{DO}$ of a chain of nuclei with the electron at the origin is shown where the transition amplitude is defined analogously as in [5], for example for the transition from $\mathfrak{L}_1$ to $\mathfrak{L}_2$:

$$\langle \hat{\hat{O}}_k | \hat{\hat{\mathscr{H}}}_{DO} | \hat{\hat{O}}_j \hat{\hat{O}}_k \rangle \qquad j, k = \in [1,N]. \qquad (3.5.7)$$

The chain has been rotated from $\theta = 0$, which corresponds to being aligned

with the z axis, to $\theta = \arccos\left(\frac{1}{\sqrt{3}}\right)$, which corresponds to the magic angle. One can see that for the magic angle and close to the magic angle the largest transfer amplitude is equal for all spin orders, whereas for the angles where the hyperfine constant A_k is non-zero a non trivial dependency of the transfer rate on the spin order occurs. From figure 3.7 one can see that the transition amplitude
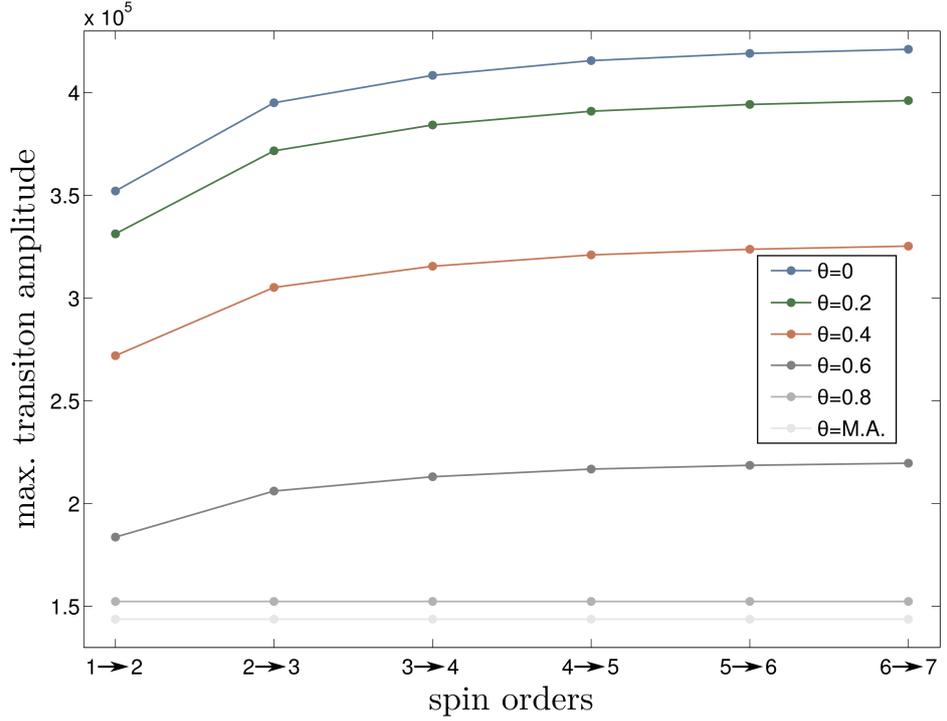
Figure 3.7: The largest transition amplitude in units of $\frac{rad}{s}$ for the interaction Hamiltonian $\hat{\hat{\mathscr{H}}}_{DO}$ for a chain of six nuclei with one electron at the centre is shown. The distance between the spins is 12Å. The angle is given in radians, where $\theta_{MA} = 0.9553$. One can see that for the angles that corresponds to small constants A_k in the hyperfine Hamiltonian the transition amplitude does not change with spin order k. For terms where A_k is non-zero a non-trivial dependency is present.

converges to a constant value for a large spin orders. The following estimate holds well as an upper bound for the largest transfer amplitude. The terms of the hyperfine and dipole dipole interaction can assumed to be smaller than or

equal to

$$A = \max_k \sqrt{A_k^2 + |B_k|^2} \quad \text{and} \quad d = \sqrt{6} \max_k |d_{jk}|.$$

The constant c_0 has therefore got the bound

$$c_0 < \frac{2A(N-1) + 2d\binom{N-1}{2}}{\binom{N}{2}} = \frac{4A + 2d(N-2)}{N}. \tag{3.5.8}$$

Table 3.2 summarises the largest Eigenvalue of $\hat{\hat{\mathcal{H}}}_{DO}$ for the chain example of figure 3.7 and the corresponding upper bound for c_0 from (3.5.8). The relation always holds, so is suitable as an upper limit.

Table 3.2: Comparison of the largest transfer amplitude of $\hat{\hat{\mathcal{H}}}_{DO}$ with the upper bound estimate 3.5.8 for c_0.

θ [rad]	largest transfer amplitude in $\hat{\hat{\mathcal{H}}}_{DO}$	c_0 from (3.5.8)
0	$4.14 \cdot 10^5$	$4.21 \cdot 10^5$
0.2	$3.96 \cdot 10^5$	$4.01 \cdot 10^5$
0.4	$3.25 \cdot 10^5$	$3.66 \cdot 10^5$
0.6	$2.20 \cdot 10^5$	$3.17 \cdot 10^5$
0.8	$1.52 \cdot 10^5$	$2.65 \cdot 10^5$
$\arccos\left(\frac{1}{\sqrt{3}}\right)$	$1.44 \cdot 10^5$	$2.32 \cdot 10^5$

3.5.2   Basis truncation error analysis

Having obtained expressions for the parameters c_0 and r_0, that can be calculated before the start of the simulation of the evolution of a spin system, one can calculate the lowest spin correlation order m_* that has to be kept in order to obtain the result within a user defined tolerance ξ. This m_* can be obtained from equation (3.5.4):

$$m \geq m_* = \frac{1}{\sqrt{\chi}}\,\mathrm{erfc}^{-1}\left(\xi\,\mathrm{erfc}\left(\sqrt{\chi}\right)\right) \qquad (3.5.9)$$

with

$$\mathrm{erfc}(x) = \frac{2}{\sqrt{\pi}}\int_x^\infty e^{-\tau^2}\,\mathrm{d}\tau.$$

In order to obtain the dissipative transport equation (3.5.2), the limit for $N \ll 1$ was taken, hence the bound m_* for the basis truncation is only fully valid when it is much smaller than the number of spins in the system. The lowest limit for m_* is three, as the spin interaction Hamiltonian which contains bilinear terms would not be able to cause a transfer from the two spin order subspace to the higher spin order spaces.

Scaling of χ

Equation (3.5.9) depends strongly on χ, as can be seen from figure 3.8, where the tolerance ξ has been set to 0.05, corresponding to a relative error of 5 %. For $\chi \geq 0.29$ third order basis truncation can safely be used as this is the lowest limit. If m_* becomes equal to or larger than the number of spins, safe truncation is not possible. It will be discussed later that although equation (3.5.9) gives the lower limit for truncation, in some cases a smaller basis does also produce accurate results.

In order to test equation (3.5.9) a comparison with the full basis is necessary for the error analysis. As the averaged Hamiltonian has been found to produce a very good approximation also with restricted basis, it was used for all error
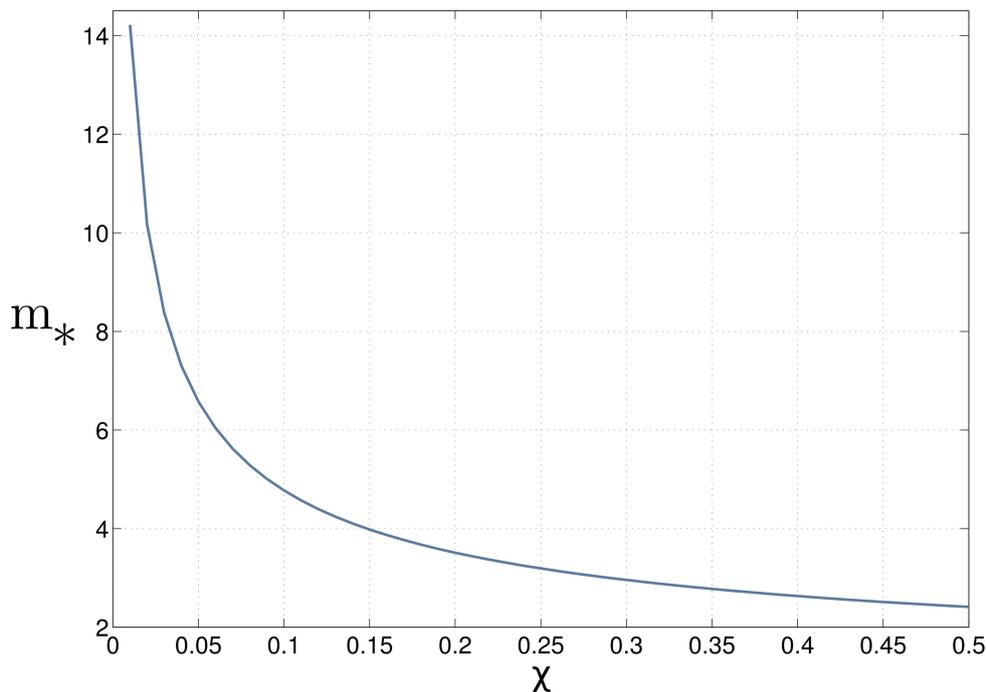
Figure 3.8: The lower bound for basis truncation m_* for different parameters χ. The tolerance ξ is set to 0.05. In practice the basis truncation order m is an integer, and in order to err on the side of caution m_* should always be rounded up.

analysis of the basis truncation. The largest number of spins that can be tested within the constraints of the 8 GB memory card using the averaged Hamiltonian is eight but this is involves long processing times, hence most analysis has been carried out with six nuclei and one electron.

The estimate in equation (3.5.9) has been tested systematically by scaling the parameter χ by a factor s, so $\chi = \chi_0/s$. This was done either by dividing the relaxation parameter r_{2e} by s, keeping c_0 constant or by scaling the coordinates by $s^{\frac{1}{3}}$, which translates into a linear scaling of c_0. The factor s was chosen in such a way that the resulting m_* would cover the whole range of possible basis truncations, so for a seven spin system from the third to sixth order.

Several random configurations were tested this way and to start with ^{1}H nuclei

were used in the simulation as a 'worst case' as the interaction constants are the largest. The error that was calculated for each basis truncation level $m \in [3,6]$, and each scaling parameter s, is of the form

$$e = \left| \max_i \left| \frac{P(i)_\infty|_m}{P(i)_\infty} \right| - 1 \right|, \quad i \in [1,N] \tag{3.5.10}$$

where $P(i)_\infty$ is the steady state polarisation of spin i and $P(i)_\infty|_m$ the steady state polarisation for spin i obtained with basis truncation to level m. The error e should not exceed the factor ξ in (3.5.4) for a fixed basis truncation level m. The steady state polarisation was used because the solution to the transport equation of magnetisation to higher ranks, equation (3.5.3), was given for the steady state.

The randomly generated configurations have the following boundary conditions: The electron sits at the origin and the nuclei are distributed within an eighth of a sphere of outer radius $r_{max} = 24$ Å and a minimum distance from the electron of $r_{min} = 12$ Å. The individual positions where calculated using the MATLAB pseudorandom integer generator, *randi()*, with the limits

$$r \in [12,24] \qquad \theta \in [0, \frac{\pi}{2}] \qquad \phi \in [0, \frac{\pi}{2}].$$

In order to circumvent nuclei accidentally being placed on the same position and to avoid an unrealistically large nuclear dipole interaction, the minimum distance between all nuclei was set to be larger or equal than 5 Å. The maximum and minimum radius where chosen to result in a range of realistic interaction constants. In figure 3.9 one can see the resulting error e for one of these configurations, where ξ is also displayed for all scaling parameters s. One can see that the error e always remains below the error estimate ξ for each χ, meaning that if one calculates the lower limit for basis truncation m_* according to (3.5.9), one will obtain a basis truncation level that will reliably return an error e smaller than a user defined ξ. One can see from figure 3.9 that for larger χ the error tolerance estimate and the actual error e are similar but for small χ the estimated error becomes much larger than the actually incurred error. This
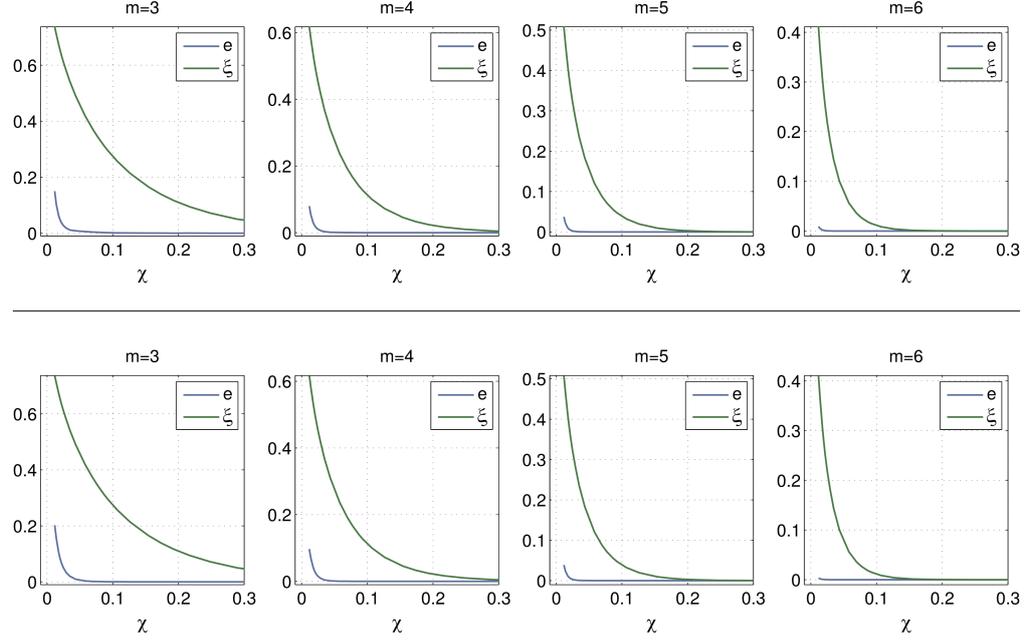
Figure 3.9: Error tolerance ξ and steady state error e for scaled χ for each basis truncation level m. The top row shows a scaling of χ by changing c_0, in the bottom row the electron transversal relaxation rate r_{2e} has been scaled. The initial c_0 was 15 kHz, the initial $r_0 = 7.5$ kHz.

results in overestimation of the needed spin order level, for example if one takes m=3 in figure 3.9, the parameter χ for which the error becomes larger than 5%, $\chi(e \gtrsim 0.05) = 0.019$, results in a recommended truncation level of $m_* = 10.4$, which is larger than the number of spins. With some configurations this overestimation was less extreme than with others, but all configurations obeyed the trend from figure 3.9 that e is smaller than ξ. Still, equation (3.5.9) is meant to provide a lower estimate of the basis truncation level, which it reliably does. In practice one would calculate χ for a given set of interaction and relaxation parameters and decide on the level of basis truncation with equation 3.5.9.

Even although the error tolerance ξ is calculated from the the steady state distribution of magnetisation across the spin orders, it turns out that the largest error over the whole time course of the simulation, although larger than the steady
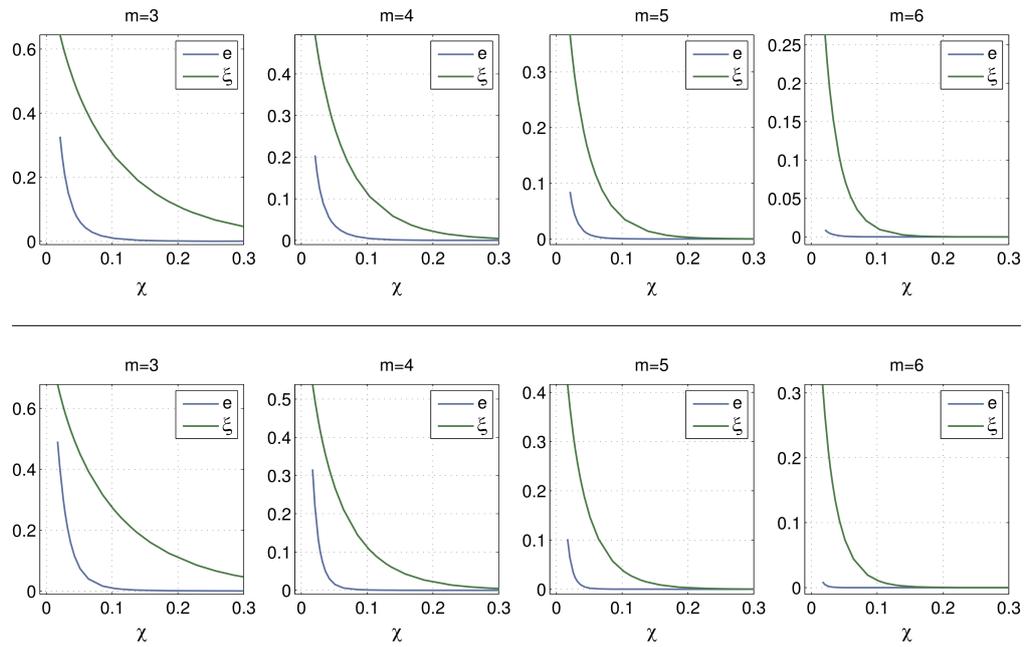
Figure 3.10: Error tolerance ξ and error e for scaled χ for each basis truncation level m over the full time course of the simulation. The top row shows a scaling of c_0, in the bottom row the electron transversal relaxation rate r_{2e} has been scaled.

state error, also remains smaller than the error tolerance ξ, as can be seen in figure 3.10.

The microwave field strength ω_1, and the remaining relaxation parameters (r_{1n}, r_{2n} , r_{1e}) were also scaled but no significant dependency of the error was seen. The dependency of the basis truncation level on the ratio $\frac{r_0}{c_0}$ was additionally checked by simultaneously scaling r_{2e} and c_0 by the parameter s, keeping χ constant. The starting parameters were chosen in such a way that the initial $\chi = 0.29$, ensuring that the third order basis truncation returned an error of less than 5%. In figure 3.11 one can see that the error remains small and largely constant for each basis truncation order, the largest absolute error encountered is on the order of 10^{-3}, the parameter is $\chi = 0.29$ for all scaling factors s. This confirms that indeed the ratio $\frac{r_0}{c_0}$ is the main indicator for the basis truncation limit.
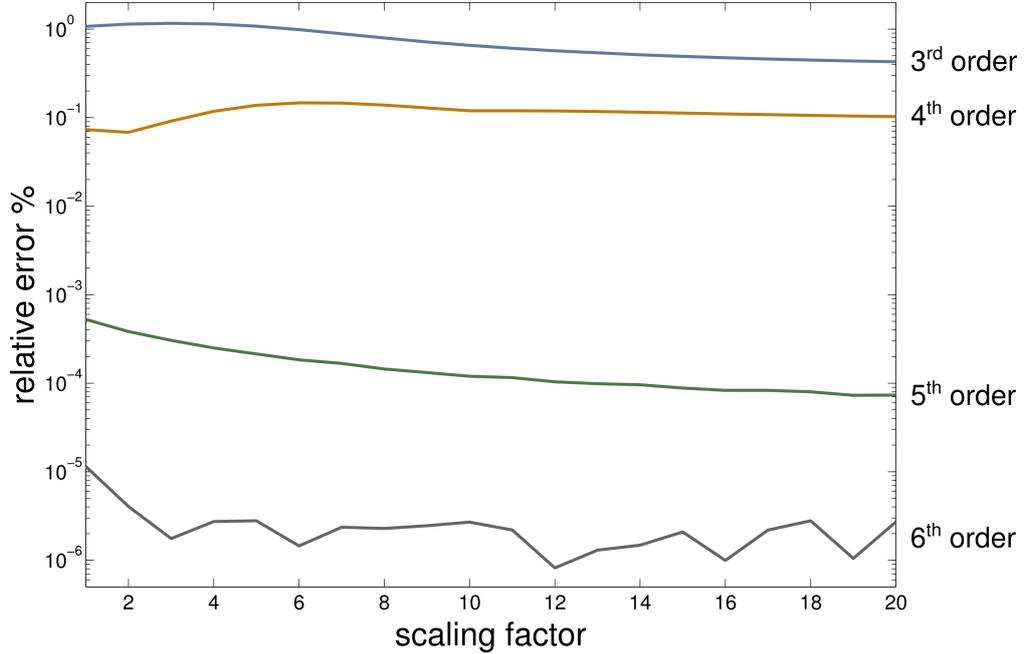
Figure 3.11: Relative error for different basis truncation levels of a spin system containing six nuclei and one electron in the pyramid configuration. The truncation level of the spin correlation order is indicated to the right of the graph.

Additionally ^{13}C nuclei have been tested in the random configurations. Due to their lower gyromagnetic ratio the hyperfine interaction constants are four times smaller and the nuclear dipole interaction even 16 times smaller than in the case of the protons. Hence larger scaling parameters were used in order to obtain the same range of χ-values as for the case of protons. Also here the errors remain smaller than ξ in all cases.

Revisiting the configuration used in figure 3.4 , section 3.4.2, as a showcase to demonstrate the accuracy of the averaged Hamiltonian, the deviation of the polarisation build up curves calculated with fourth order basis truncation from the curves obtained using the full state space are shown in figure 3.12. The left column shows the evolution of the spin system for three different sets of input parameters, the middle column again the error incurred from using the averaged Hamiltonian only, and in the right hand column the residual for additionally using the fourth order basis truncation is displayed. For row **c**, where the hyperfine interaction constants have been doubled, $m_*(\chi = 0.12) = 4.4$, and the largest error for the basis truncation remains less than 10^{-2}.
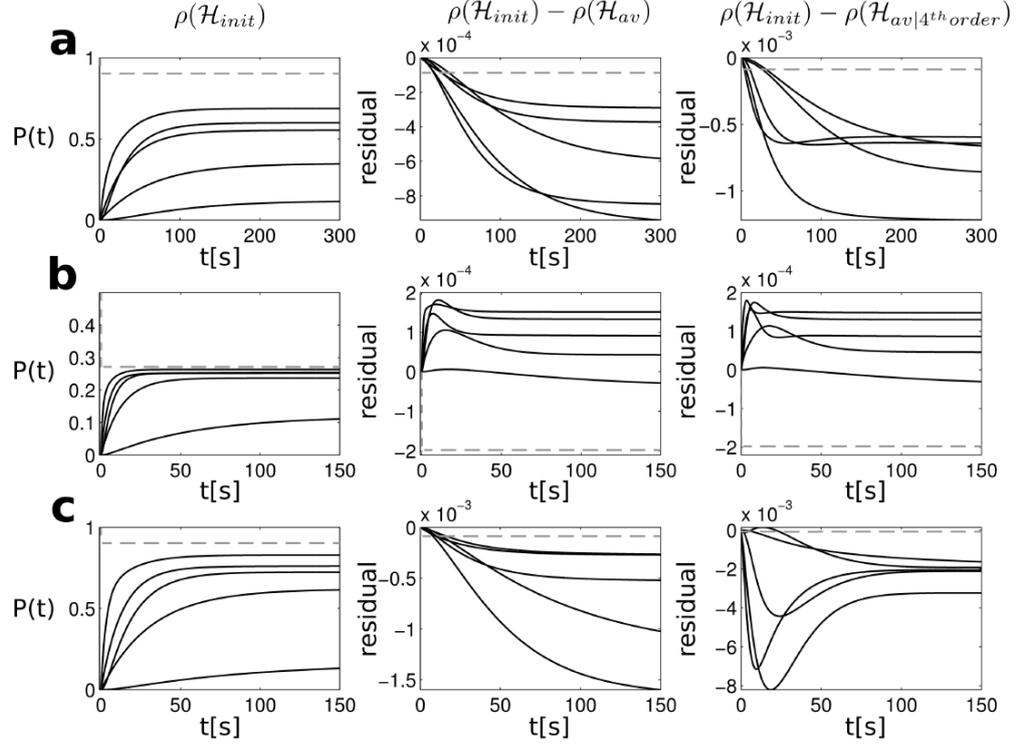
Figure 3.12: Simulation results for the pyramid configuration first mentioned in section 3.4.2 and displayed in appendix C. The nuclear build up curves are depicted in black, the electron is the dashed grey line. The constant relaxation operator was used with the parameters: $r_{1n} = 0.01 \frac{rad}{s}$, $r_{2n} = 10 \frac{rad}{s}$, $r_{1e} = 10^3 \frac{rad}{s}$, $r_{2e} = 10^6 \frac{rad}{s}$. Left column: full basis, full Hamiltonian. Middle column: full basis, averaged Hamiltonian. Right hand column: fourth order basis truncation, averaged Hamiltonian. In row **a**: ω_1=1.5 MHz and $\chi = 0.23$. In row **b**: the microwave power has been changed to ω_1=7.5 MHz and remains $\chi = 0.23$. In row **c**: the hyperfine interaction constants have been doubled, $\chi = 0.12$.

Removing additional states

It was mentioned that in some cases it is possible to remove more states, additionally to the ones removed by truncation of the basis at spin correlation order m_*, and still obtain a good approximation of the evolution of the spin system. In order to investigate this, random configurations of five ^{13}C nuclei and one electron with basis truncation level 3 were simulated. For the chosen configurations $\chi = 2$, justifying the basis truncation at the 3 spin correlation order. The averaged Hamiltonian was used, which resulted in a density operator containing 192 basis operators to describe the spin system. The time evolution of each state was calculated, then a threshold is applied to cut out states with a maximum amplitude of A_{th}. The same configuration was then simulated again and the relative error with respect to the simulation obtained using the initial state space was calculated. This was repeated and on each repetition the threshold was decreased, effectively cutting out more and more states until a relative error of $\sim 100\%$ was reached.

It was observed that for some configurations the error increases immediately over the 5% tolerance, whereas for others the error stays largely the same until it increases with one sudden jump to $\sim 100\%$. This indicates that for some configurations, corresponding to certain sets of interaction constants, it is possible to remove a large number of additional states without affecting the quality of the simulation significantly. Figures 3.13 shows two representative simulations for either case. On the left one can see that the error increases very quickly over the 5% error tolerance, whereas on the left the error remains less than 5% with only 50 out of the initial 192 states, or if one compares this to the full state space 50 out of $4^6 = 4096$ states. In order to demonstrate that the number of basis operators included in the simulation did not decrease rapidly from one threshold point to another, which could result in a large number of states being discarded at once, and hence a large error jump, the number of states left in the simulation

are plotted in blue, with their y axis on the right of each figure.

This clearly demonstrates the potential for additional compression, if one was able to identify a-priori the redundant states. So far it has not been possible to find a good prediction as to which states fall into this class.

SPINACH has a built in threshold setting called 'zero-track elimination' which evolves the spin system for a few very small time steps and then cuts out all states that have not been populated by more than a certain threshold within this time. This setting was always disabled during simulations for basis truncation tests and testing the average Hamiltonian as no analytical conditions for safe thresholding have been found , but clearly this feature has a great potential to reduce the dimension of the density state vector even further if such a condition was obtained.
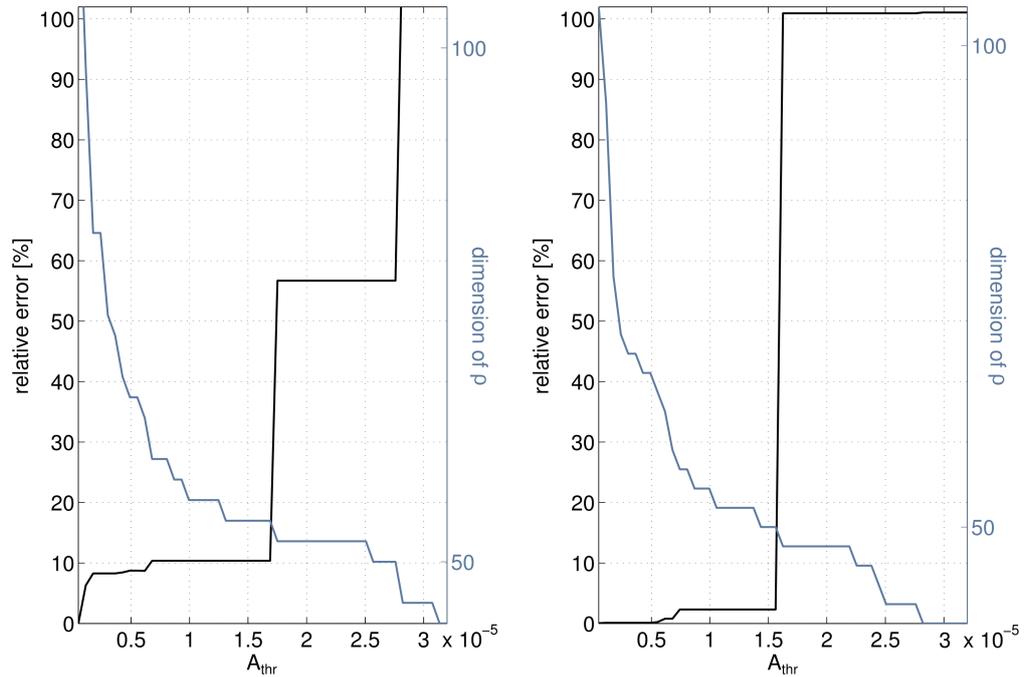
Figure 3.13: Size of the matrix describing the spin evolution (blue) and largest relative error of the simulation(black).

Basis truncation conclusions

The method of restricting the size of the propagator by reducing the state space to basis operators containing product states of up to a user defined order results in polynomial scaling, instead of the original exponential scaling. If third order truncation is possible, the Liouville presentation of a spin system scales more favourably than the Hilbert space description from 18 spin onwards, as could be seen in figure 3.5. It was found that for most realistic nuclear and electronic interaction parameters the basis could be truncated safely to fourth order for ^{1}H spins and to third order for ^{13}C nuclei (see figure 3.14). The largest number of nuclei that can then be simulated, in conjunction with using the averaged Hamiltonian, is 13 for protons and 26 for ^{13}C nuclei. The duration of simulating the behaviour of a spin systems close to the upper limit can be up to 58 hours, so although it is possible to access Liouville space simulation results for these spin systems it is tedious to probe the outcome for many different input parameters. Staying slightly under the maximum limit can already drastically reduce the simulation time, as it scales exponentially with the propagator size (see figure 3.1). Despite the basis truncation theory being defined for the multi spin limit, testing of the basis truncation condition has shown to still provide accurate prediction of the minimum truncation level for smaller spin systems. The considerations that lead to condition (3.5.9) are not just restricted to DNP simulations. The same treatment can also be applied for any spin system, whilst care has to be taken about the relaxation mechanisms involved [66].

The presented methods of truncating the basis in conjunction with the averaging the Hamiltonian have increased the number of spins that could thus far be simulated in the Liouville space. Whilst insight into the behaviour of nuclei around the electron can be gained, for polarisation of samples with realistic spin concentrations the numbers that can be achieved are not sufficient.
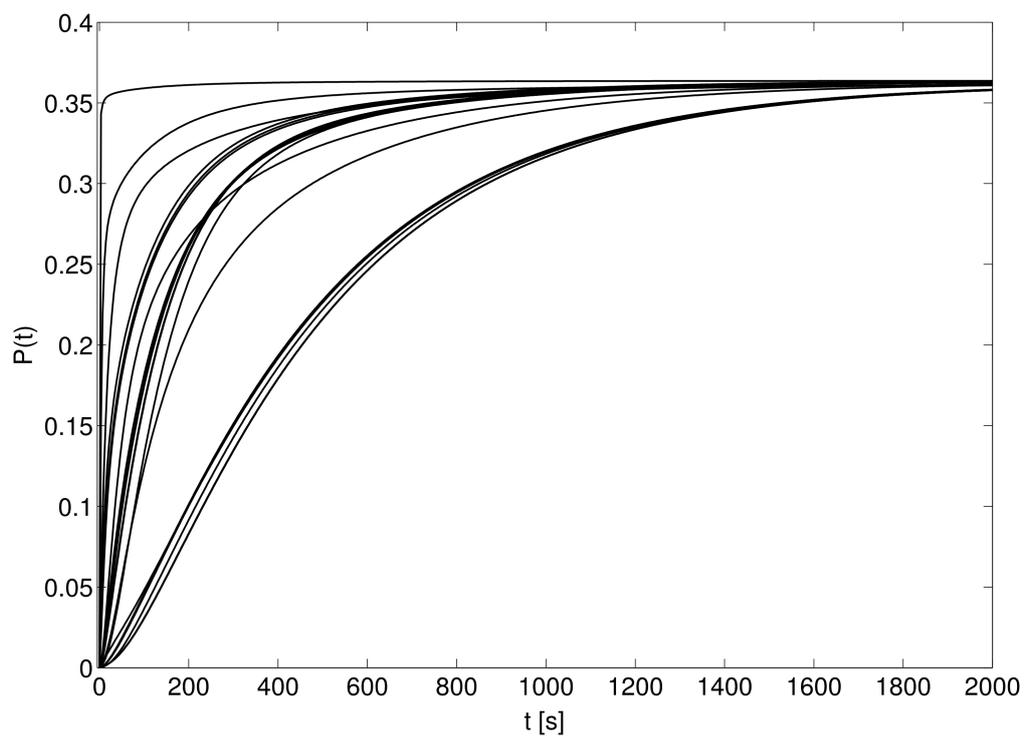
Figure 3.14: Build up curves of 25 ^{13}C nuclei obtained with the averaged Hamiltonian and basis truncation order 3. A scaled relaxation operator was used with $r_{2e} = 10^6 \frac{\text{rad}}{\text{s}}$, $r_{2e} = 10^6 \frac{\text{rad}}{\text{s}}$.

3.5.3 'Multi-exponentiality' of the polarisation build-up curves

Using the averaged Hamiltonian in conjunction with the lowest possible basis truncation order of 3 makes it possible to carry out simulations with up to 26 spins using an 8 GB RAM memory card. This is an improvement on the previous limit of seven spins using the full system size in the Liouville space, or the maximum of ten spins that are achievable when the Hilbert space method presented in [55] and [56] is used. Nonetheless, a simulation reflecting realistic sample conditions would have to include far more spins, which is only possible if the dimension of the matrices involved in the calculations is further reduced.

In order to test whether it is possible to describe the build-up curves of the nuclei with a mono-exponential function of the form $P_n(t) = P_0(1 - \exp(t\tau_b^{-1}))$, where an a priori knowledge of P_0 and τ_b has yet to be obtained, nuclear polarisation build-up curves of spin systems have been fitted with the aforementioned function and the error of the fit was analysed. For this, three regions were defined, a core region, a bulk region and a mix of a core and bulk region following the definition in [55] and [56]: Bulk nuclei are defined as the nuclei whose dipole interaction is five times larger than the difference in their hyperfine interaction constants, so

$$5|d_{ij}| > \Delta A_{ij} = \frac{1}{2}\left|A_{k,i} - A_{k,j} \pm \frac{|B_{+,i}|^2 - |B_{+,j}|^2}{4\omega_I}\right|. \qquad (3.5.11)$$

As is acknowledged in the mentioned publications, the scaling factor before the nuclear dipole dipole interaction is somewhat arbitrarily defined but has been shown to ensure true 'bulk behaviour' of the spins in the simulation, meaning that excluding dipole interaction between the nuclei results in very different polarisation build-up curves for each nucleus. This indicates that the distribution of polarisation via spin diffusion plays a big role in this region, as would be expected. The transition from full bulk to full core nuclei is not clearly defined: Nuclei that do not fall into the bulk classification of 3.5.11 do not necessarily behave strictly as core nuclei, some can still have significantly different build-up

curves when the nuclear dipole interaction is excluded.

In order to match the pure bulk condition 3.5.11, the nuclei in the examples chosen have been far removed from the electron (minimum distance 30Å) to reduce the strength of the hyperfine coupling and put close together for strong nuclear dipole interaction. For the simulations of a pure core, the nuclei were positioned in such a way that the hyperfine interaction quenched the nuclear dipolar interaction, so only a small difference in the build-up curves was found upon exclusion of nuclear dipolar interaction. For the mix region pure core and bulk nuclei, as well as intermediate nuclei where included. Intermediate nuclei are nuclei that fall by definition 3.5.11 into the class of core nuclei but still show changes in the build-up curve when dipole interaction is excluded.

The constant relaxation operator was used, with the relaxation rates chosen to be: $r_{1e} = 10^3$, $r_{2e} = 10^6$, $r_{1n} = 10^{-2}$ and $r_{2n} = 10^2 \frac{\text{rad}}{\text{s}}$. The largest relative and absolute error over the entire simulation were calculated for each fit of a build-up curve, as well as the steady state relative and absolute error. The errors were also calculated for the simulation of the same configuration with all nuclear dipole interaction set to zero. Three randomly generated configurations with five nuclei and one electron for each region were carried out.

It was found that steady state error in the fit remained small for all three scenarios. The largest absolute steady state error of all three configurations was found to be $1.6 \cdot 10^{-3}$, and the largest relative error 0.2% ,when dipolar interaction was included. When dipolar interaction was removed this reduced to a maximal absolute error of $8.3 \cdot 10^{-4}$ and relative error of 0.05%.

For the pure bulk region the largest relative error of all fitted build-up curves was 2.8% and the largest absolute error was $5 \cdot 10^{-6}$ with dipolar interaction included and $5 \cdot 10^{-8}$ when the dipolar interaction was neglected. This error is small, so a mono-exponential description of the build-up curves is justified, provided one can find a priori expressions for P_0 and τ_b. The exclusion of the dipolar

interaction yields very different steady state polarisations but the difference in the build-up time constants is less than 0.1%.

For the pure core region the errors also remain acceptably small, for example the largest relative error was found to be 4.5% and the largest absolute error 0.02. Obviously the errors remain the same when dipolar interaction is excluded.

When a configuration is chosen, where some nuclei fit the bulk description 3.5.11, some can be considered to be core nuclei and others are somewhere in between, the errors become considerably large. The average relative error over all build-up curves of all three configurations is 19%, with the largest error found being 87%. The largest absolute error has been found to be 0.14, with the average being 0.05. This reduces significantly when dipolar interaction is neglected: the largest relative error reduces to 0.03% and the largest absolute error to $0.7 \cdot 10^{-3}$.

From the small number of configurations tested, the conclusion is that a mono-exponential description of the build-up curve seems justified for a sample containing purely bulk or purely core nuclei. When a sample contains a mixture of both, or nuclei that do not belong strictly to either category, the deviation from a mono-exponential build-up curve can become relatively large, mostly in the initial stages of the simulation as can be seen in figure 3.15.

The error of a mono-exponential fit has been shown to reduce significantly for the core - bulk mix region when dipolar interaction is neglected. One reason for the deviation from a mono-exponential build-up curve might be explained from the following observations, that can be made from Table 3.3 and figure 3.16:

- For the pure core configurations the build-up time constants are quite different for each nucleus, and the dipolar interaction is quenched.

- For the pure bulk configurations the build-up time constants are very similar, and the dipolar interaction has a large effect on the final polarisation.
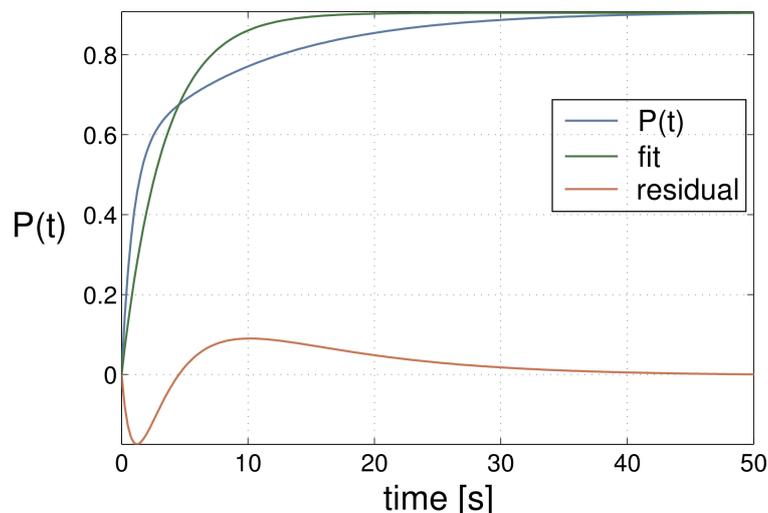
Figure 3.15: Example build-up curve for a nucleus from a core-bulk mix (blue line) that does not behave strictly mono-exponentially. The green line shows the mono-exponential best fit, the orange line the difference between the fit and the build-up curve. As one can see, the largest error occurs in the initial build-up stage.

- The bulk-core mix configurations the build-up time constants are different and the dipolar interaction has an effect on the build-up curves and the final polarisation.

From this one can conclude that probably the multi-exponentiality stems from the fact that nuclei, whose dipolar interaction plays a non-negligible role in the build-up curves, are affected by the faster or slower build-up time constants of their strongly coupled neighbouring nuclei. In the pure core sample the build-up time constants are different for each nucleus but the dipolar interaction is quenched so the nuclei do not experience each others different time constants.

In conclusion, for the examples containing only bulk or only core nuclei, the nuclear polarisation build-up can be described very well by a mono-exponential function. The polarisation rates in the bulk are close to the nuclear longitudinal relaxation time. For samples, where the type of region is not clearly defined, and

90

Table 3.3: build-up time constants of example configurations for each region. The time constants are given for simulations including and neglecting the nuclear dipolar interaction and their ratios are stated.

Region		build-up time constants τ_b^{-1} in $\frac{rad}{s}$				
Bulk	including dipole interaction	0.0106	0.0106	0.0106	0.0106	0.0106
	excluding dipole interaction	0.0109	0.0106	0.0105	0.0108	0.0103
	ratio	0.9716	1.0039	1.0160	0.9835	1.0271
Core	including dipole interaction	0.270	0.382	1.761	4.659	10.270
	excluding dipole dipole	0.262	0.380	1.757	4.612	10.324
	ratio	1.031	1.005	1.002	1.010	0.995
Core-Bulk Mix	including dipole interaction	0.088	0.213	0.088	2.923	0.213
	excluding dipole interaction	0.015	0.059	0.0103	3.303	0.400
	ratio	5.781	3.590	8.507	0.885	0.532
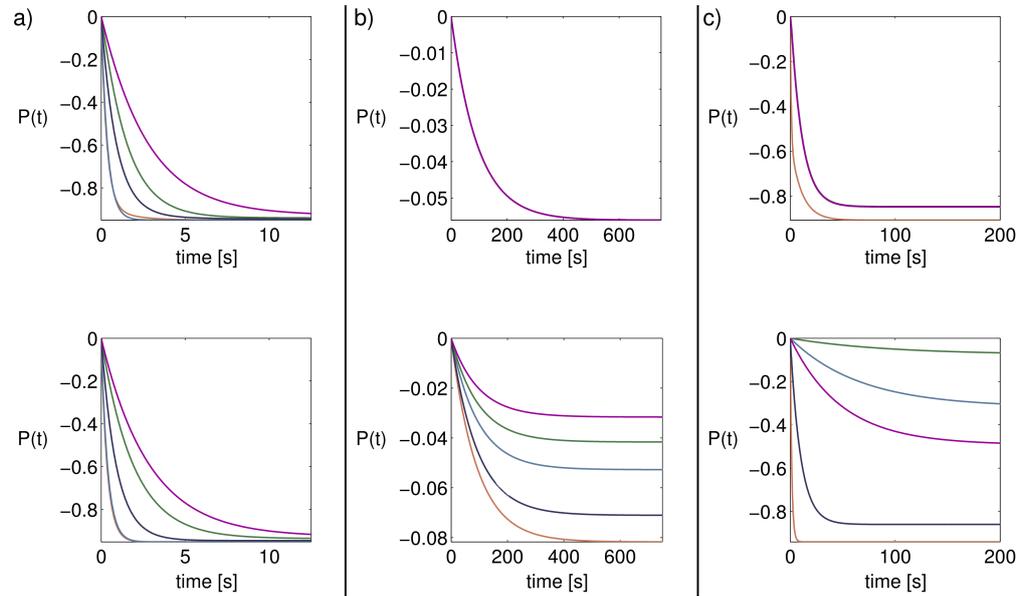
Figure 3.16: Evolution of the nulear polarisations for an example configuration for each region: Pure core (a), pure bulk (b), and a mixture of core and bulk nuclei (c). The build-up curves are shown with (top row) and without (lower row) inclusion of nuclear dipole interaction.

one can assume that in a realistic sample the boundaries between the core and bulk region are fuzzy, a mono-exponential function does not always describe the build-up curves well, and in certain cases the error can become quite large. One can reduce this error by excluding the nuclear dipole interaction but this can change the final polarisation and build-up rates substantially, as can be seen from figure 3.16 b) and c). Since the sample of configurations that were tested is small, it may be possible that the large errors for the core-bulk mix could average out when a larger number of geometries is considered, as well when a large number of spins is included in the simulation. Nonetheless, if one wants to obtain very accurate results a multi-exponential approach to the simulation is needed.

Such an approach will be introduced in section 3.7. Before that, an excursion into the parameters involved in the solid effect will be made in the next section.

3.6 Solid Effect Observations

The parameter space involved in determining the final DNP enhancement and build-up rates is very large and many factors interplay in the DNP mechanism, which is the main problem that prevents a rigorous quantitative description of the process to date. In order to shine a small light on a few of the important factors determining the final enhancement and characteristic build-up time in solid effect DNP a few observations from the simulations will be discussed here. A similar and more in depth discussion can be found in [56].

3.6.1 Off resonance irradiation and microwave strength

Polarisation build-up by irradiation on the zero and double quantum transitions does not strictly occur only at the offset frequencies $\omega_S \pm \omega_I$. Irradiating slightly off-resonant from the DNP frequency $\omega_S \pm \omega_I$ also results in some polarisation build-up. In [56] it has been shown that one can view the double or zero quantum transition as a fictitious spin $\frac{1}{2}$, so analogously to the off resonance behaviour for a single quantum transition in a two level system with the steady state solution to the Bloch equation for M_z:

$$M_z = M_0 \frac{1 + (\Delta\omega T_2)^2}{1 + (\Delta\omega T_2)^2 + \gamma^2 B_1^2 T_1 T_2}, \tag{3.6.1}$$

where M_0 is the initial magnetisation of the spin, T_1 and T_2 its longitudinal and transversal relaxation times, $\Delta\omega$ the offset term and B_1 the amplitude of the perturbing field. The line shape is then a Lorentzian of line width T_2^{-1} or, when saturation is included [3]:

$$T_2'^{-1} = T_2^{-1} \left(1 + \gamma^2 B_1^2 T_1 T_2 \right)^{\frac{1}{2}}. \tag{3.6.2}$$

In the case of the double or zero quantum transitions, γB_1 has to be replaced by the effective microwave field $s\omega_1$ with $s \simeq \frac{|B_+|}{2\omega_I}$, which has been obtained from diagonalisation of the two spin solid effect Hamiltonian [56]. The relaxation

time constants have to be replaced by $T_{1,ZQ/DQ}$ and $T_{2,ZQ/DQ}$, with which the double and zero quantum states decay . In the relaxation operator defined in 3.2 and used in this work such terms are not explicitly defined but still a broadened line in the frequency dependency of the steady state polarisation is present (see figure 3.17). This can be explained by the following considerations: The effect of $T_{1,ZQ/DQ}$ is relaxation of both the electron and nuclear spin. This can be approximated by the sum of the relaxation times T_{1n} and T_{1e} and, as the electronic relaxation time is usually much smaller than the nuclear, $T_{1,ZQ/DQ}$ can be replaced by T_{1n}. It was observed that replacing $T_{2,ZQ/DQ}^{-1}$ with T_{2e}^{-1}, so the dominant transversal relaxation time, results in a relatively good prediction of the line widths of the final polarisations using equation (3.6.2), as can be seen in Table 3.4. The fact that T_{2e} can be used makes sense intuitively, as it determines the electronic line width and the final DNP enhancement follows the EPR spectrum closely.

Table 3.4: Comparison of line widths obtained from the simulation (left table) and with equation (3.6.2) (right table). All line widths are given in units of MHz, the relaxation rates are in $\frac{rad}{s}$. The simulation parameters are: |B|=0.17 MHz, $r_{1n} = 3 \cdot 10^{-3} \frac{rad}{s}$, $r_{1e} = 10^3 \frac{rad}{s}$, $r_{2n} = 30 \frac{rad}{s}$. r_{2e} in the tables is given in units of $\frac{rad}{s}$

		$\omega_1/(2\pi)/10^6$					$\omega_1/(2\pi)/10^6$		
		1	0.5	0.1			1	0.5	0.1
	10^6	2.40	1.24	0.4		10^6	2.40	1.24	0.29
r_{2e}	$5 \cdot 10^5$	1.71	0.86	0.25	r_{2e}	$5 \cdot 10^5$	1.74	0.87	0.20
	$2.5 \cdot 10^5$	1.22	0.5	0.15		$2.5 \cdot 10^5$	1.21	0.61	0.13

Using the scaled relaxation operator the offset sweep has been obtained for several positions of the nucleus, with the electron sitting at the origin of the coordi-

nate system. It can be seen from figure 3.17 that the line broadening decreases for decreasing r_{2e} and increases for larger microwave power ω_1.
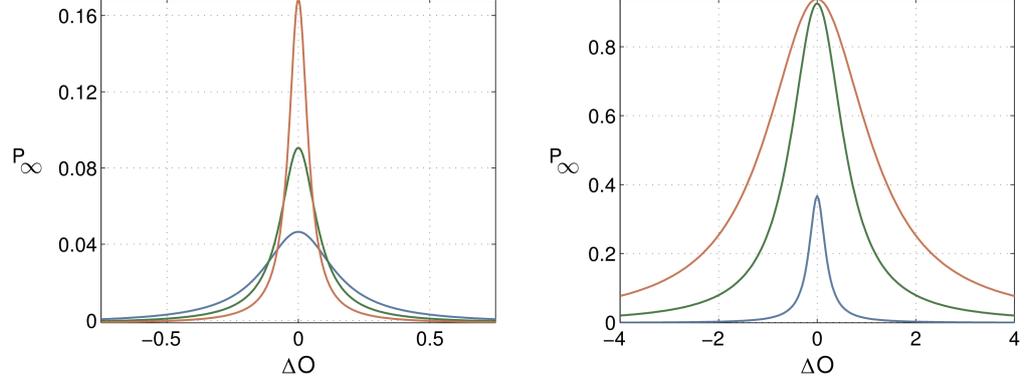
Figure 3.17: Offset behaviour of the steady state polarisation of the nucleus P_∞ for different electronic transversal relaxation rates T_{2e}^{-1} (left) and microwave powers ω_1(right). The parameters that both figures have in common: $|B| = 0.17\,\text{MHz}$, $r_{1n} = 3 \cdot 10^{-3}\frac{\text{rad}}{\text{s}}$, $r_{1e} = 10^3 \frac{\text{rad}}{\text{s}}$, $r_{1n} = 30\frac{\text{rad}}{\text{s}}$. Parameters for left hand figure: ω_1=30 kHz; blue line: $r_{2e} = 10^6 \frac{\text{rad}}{\text{s}}$; green line: $r_{2e} = 0.5 \cdot 10^6 \frac{\text{rad}}{\text{s}}$; orange line: $r_{2e} = 0.25 \cdot 10^6 \frac{\text{rad}}{\text{s}}$. Parameters for the right hand figure: $r_{2e} = 10^6 \frac{\text{rad}}{\text{s}}$; blue line: ω_1=0.1 MHz; green line: ω_1=0.5 MHz; orange line: ω_1=1 MHz. The offset ΔO is given in MHz

If the distance r between the electron and nucleus is kept constant and the angle θ between the z axis and the electron-nuclear connecting axis is varied, one always obtains the same frequency profile. This is consistent with the scaled relaxation operator r_{1n} is being scaled by $|B_+|^2$, and hence in equation (3.6.2) the product of effective microwave amplitude squared times the inverse of r_{1n} remains constant. If a relaxation operator is used, in which the nuclear relaxation rates are not scaled by the hyperfine term $|B|$, the line shapes (and final polarisations) do change but still obey equation 3.6.2.

3.6.2 Frequency sweep

The A_k terms of the hyperfine interaction, as well as to a small extent the B_k terms, cause a shift in the energy levels. For the case of a single nucleus coupled to an electron this shift is in the same direction for both electronic levels. When additional nuclei are added the DNP frequency for the nucleus i is modified by the A_k terms of the other nuclei like [69]:

$$\omega_{DNP}(i) = \omega_S + \omega_I + \sum_{k \neq i} \pm A_{zk}. \qquad (3.6.3)$$

Equation (3.6.3) is valid for the double quantum transition. The zero quantum transition can be obtained by inverting the sign before ω_I. According to equation (3.6.3) a nucleus with a stronger hyperfine constant will split the DNP transition frequency of a nucleus with a weak hyperfine constant to a greater extent than the other way around. Figure 3.18 shows an example for a system with three nuclei coupled to an electron. In the main figure, the black line shows the electron saturation for off resonance irradiation, whereas the light blue line shows the average of all final polarisations of the nuclei. The inset b) shows the final polarisation of the nuclei for different offset frequencies from $\omega_S \pm \omega_I$. The positions of the nuclei are shown in inset a) and the color of the plot corresponds to the color of the spins in the coordinate system. One can see that the spin depicted in dark blue,which has the strongest secular hyperfine interaction constant, experiences the smallest splitting, whilst the spin depicted in orange with the weakest A_k, is split into a quartet with frequencies corresponding to the other hyperfine constants. In a realistic sample a large spread of hyperfine interaction constants will result in a smooth distribution of DNP resonances, rather than a band structure.
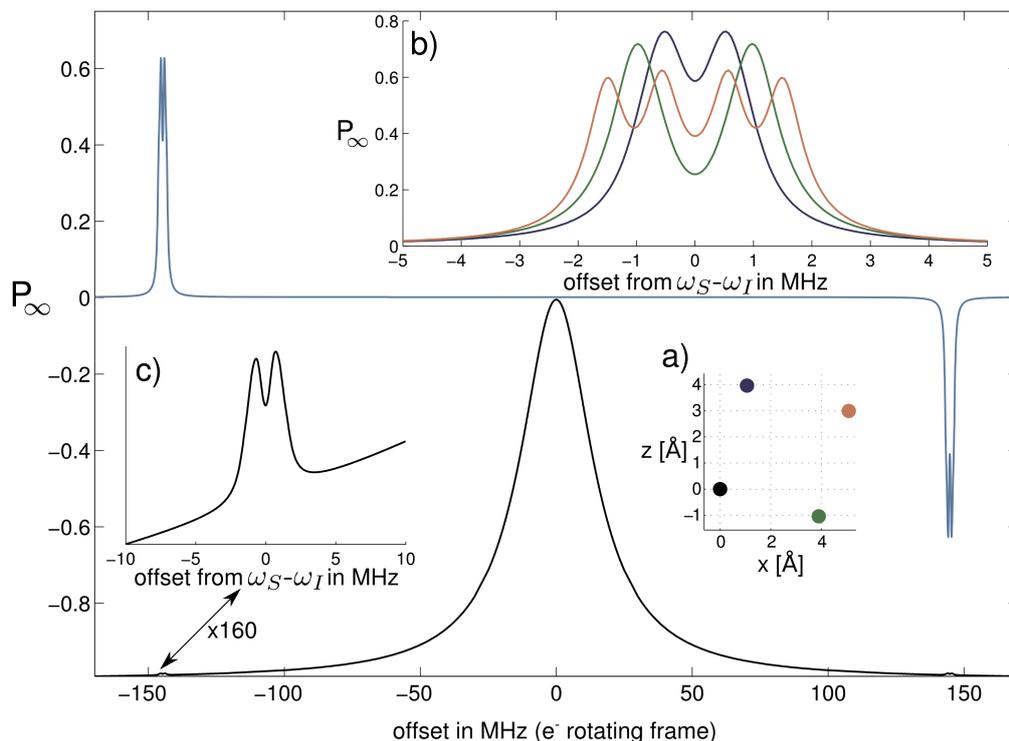
Figure 3.18: Offset dependency of final polarisation for a spin system containing 3 nuclei and one electron. The average final polarisation of the nuclei is depicted in light blue, whereas the electron saturation is shown in black. Figure inset a) shows the geometry of the nuclei with the electron at the origin, inset b) shows the offset dependency of the nuclei and inset c) shows a 160 times zoom into the electron DQ or ZQ saturation. Interaction constants A_k of the spins: dark blue: 2.5 MHz , green: -1.2 MHz, orange: -0.1 MHz

3.6.3 Final Polarisation and build-up rates

The dependency of the final polarisation and rate with which the nuclear polarisation builds up on the microwave power and the ratio of $\frac{|B_+|}{r_{1n}}$ have been checked for a simple two spin system involving one electron and a proton. For this, the evolution of the system has been recorded for several positions of the proton, keeping the electron at the origin of the coordinate system. The inter-spin distance is kept the same, but the angle θ with the z axis is varied, resulting in

97

different interaction constants A and $B_\pm$. The angle was changed between 0.1π and 0.4π in order to avoid the infinitely long build-up times that occur at the positions where $|B_\pm| = 0$. The nuclear polarisation build-up rate constant τ_b^{-1} was obtained by fitting an exponential to the polarisation curve. The resulting nuclear steady state polarisations P_∞ for different angles θ and microwave powers ω_1 can be found in figure 3.19a). As was indicated in the previous section the saturation of the double and zero quantum transition can be described by

$$M_{z,DQ/ZQ} = M_0 - M_z = M_0 \left(1 - \frac{1 + (\Delta\omega T_{2e})^2}{1 + (\Delta\omega T_{2e})^2 + s^2\omega_1^2 T_{1n}T_{2e}} \right), \qquad (3.6.4)$$

which on resonance reduces to

$$M_{z,DQ/ZQ} = M_0 \left(1 - \frac{1}{1 + s^2\omega_1^2 T_{1n}T_{2e}} \right).$$

If for M_0 the electronic steady state magnetisation $M_{z,e}$ at the zero or double quantum frequency is used, then the final polarisation of the nuclei is

$$P_\infty = M_{z,e} \left(1 - \frac{1}{1 + s^2\omega_1^2 T_{1n}T_{2e}} \right). \qquad (3.6.5)$$

as can be seen in figure 3.19b), where the dashed grey lines follow equation (3.6.5). When the microwave irradiation power becomes larger the electronic longitudinal magnetisation M_{ze} decreases, which reduces the population difference on the electrons, and hence the final polarisation of the nuclei.

When the angle θ is changed, this modifies the effective microwave field $s\omega_1$, which in turn shifts the saturation of the double and zero quantum transition, as can also be seen in figure 3.19b). This effect is removed when the same simulations are carried out using a relaxation operator, where the nuclear relaxation rates are scaled by the hyperfine interaction. Then the final polarisation remains constant for the different values of θ (see also figure 3.19c)). The same effect can also be obtained by changing the nuclear longitudinal relaxation rate.

The build-up rate constants τ_b^{-1} for different angles θ and microwave powers ω_1 are shown in figure 3.20. For low ω_1 the build-up rate equals the nuclear
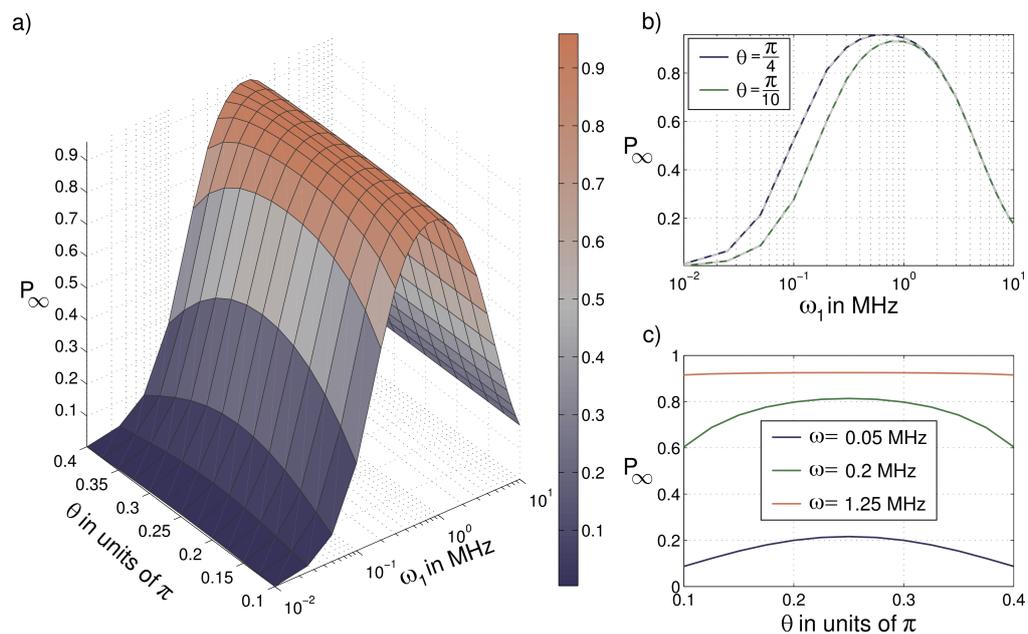
Figure 3.19: Dependence of the final polarisation on the microwave power ω_1 and the azimuthal angle θ (a). The inset b) shows the final Polarisation for two fixed angles, along with the predicted P_∞ from equation 3.6.5 in grey dashed lines. In c) one can see the angle dependency of the final nuclear polarisation for three fixed microwave powers.
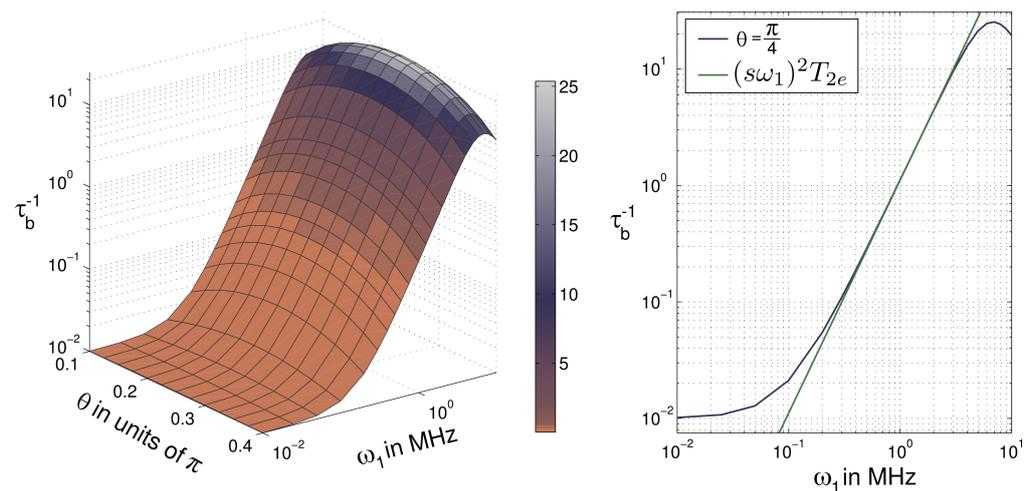
Figure 3.20: Dependence of the build-up rate constant τ_b^{-1} on the microwave power ω_1 and angle θ. On the left the rate constants vs the microwave for $\tau = \frac{\pi}{4}$ is shown along with the build-up rate derived in [55].

longitudinal r_{1n}. When ω_1 is larger than r_{1n} the rate constant starts to follow $(s\omega_1)^2 T_{2e}$, which has been derived in [55] from the Bloch equations. This does not hold any more when the microwave power becomes too large, as can be seen in figure 3.20 on the right.

Equation 3.6.4 can also be used to predict the off resonance behaviour of the final polarisation. To demonstrate this the angle θ of the nucleus has been set to the magic angle and the microwave power to 0.5 MHz. Figure 3.21 confirms indeed that the final polarisation follows equation 3.6.4. The dependency of the build-up rate τ_b^{-1} on the offset was also tested. This was found to follow the expression in [55] for the off resonant case $\frac{(s\omega_1)^2 T_{2e}}{1+(\Delta\omega T_{2e})^2}$ very closely , although it was found that in order to obtain a very good match the nuclear relaxation rate r_{1n} had to be added on to this expression. This demonstrates that the polarisation process is a combination of coherent transfer effects and incoherent relaxation effects.

3.6.4   Bridge nucleus

The question arose whether the polarisation build-up would benefit from selectively labelling the Trityl radical with a 'bridge nucleus' inside the 12Å radius for more effective polarisation transfer from the electron to the surrounding nuclei.

Using simulations with the averaged Hamiltonian and the basis truncation strategy this idea was tested. An electron was placed in the center of the coordinate system and four nuclei were placed in the first octant, with a minimum distance of $r_{min} =12$Å from the electron, and a maximum distance of $r_{max} = 24$Å, representing a sample with 15mM electron concentration and 1M nuclear concentration. Then an additional nucleus was placed at $r = r_b$, where r_b ranged from 5 to 11Å. Two angles were tested, $\theta_b = \frac{\pi}{4}$, where the hyperfine interaction constant B_k is maximal, and $\theta_b = \theta_{MA}$, where the hyperfine splitting is minimal.
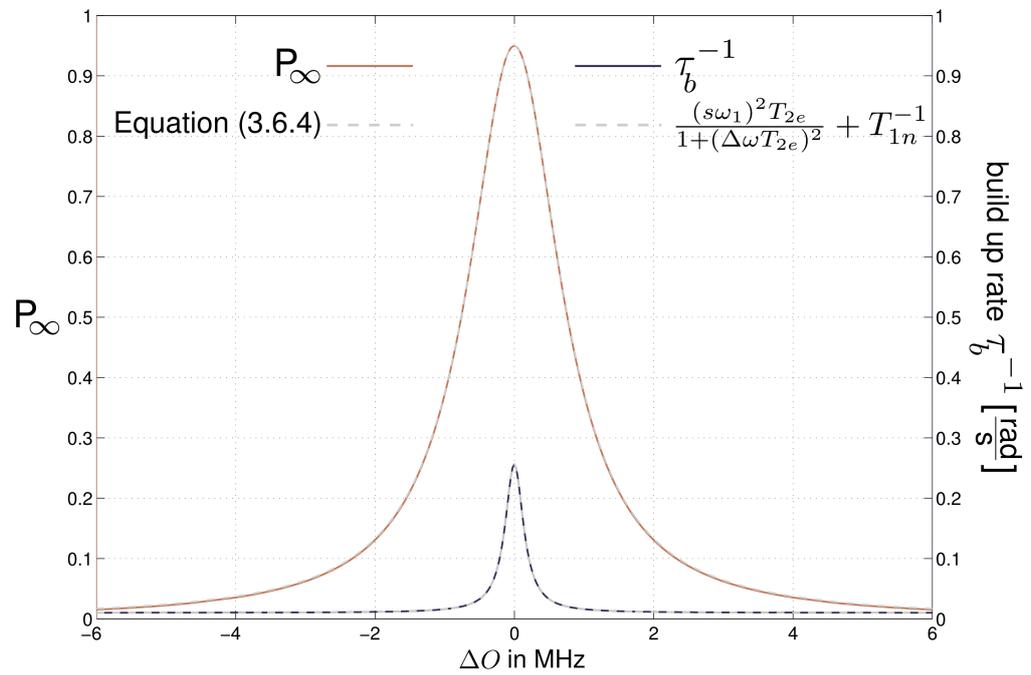
Figure 3.21: Dependence of the build-up rate constant τ_b^{-1} and the final polarisation on the offset. The left y axis corresponds to the final polarisation, the right hand y-axis to the polarisation build-up rates.

The angle ϕ was set to $\frac{\pi}{4}$.

Two hundred different random configurations for the nuclei outside the 12Å threshold were recorded and the average build-up curve of these nuclei was calculated. In order to check convergence, the average build-up of the nuclei was compared to the build-up of the first 150 random configurations and the difference was found to be less than 1.4% for all r_b, which was deemed sufficient. The smallest $\chi = \frac{r_0}{c_0}$ for the bridge nucleus at 5,6 and 7Å was 0.05, 0.08 and 0.14 respectively. For these configurations the full basis was used. For $r_b = 8$Å the smallest χ was 0.21, justifying 4$^{\text{th}}$ order basis truncation. For all larger r_b and the configuration without a bridge nucleus 3$^{\text{rd}}$ order truncation was used as $\chi \leq 0.29$. The simulations were carried out using a constant and a scaled relaxation operator.

It turned out that for the chosen geometry the optimum final polarisation and build-up time was for the position of the bridge nucleus at the 12Å boundary, so no spin diffusion assistance was provided by the bridge nucleus. The hyperfine interaction of the outside nuclei was too large and so spin diffusion is quenched. If one increases the distance of the outside nuclei to r_{min}=24Å, and shifts the bridge nucleus between 12 and 24Å one sees an optimum position for the bridge nucleus at around 12Å as can be seen in figure 3.22 for the constant relaxation operator and a bridge nucleus at the magic angle. This effect disappears if one sets the interactions between the core and bulk nuclei to zero, confirming that this is indeed a spin diffusion effect.

In figure 3.22 the polarisation build-up times are also displayed, which were obtained from a mono-exponential fit. The caveats associated with such a mono-exponential fit are described in section 3.5.3. In order to judge the accuracy of the build-up time constant displayed in the figure, also the largest residual of the fit is shown in orange. The bulk ('outside' nuclei) build-up rate is the largest at the around 12Å, which also coincides with the highest final polarisation. As
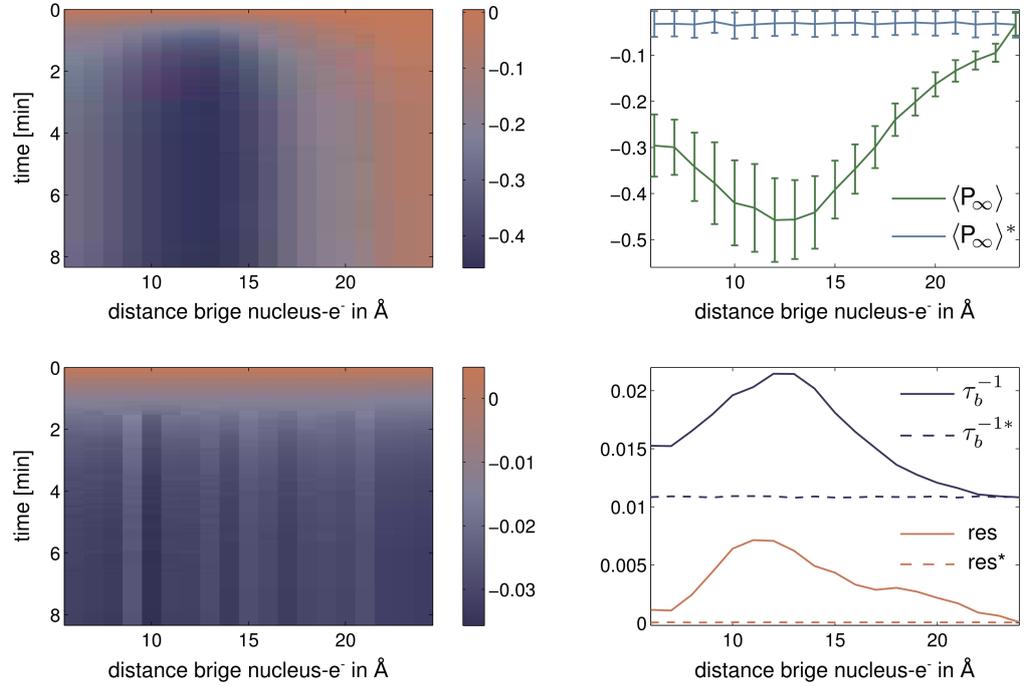
Figure 3.22: **Top left**: averaged build-up curves of the bulk with dipole interaction between bridge nucleus and bulk included. **Bottom left**: average build-up curves without the dipolar interaction between bridge nucleus and bulk. Note the different color bar scale. **Top right**: average final polarisation of the bulk nuclei, with and without including the dipolar interaction between the bridge nucleus and the bulk. The asterisk indicates the curve obtained without the dipole interaction between bridge nucleus and bulk. The error bars have been obtained from the standard deviation of all build-up curves for one particular bridge nucleus position. Optimum bulk polarisation at $r_{e-bridge} = 12\text{Å}$. **Bottom right**: build-up rate in $\frac{rad}{s}$, obtained from a mono-exponential fit with (blue full line) and without (blue dashed line) inclusion of dipole interaction between bridge and bulk nuclei. To indicate quality of the mono-exponential fit the residual of the fitting cure has been plotted in orange.

the bridge nucleus moves further away from the electron, its own build-up rate reduces and so the bulk also builds up polarisation slower. When the bridge nucleus moves closer to the electron, its own build-up rate and final polarisation increase but the dipolar interaction to the bulk decreases, hereby reducing the final polarisation and build-up rate of the bulk with respect to the optimum position of the bridge nucleus.

The residual of the mono-exponential fit is the largest for the optimal position of the bridge nucleus. In this position the polarisation of the bulk nuclei is dictated by a superposition of the build-up time constant for the core nucleus and the time constants of the bulk nuclei. In section 3.5.3 it was seen that the mono-exponential fit becomes worse if different time constants are present in the sample. As the bridge nucleus moves closer to the bulk, its own build-up rate becomes similar to that of the bulk nuclei so the error of the mono-exponential fit is smaller. For the positions of the bridge nucleus closer to the electron the interaction with the bulk nuclei becomes smaller, and so the polarisation build-up rate of the bulk is less influenced by the rate of the bridge nucleus. This also reduces the mono-exponential fitting error.

When the angle θ_b of the bridge nucleus is set to $\frac{\pi}{4}$, the optimum is shifted towards a higher electron-bridge nucleus distance as the secular part of the hyperfine interaction of the bridge nucleus causes a splitting in the DNP transition frequencies when it comes too close to the electron. In figure 3.23 one can see this effect. All parameters apart form the angle θ_b have been kept the same with respect to the data-set displayed in figure 3.22. The overall enhancement is decreased due to the splitting of the DNP transition frequencies and the maximum has been shifted to 16Å. The polarisation times are also slower and the fastest build-up rate coincides again with the highest final polarisation at 16Å. This confirms that the faster build-up is indeed a result of the transfer of polarisation of the bridge nucleus.
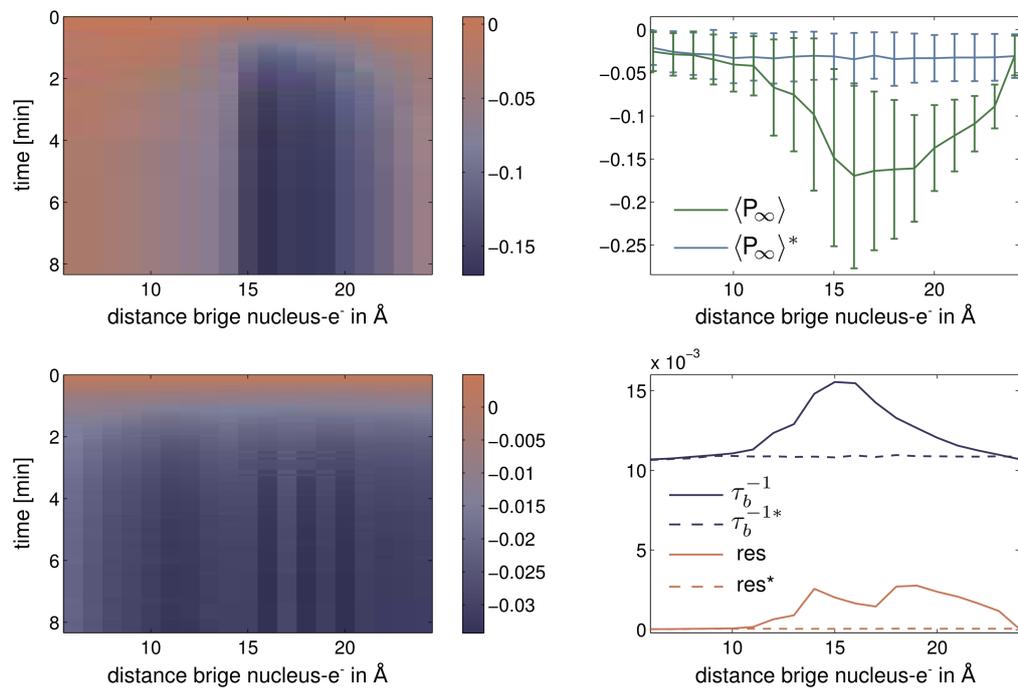
Figure 3.23: The description for this figure is identical to that of figure 3.22, only the angle θ_b is changed to $\frac{\pi}{4}$, making the secular part of the hyperfine interaction non-zero.

Repeating the same simulations with the scaled relaxation operator showed that on average all nuclei obtained the same final polarisation but there is an optimum in the build-up rate also at around 12Å (data not shown). This can be explained from the observations made in section 3.6 for a two spin system: The final polarisation of one spin coupled to an electron depends on the term $\left(\omega_1 \frac{|B_\pm|}{2\omega_I} \right)^2 T_{1n} T_{2e}$. As T_{1n} is scaled with $B_\pm$ the final polarisation does not depend on the angle θ of the nuclei. As spin diffusion does play a large role in the range between r=12Å and r=24Å the final polarisations equilibrate for the different distances of the nuclei to a single value across all the sample within these limits.

A radical with the mentioned outer dimensions does not exist but as a theoretical consideration of spin diffusion it is pleasing to know that the concept works.

3.7 Further reduction of the state space using a projection method

The development of a projection method for the description of nuclear polarisation build-up was developed by A. Karabanov. The author of this work has carried out the error analysis by comparing the projection method to simulations using SPINACH. The theory underlying the projection method will only be illustrated in the main points, some additional details can be found in appendix D. The full description will be presented in a future publication.

3.7.1 Principles of the projection method

The concept of dividing the Liouville space into subspaces and projecting the equation of motion into these different subspace was introduced in 3.5.1. The subspaces were defined based on spin correlation order, and the Hamiltonians containing a two spin correlation were the operators that could transfer magneti-

sation between the subspaces. The projection method is based on a similar idea but instead of dividing the Liouville space into several subspaces corresponding to spin correlation orders, it is split into just two. One subspace, $\mathfrak{L}_1$, is spanned by the basis operators containing the Zeeman spin orders $\{\hat{S}_z, \hat{I}_{1z}, \hat{I}_{2z}, \hat{I}_{1z}\hat{I}_{2z}...\}$, and the other, $\mathfrak{L}_2$, is spanned by all remaining basis operators and thus:

$$\mathfrak{L} = \mathfrak{L}_1 \oplus \mathfrak{L}_2$$

As it was found to produce accurate results, the averaged Hamiltonian from section 3.4.1 will be used in the equation of motion. This restricts the basis of the non-Zeeman order subspace to the zero quantum coherence subspace, $\mathfrak{L}_2 \subset \mathfrak{L}^0$, whereas the subspace containing the Zeeman orders already resides in the zero quantum coherence subspace. The equation of motion

$$\frac{\mathrm{d}}{\mathrm{d}t}|\hat{\rho}\rangle = \hat{\hat{\mathscr{L}}}|\hat{\rho}\rangle + l,$$

where $\hat{\hat{\mathscr{L}}}$ is the Liouvillian of the spin system and l contains the thermal correction, can in general be rewritten as

$$\begin{aligned}
\frac{\mathrm{d}}{\mathrm{d}t}|\hat{\rho}_1\rangle &= \hat{\hat{\mathscr{L}}}_{11}|\hat{\rho}_1\rangle + \hat{\hat{\mathscr{L}}}_{12}|\hat{\rho}_2\rangle + l_1 \\
\frac{\mathrm{d}}{\mathrm{d}t}|\hat{\rho}_2\rangle &= \hat{\hat{\mathscr{L}}}_{21}|\hat{\rho}_1\rangle + \hat{\hat{\mathscr{L}}}_{22}|\hat{\rho}_2\rangle + l_2,
\end{aligned} \qquad (3.7.1)$$

using the projections

$$|\hat{\rho}_k\rangle = \hat{\hat{\pi}}_k|\hat{\rho}\rangle, \qquad l_k = \hat{\hat{\pi}}_k l,$$

$$\hat{\hat{\mathscr{L}}}_{jk} = \hat{\hat{\pi}}_j\hat{\hat{\mathscr{L}}}\hat{\hat{\pi}}_k : \mathfrak{L}_k \to \mathfrak{L}_j, \quad j,k = 1,2.$$

The superoperator $\hat{\hat{\pi}}_k$, first defined in section 3.5.1, projects the operators into the subspace $\mathfrak{L}_k$. The subspaces $\mathfrak{L}_k$ are closed under the action of $\hat{\hat{\mathscr{L}}}_{kk}$, whereas the components $\hat{\hat{\mathscr{L}}}_{jk}$, with $j \neq k$, cause a transfer of magnetisation into the respectively other subspace. Formally integrating the equation for $\frac{\mathrm{d}}{\mathrm{d}t}|\hat{\rho}_2\rangle$ in 3.7.1 and substituting the solution into the equation for $\frac{\mathrm{d}}{\mathrm{d}t}|\hat{\rho}_1\rangle$ results in an integro-

differential equation:

$$\frac{\mathrm{d}}{\mathrm{d}t}|\hat{\rho}_1(t)\rangle = f(t) + \hat{\mathscr{L}}_{11}|\hat{\rho}_1\rangle + \int_0^t \hat{\hat{\mathrm{K}}}(t-\tau)|\hat{\rho}_1(t)\rangle \mathrm{d}\tau$$

$$\text{with } \hat{\hat{\mathrm{K}}}(T) = \hat{\hat{\mathscr{L}}}_{12} e^{\hat{\hat{\mathscr{L}}}_{22}T} \hat{\hat{\mathscr{L}}}_{21} \tag{3.7.2}$$

$$\text{and } f(t) = l_1 + \hat{\hat{\mathscr{L}}}_{12} e^{\hat{\hat{\mathscr{L}}}_{22}t} \left[|\hat{\rho}_2\rangle(0) + \int_0^t e^{-\hat{\hat{\mathscr{L}}}_{11}\tau} l_2 \mathrm{d}\tau \right].$$

Just as in section 3.5.1, the initial density operator $|\rho(0)\rangle$ lies in $\mathfrak{L}_1$ and is assumed to be equal to $\hat{\mathrm{S}}_z$. Hence l_2 is zero, as well as $|\hat{\rho}_2\rangle(0)$ and thus $f(t)$ is in fact a constant and equal to l_1. The term $|\hat{\rho}_2(t)\rangle$ does therefore not appear in equation (3.7.2) and the trajectory of the system is confined to the subspace $\mathfrak{L}_1$. The subspace $\mathfrak{L}_1$, spanned by the Zeeman order basis operators, scales with 2^N, where N is the number of spins in the sample.

One can define the polarisation subspace $\mathfrak{L}_{pol} \subset \mathfrak{L}_1$ containing only the single spin Zeeman orders $\hat{\mathrm{S}}_z, \hat{\mathrm{I}}_{1z},...,\hat{\mathrm{I}}_{Nz}$. This is the subspace of interest for the DNP simulations and its size is N. Noting that the initial density operator belongs to $\mathfrak{L}_{pol}$, one can investigate the action of the operators $\hat{\hat{\mathscr{L}}}_{11}$ and $\hat{\hat{\mathrm{K}}}(T)$ on the operators of the polarisation subspace. The operators $\hat{\hat{\mathscr{L}}}_{kk}$ and $\hat{\hat{\mathscr{L}}}_{jk}$ are given in the appendix D.

The action of the operator $\hat{\hat{\mathscr{L}}}_{11}$ on an element of the polarisation subspace is confined to this subspace: No higher Zeeman orders are generated when $\hat{\hat{\mathscr{L}}}_{11}$ is applied to a member of the polarisation subspace $\mathfrak{L}_{pol}$. The operator $\hat{\hat{\mathrm{K}}}(T)$ is not strictly closed in $\mathfrak{L}_{pol}$ but if the following conditions are obeyed, the higher Zeeman order terms that are generated by it, can be neglected:

$$\varepsilon_1 T_0 < 1, \text{ with } \varepsilon_1 = \frac{|A_j|}{2R'_{2k}} \text{ and } k, j \in [1, N-1], j \neq k,$$

$$\varepsilon_2 = \frac{d_{jk}^2}{2r_{jk}'^2} \ll 1, \qquad \varepsilon_3 = \frac{\omega_1^2 |B_k^2|}{8\omega_I^2 R_{2k}'^2} \ll 1 \tag{3.7.3}$$

where $r'_{jk} = r_{2n}(j) + r_{2n}(k)$ is the sum of the nuclear transverse relaxation rates of spin j and k, $R'^2_{2k} = r_{2e} + r_{2n}(k)$ is the sum of the electronic transverse relaxation rate and the nuclear transverse relate of spin k. The factor T_0 is ob-

tained from an integral convergence condition in the operator $\hat{\hat{K}}(T)$, and due to a transformation of variables used in the derivation it is dimensionless. T_0 is not dependent on the interaction and relaxation constants and its required value will be determined from the error analysis. It is noteworthy that the conditions 3.7.3 are not dependent on the number of spins in the simulation, as it was the case for the spin correlation order basis truncation method.

The precise steps made to arrive at the conclusion that the conditions (3.7.3) ensure the trajectory remains in $\mathfrak{L}_{pol}$ were not discussed, but they involve applying $\hat{\hat{K}}$ to the operators spanning $\mathfrak{L}_{pol}$ and analysing which resulting terms cause leakage of magnetisation into $\mathfrak{L}_1$. These terms can then be neglected if the conditions (3.7.3) are fulfilled.

The equation of motion can now be described by the differential equation

$$\frac{\mathrm{d}}{\mathrm{d}t}|\hat{\rho}_{pol}\rangle = \hat{\hat{M}}_0|\hat{\rho}_{pol}\rangle + l_1,$$

with

$$\hat{\hat{M}}_0 = \hat{\hat{\mathscr{L}}}_{11} + \hat{\hat{K}}|_{pol}.$$

$\hat{\hat{K}}|_{pol}$ is the component of operator $\hat{\hat{K}}(T)$ that is closed in $\mathfrak{L}_{pol}$ if the conditions 3.7.3 hold. The action of the operator $\hat{\hat{M}}_0$ on the single spin operators results in only single spin components (see equation 3.7.4).

$$\frac{\mathrm{d}}{\mathrm{d}t}\hat{\hat{S}}_z = -R_1'\hat{\hat{S}}_z - \frac{\omega_1^2}{8\omega_I^2}\sum_k^{N-1}|B_k|^2 c_k\left(\hat{\hat{S}}_z - \hat{\hat{I}}_{kz}\right),$$

$$\frac{\mathrm{d}}{\mathrm{d}t}\hat{\hat{I}}_{kz} = -r_{1k}'\hat{\hat{I}}_{kz} + \frac{\omega_1^2}{8\omega_I^2}|B_k|^2 c_k\left(\hat{\hat{S}}_z - \hat{\hat{I}}_{kz}\right) - \frac{1}{2}\sum_{j\neq k}^{N-1}d_{jk}^2 c_{jk}'\left(\hat{\hat{S}}_z - \hat{\hat{I}}_{kz}\right).$$

(3.7.4)

Hence the dynamics is closed in the polarisation subspace under the action of

$\hat{M}_0$. The newly introduced coefficients are:

$$c_k = \int_0^{+\infty} e^{-R'_{2k}T} \cos(\omega_I T) \prod_{j \neq k}^{N-1} \cos\left(\frac{A_j T}{2}\right) dT$$

$$c'_{jk} = \frac{r'_{jk}}{r'^2_{jk} + \frac{1}{4}(A_j - A_k)^2},$$

$$R'_1 = R_1 + \frac{\omega_1^2}{\omega_I^2}(R_2 - R_1),$$

and

$$r'_{1k} = r_{1k} + \frac{|B_k|^2}{\omega_I}(R_1 - r_{2k} - r_{1k})$$

The multi-exponential character of the polarisation build-up curves is introduced via the constants c_k. The evolution of the system can thus be described by N coupled equations. Using a computer equipped with 8 GB RAM it is then possible to simulate up to 16.000 spins. This treatment was based on the initial condition being in the polarisation subspace , $|\rho_1(0)\rangle \in \mathfrak{L}_{pol}$, which holds to a good approximation if the sample temperature is about 1 K or above. At lower temperatures the initial density operator would contain higher Zeeman orders, and thus not be an object of $\mathfrak{L}_{pol}$ alone.

3.7.2 Error Analysis

In order to test the validity of the projection method, five random configurations of five ^{13}C - nuclei around an electron at the origin of the coordinate system were defined. The maximum and minimum distance from the electron was 24Å and 12Å respectively, which is the the same as was used for the investigation of the spin correlation order basis truncation. The closest distance of approach between the nuclei was set to 5Å. The number of nuclei was kept small in order to enable the use of the full basis in SPINACH, making it possible to scale the interaction constants and relaxation rates beyond the scope of the spin correlation order basis truncation method. The interaction parameters A_k, $B_{k\pm}$, d_{jk}

were scaled separately, resulting in individual scaling of the constants ε_1, ε_2, and ε_2. The relaxation rates r_{2n} and r_{2e} were also scaled. For the tests a relaxation operator with the same relaxation rates for all nuclei was used to allow for easier control of the ε constants. For each configuration the polarisation build-up is calculated using SPINACH with the averaged Hamiltonian and the new projection method. The results from SPINACH are used as a reference for the projection method.

The results are summarised in figure 3.24, where the average absolute error with error bars indicating the standard deviation is plotted. The average was taken over all nuclear polarisation build-up curves and all configurations. As interaction constants are scaled up, the standard deviation also becomes larger. This is due to the fact that for some nuclei with strong interaction constants, the error increases more dramatically than for other nuclei, with interaction constants close to zero. Overall this results in a larger spread of error values and hence a larger standard deviation. The initial input parameters are summarised in Table 3.5. These are the starting conditions for each figure, with only the parameter indicated in the figure being scaled.

Table 3.5: Initial conditions for the error analysis of the projection method

r_{1n}	$0.01\,\frac{\text{rad}}{\text{s}}$
r_{2n}	$10^4\,\frac{\text{rad}}{\text{s}}$
r_{1e}	$10^3\,\frac{\text{rad}}{\text{s}}$
r_{2e}	$10^6\,\frac{\text{rad}}{\text{s}}$
ω_1	$1\,\text{MHz}$
$\langle|A_k|\rangle$	$(5.7 \pm 3.3)\,\text{kHz}$
$\langle|B_k|\rangle$	$(4.6 \pm 1.3)\,\text{kHz}$
$\langle|d_{jk}|\rangle$	$(45 \pm 38)\,\text{kHz}$
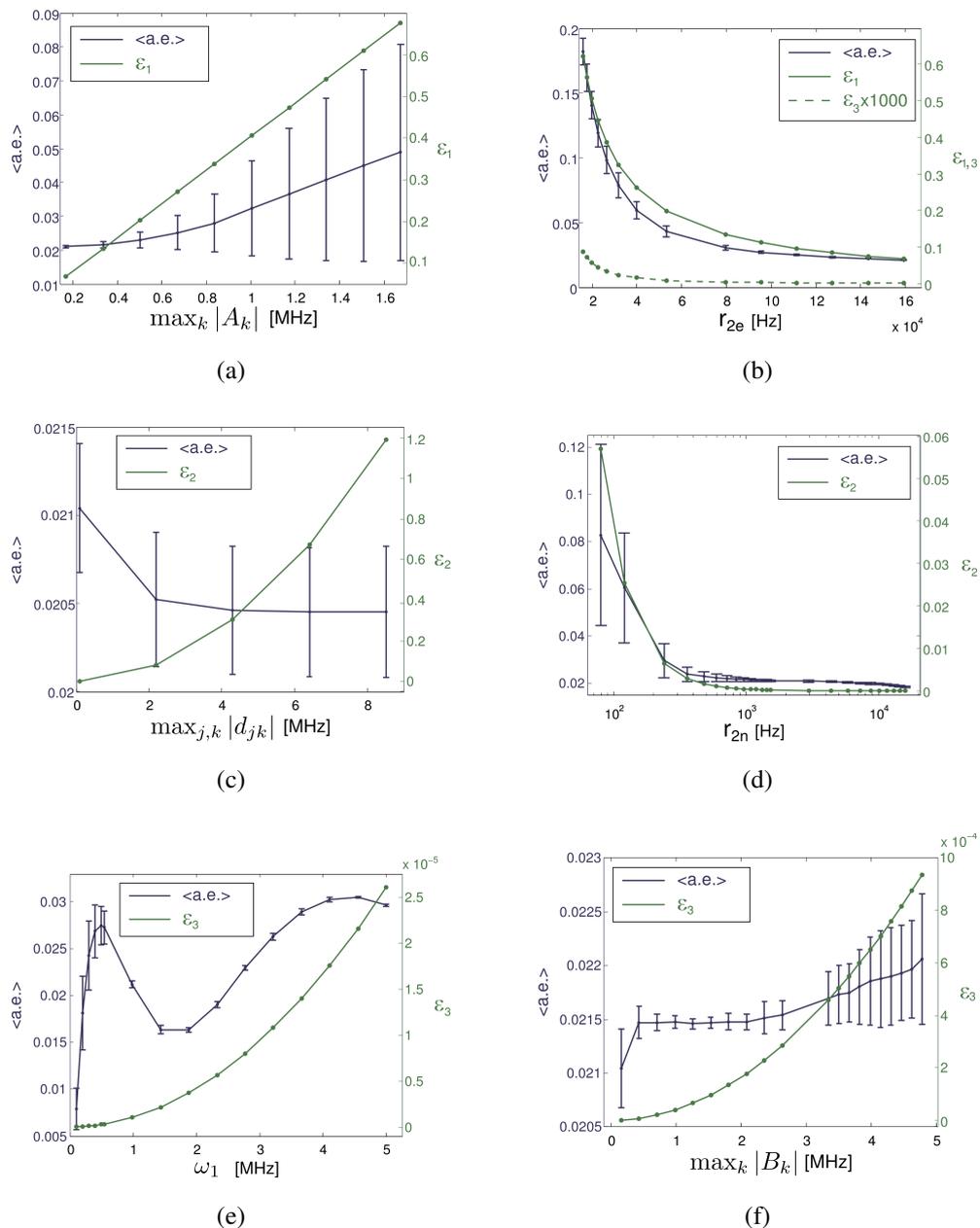
Figure 3.24: Average absolute errors for scaling of input parameters with error bars indicating the standard deviation.

Scaling of the hyperfine interaction constant A_k (see figure 3.24a) results in a change in ε_1. In order for the error to remain below a tolerance level of 0.05 the secular hyperfine interaction constants should not be larger than $\cong 1.2$ MHz, if one takes the largest values of the error bars into account. For ^{13}C nuclei this

112

would correspond to a closest distance of approach to the electron of 3.5Å. If the Trityl radical is considered in the simulation, this distance should in principle not be reached. For the simulation of ^{1}H nuclei this condition is more critical: the closest distance of approach corresponding to $A_k \cong 1.2\,\text{MHz}$ is 5.5Å.

From figure 3.24b it can be seen that the electron transverse relaxation constant should not drop below 45 kHz if the error is to remain below 0.05. As scaling the electron transverse relaxation rate affects ε_1 as well as ε_3, the scaling of both constants is shown. Due to the division by ω_I^2 in the definition, ε_3 it remains very small and had to be scaled up by a factor of 10^3 in order to be visible. Comparison of figures 3.24a and 3.24b reveals that the error is more sensitive to scaling of ε_1 via the electronic transverse relaxation rate than via scaling A_k: The error tolerance of 0.05 is reached when $\varepsilon_1 \approx 0.4$ for a scaling of A_k but when scaling r_{2e} the same error is reached when ε_1 is only 0.2. From this the parameter T_0 is determined to be approximately 1.25 and 2.5, obtained from the scaling of A_j and r_{2e} respectively and using the condition for ε_1 in (3.7.3). The numerical integration in operator $\hat{\hat{\text{K}}}$ should be done up to the larger T_0 in order to err on the side of caution. The integration is done with the MATLAB function *quadgk()*, which is very fast and increasing the upper limit of the integral does not lead to a notable reduction in simulation speed.

Scaling of the nuclear dipole interaction displays very little change in the error, even when scaling d up to unrealistically large values and ε_2 becomes larger than 1 (see figure 3.24c). The dependence of the error on scaling the transverse nuclear relaxation rate is on the other hand noticeable. The nuclear transverse relaxation rate should not drop below 200 Hz in order to keep the error below the 0.05 tolerance.

The parameter ε_3 was found to be least critical as it contains the nuclear Larmor frequency ω_I squared, and hence this parameter is always much smaller than 1 (see figures 3.24e and 3.24f).

The projection method has also been tested with ten random configurations of 20 ^{13}C spins and one electron, where the nuclei are again positioned within a distance of r$\in$[12,24]Å from the electron, and the internuclear distance is not smaller than 3.5Å. For the simulation in SPINACH the averaged Hamiltonian as well as a truncation of the basis to third order spin correlation is used. The largest absolute error of the build-up curves obtained from the projection method, with respect to the simulation carried out in SPINACH, was found to be $1.8 \cdot 10^{-2}$, the average error over all ten configurations was $(1.2 \pm 0.7) \cdot 10^{-2}$. The results of the simulation of one of the random configurations is shown in figure 3.25.

For easier error analysis the constant relaxation operator was used. When using the scaled relaxation operator it is possible that some of the nuclear transverse relaxation rates r_{2e} become too small and the error for the projection method increases. However, as for example the average electron distance in a sample containing 15mM Trityl is 48Å, the value for r_{2e} should not become too small because the next electron is not too far away. One could introduce a more realistic relaxation operator which adds a basic relaxation rate onto the scaled rates. This avoids singularities of the nuclear relaxation times at the points where either A_k or B_k are zero and ensures that ε_2 in the conditions 3.7.3 remains small.

In summary, it was found that for a realistic set of input parameters the error incurred when using the projection method remains small, i.e. below the tolerance level of 0.05. This is certainly true for the model system of 1M ^{13}C nuclei positioned around an electron with the closest distance of approach of 12Å as is the case for the Trityl radical.

(a)   (b)
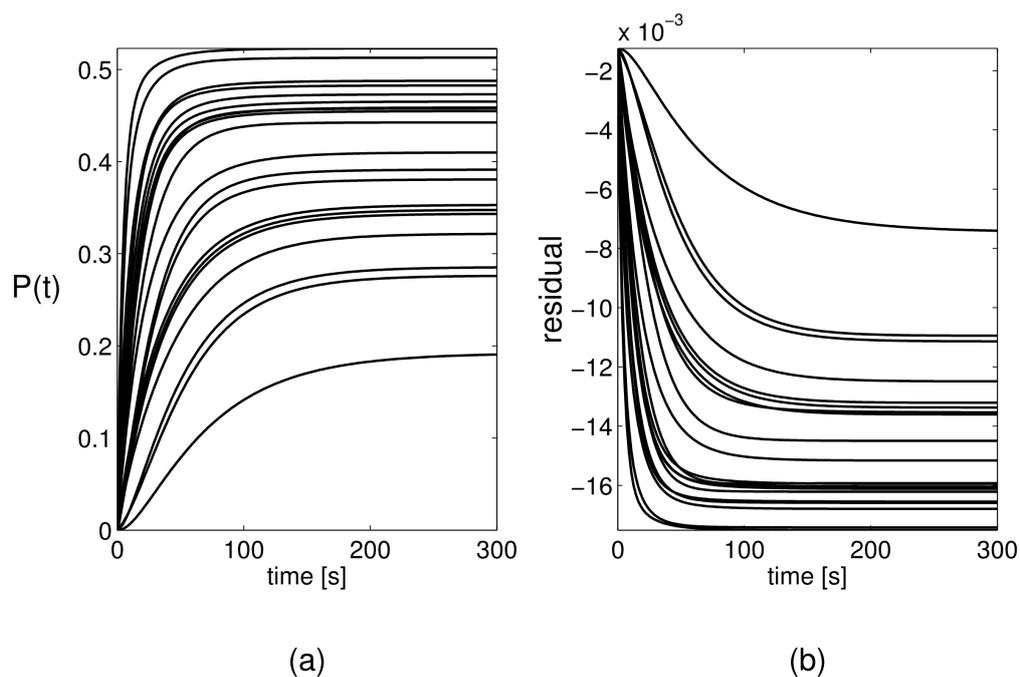
Figure 3.25: (a) Polarisation build-up of 20 nuclei calculated with the projection method and (b) the difference to the build-up curves obtained from SPINACH , using basis truncation of higher than third order spin correlations and the averaged Hamiltonian. The processing time for calculating the simulation with SPINACH was 4 hours, whereas with the projection method it was less than a second. ω_1=1 MHz and the constant relaxation operator was used with: $r_{1e} = 10^3$, $r_{2e} = 10^6$, $r_{1n} = 0.01$, $r_{2n} = 10^5$. All relaxation rates are given in $\frac{\text{rad}}{\text{s}}$.

3.7.3 Visualisation of the propagation of nuclear spin polarisation

The projection method has been used to calculate the build-up and distribution of polarisation in a sample of more than a thousand nuclei. The electron was positioned at the origin of the coordinate system and the nuclei were placed on a cubic lattice with a nearest neighbour distance of 12Å. The position of the nuclei was randomised within 5% of the exact lattice position to avoid an overly symmetric system. The number of nuclei in one edge of the cube was 11 resulting in 1330 nuclei in total. The constant relaxation operator was used in order to avoid very small transverse nuclear relaxation rates which would lead to a larger error in the projection method. The same simulation was carried out twice, once with and once without taking the nuclear dipole interaction into account. The processing time was one minute for each case. The resulting polarisation build-up curves, as well as the difference between the two, are shown in figure 3.26. For the difference,the positive curves correspond to the nuclei gaining polarisation as a result of the inclusion of nuclear dipole interaction. The negative curves correspond to the nuclei which have less polarisation when nuclear dipole interaction is taken into account.

The drawback of displaying the polarisation build- up curves as in figure 3.26 is that one does not know the location of the spins corresponding to each curve. A more informative way of visualising the polarisation build-up has been attempted in figure 3.27. The configuration of the spin system is shown, with the size of the dots, corresponding to the nuclei, indicate the level of polarisation. Three points in time (corresponding to the blue triangles in figure 3.26) are displayed.

The polarisation of the nuclei further removed from the electron remains close to zero when nuclear dipole interaction is excluded, demonstrating the importance of spin diffusion for the polarisation build-up in the sample. The polarisation in

(a) All spin-spin interactions included

(b) Nuclear dipole interaction set to zero

(c) Difference of the above: Effect of spin diffu-
sion.
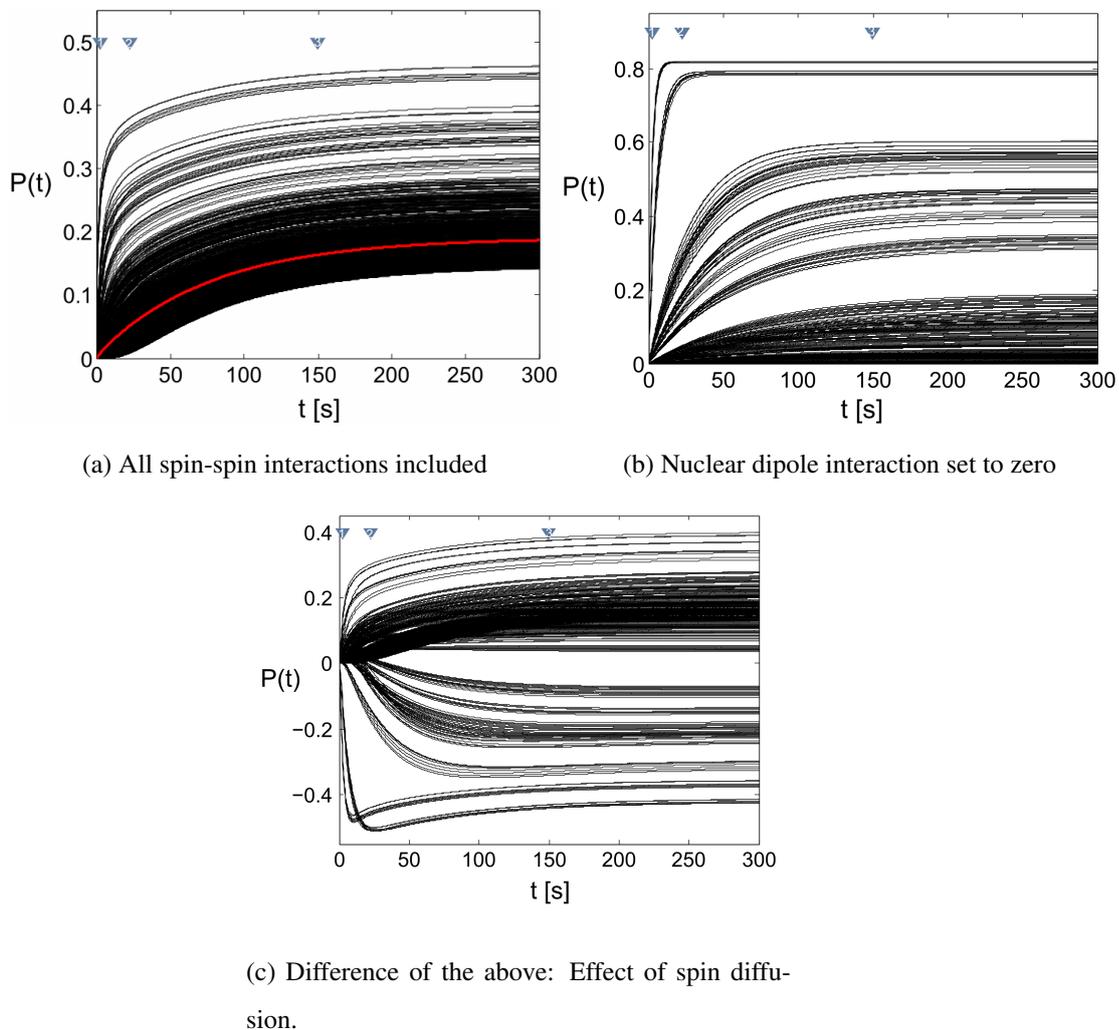
Figure 3.26: Polarisation build-up of 1330 nuclei, calculated with the projection method. Simulation parameters: microwave strength ω_1=2 MHz, the constant relaxation operator was used with: $r_{1e} = 10^3$, $r_{2e} = 10^6$, $r_{1n} = 0.01$, $r_{2n} = 10^5$. The red line shows the average polarisation build up of the nuclei with a hyperfine interaction constant A_k of less than 500 Hz, so the spins that can reasonably be expected to be observable in an NMR experiment.
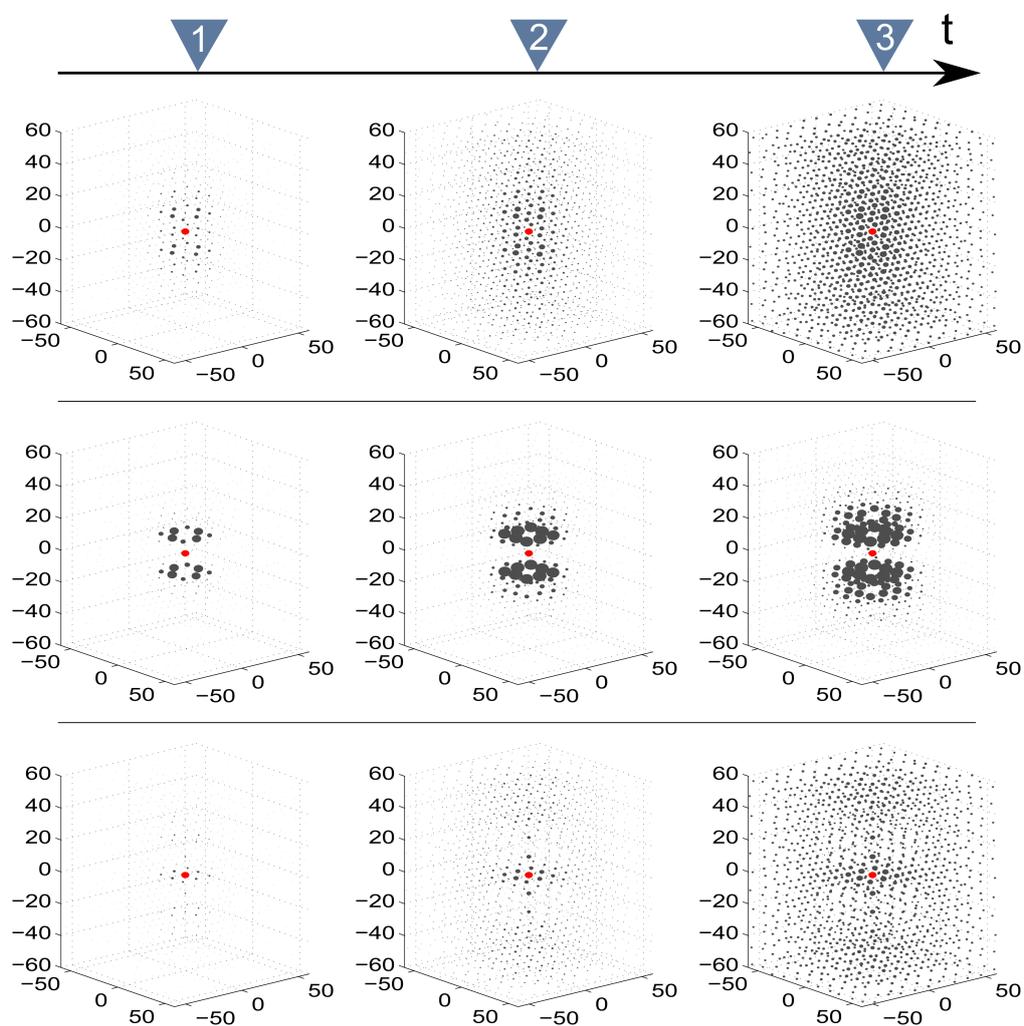
Figure 3.27: Polarisation build-up through space visualised by the size of the dots, corresponding to the nuclei. The electron is depicted in red. All axes units are in Å. Top row: all interactions included. Middle row: nuclear dipole interaction set to zero. Bottom row: difference between including and excluding nuclear dipole interaction, where nuclei having relatively less polarisation when nuclear dipole interaction is included are not shown.

the xy-plane, as well as along the z-axis, remains zero due to the fact that the hyperfine interaction constant $B_{k\pm}$ is zero for the angles $\theta = \frac{\pi}{2}$ and $\theta = 0$, and no indirect polarisation via the nuclear dipole interaction can take place. When nuclear dipole interaction is included, the polarisation is distributed faster in the z direction than the xy-plane as the nuclear dipole interaction constant scales with $1 - 3\cos^2\theta$.

3.7.4 Discussion

It was shown that it is in principle possible to simulate 16,000 spins on a desktop computer using a subspace projection method. If one were to tap into commercially available cloud computing power, where the processor memory can be up to one Terra-byte, simulations of spin systems containing on the order of $2 \cdot 10^5$ spins are within realistic reach. This makes it possible to compare the quantum mechanical model to thermodynamical models of DNP. The processing time still scales exponentially with the propagator size, but as the propagator itself now scales linearly, the reduction in simulation duration is dramatic. For the case of 20 nuclei and one electron it was mentioned that the processing time reduced from 4 hours to less than a second and it is worth noting that the simulation of the 20 nuclei in SPINACH was carried out using an already reduced state space. Adding electrons for a more realistic picture is also possible, as long as the electron dipole interaction remains appreciably smaller than the nuclear Larmor frequency. This requirement comes from the averaged Hamiltonian treatment, where all interaction constants need to be smaller than ω_I.

Projection methods might be applicable also for other NMR simulations problems, as the nuclear Larmor frequency usually dominates the spin-spin interaction constants present in the sample. Depending on the case to be investigated, one could pick a subspace of interest and use the integro-differential equation to project the trajectory into it. One conceivable application is the simulation of spin diffusion. L. Emsley and co-workers have previously presented simulations with a reduced state space by using truncation to the zero quantum coherence subspace and a basis containing only up to fourth order spin correlations [60, 61, 70]. Using the projection method, simulation of spin diffusion could be carried out using one equation per spin.

CHAPTER 4

NMR spectroscopy using multiple coils and receivers

It was mentioned in chapter 2 that dissolution DNP experiments allow for only a single full excitation to be carried out. After the hyper-polarised signal has decayed to the Boltzmann equilibrium with the characteristic T_{1n} constant, time consuming re-polarisation has to be carried out before another experiment with non-thermal polarisation can be performed . Investigations of molecular dynamics are thus limited by the single shot nature of dissolution DNP. Nonetheless, there are several possibilities to study time-transient dynamics using the hyper-polarised NMR signal. Either a low flip angle excitation is used in consecutive acquisitions of the signal, or the polarisation in the sensitive region of the coil could be replenished in a stop-flow experiment. Low flip angle excitations of samples undergoing a chemical reaction have successfully been used by the C. Hilty group to study reaction rates with time constants on the order of seconds to hundreds of milliseconds [38, 39].

A new possible approach for fast repetition of an experiment on a polarised samples will be examined in this chapter. The idea is to use more than just one RF coil to acquire spectroscopic data from different locations of the sample. All RF coils are tuned to the same frequency and able to independently perform experi-

ments with the use of separate transmit and receive channels for each coil. This
strategy has the advantage that the signal acquisition from one coil can already
be started before another coil is finished. In order to observe dynamics stem-
ming from chemical reactions or protein-ligand binding, the substrate molecule
could be polarised, rapidly mixed with the target molecule or enzyme and in-
jected into the probe. Alternatively the target molecule could readily be placed
in the probe and mixing take place inside the probe upon substrate injection.
After a settling delay, the acquisition from the different coils could be started in
an arrayed fashion, enabling the fast study of the reaction. The goal is to imple-
ment a novel strategy for studies of molecular dynamics with time constants on
the order of a few milliseconds.

NMR probes that comprise multiple RF-coils tuned to the same resonance fre-
quency have previously been used to increase the speed of spectroscopic exper-
iments. For example, Raftery et al. constructed a probe that can acquire four
experiments simultaneously on different samples, which could be used to in-
crease throughput [71, 72]. Webb et al. reported the successful implementation
of 2D pulse sequences on a four coil probe, where the t_1 evolution has been
divided between the coils [73]. This resulted in an increase in the speed of the
acquisition by a factor of four. In these examples solenoid coils are used as RF
coils, which require the sample tube to be aligned perpendicular to the external
magnetic field. The advantage for this configuration lies in the ability to com-
pletely shield the environment of the RF-coils with grounded copper plates that
act as RF shields. The drawback of such a configuration lies in a more com-
plex probe geometry with specially manufactured sample tubes that split into
multiple flow channels. Particularly with respect to the frequently observed gas
bubble formation, that is a known issue of dissolution DNP, a simple tube ge-
ometry is more desirable than a complex flow path. A further drawback of the
solenoid coil geometry is that for the fast 2D spectroscopic experiments, where
strong gradients are desired the weaker X or Y gradient would have to be used

for spatial encoding of the t_1 evolution. For these reasons, saddle coils were
chosen for the multiple RF-coil probes presented in this chapter.

In this chapter, first the prototype of a probe with two independent transmit
and receive coils tuned to the ^{1}H frequency of 400 MHz, will be introduced. A
procedure for field map based simultaneous shimming of both coils has been
implemented and will be presented. Then the extension of the two coil probe
towards a six coil probe, tuned to the ^{13}C frequency of 100 MHz which has
been developed in a collaboration with Bruker, will be discussed and initial data
shown.

4.1   Spectrometer

A Bruker Avance III spectrometer console with six independently controlled
transmit and receive channels, which are suitable for proton and broadband ex-
periments, is used. The six channels can either be set up as six broadband chan-
nels or as three proton and three broadband channels running in parallel. The
magnet, provided by Oxford Instruments , has two iso-centres (3.4 T and 9.4 T)
spaced 0.8 m apart. The 9.4 T region is used to perform NMR experiments, the
field strength corresponds to a proton Larmor frequency of 400 MHz. The 3.4 T
region can be used to hyper-polarise the sample. This is then rapidly shuttled
to the 9.4 T region with the use of an actuator. During the transfer the sample
is in the solid state, which in conjunction with a shuttling time of less than a
second, allows to maintain the level of polarisation to a high degree. After that
the dissolution and transfer into the sample tube follows. A detailed description
of the set up and procedure can be found in [46].

4.2   Dual coil probehead

In order to test the idea of using multiple receive and transmit RF coils at different locations of the sample, first a probe containing two separate RF circuits was built. The observe nucleus was chosen to be ^{1}H for this pilot project for the higher signal to noise ratio protons offer compared to lower-γ nuclei.

4.2.1   Design and Parameters

The probehead comprises two separate resonant circuits with RF saddle coils tuned to the proton Larmor frequency of 400 MHz. A simple diagram of the resonance circuit of one coil is shown in fig. 4.1. The impedance of the reso-
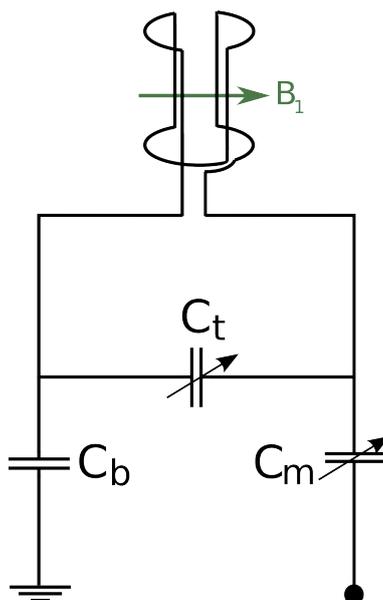
Figure 4.1: Diagram of the resonance circuit of one coil. The coil is displayed as a saddle coil in order to point out the geometry and resulting B_1 field. C_t and C_m are the tuning and matching capacitors respectively and C_b is introduced into the circuit for balancing.

nance circuit can be matched to the impedance of the connected electronic components of the spectrometer with the use of the variable capacitor C_m, which

enables maximum power transfer between them. Changing the capacitance of
the matching capacitor introduces a change in the resonance frequency, hence
the tuning capacitor C_t is used to re-tune the probe to the desired 400 MHz.
The capacitors C_t and C_m have a variable capacitance with range from (1-10) pF
and each RF coil has an inductance of $(1.2 \pm 0.5)\,\mu$H. A single sample tube of
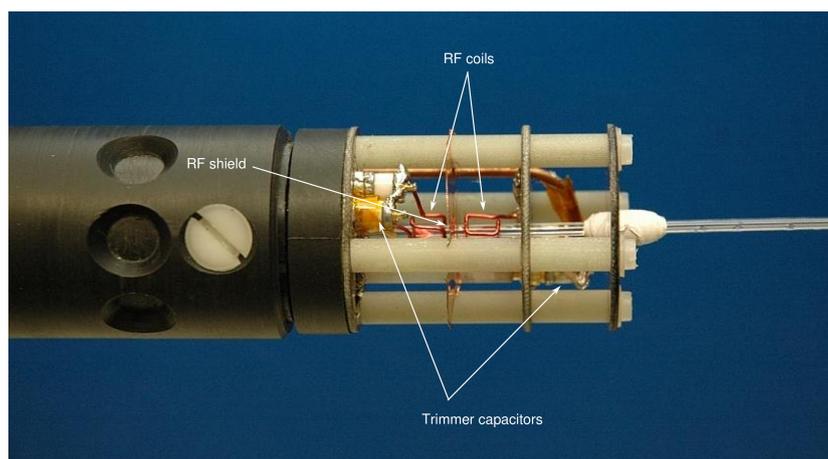
Figure 4.2: Photo of the dual coil probe.

2.5 mm outer diameter (and 2.1 mm inner diameter) extends through both coils
as is shown in figure 4.2. The coils have a diameter of 4 mm and the excited
sample length per coil is 6 mm. Saddle coils were chosen for their geometry,
which results in vertical positioning of the sample tube which in turn enables
easier sample injection from the top.

4.2.2 Coupling

Despite the strong coupling that was expected as a result of the close vicinity
of the coils, they were chosen to be positioned only 2 mm apart. This has two
reasons: Firstly the shimming of the magnetic field, so the cancellation of small
deviations in the external field with a set of orthogonal shim coils[1], becomes
increasingly difficult with larger coil separation and secondly the extent of the

---

[1]More about shimming will be discussed in section 4.2.3.

homogeneous field region in the z-direction is only on the order of 2 cm. Coupling was minimised by choosing an orthogonal set up of the RF coils and a grounded copper RF shield that was placed in the xy plane between the coils. In order to allow the sample tube to extent into both coil regions a hole of the diameter of the tube has to be placed in the RF shield. This inevitably allows a certain degree of coupling between the two circuits. With a network analyser the cross talk between the coils was found to be -24.5 dB, which is small enough so the power absorption ('wobble') curve does not display a doublet due to coupling, but instead a single absorption peak.

The probe was loaded with a sample of 20% H_2O and 80% deuterated water. When applying a $\frac{\pi}{2}$ pulse on one coil and detecting on both, a small peak also appeared on the passive coil. The integral of the peaks of both coils was calculated, and normalised to the integral of the active coil. The signal appearing on the passive coil was found to be 14% with respect to the active coil signal. Three possibilities were identified as a potential source for the cross talk:

- Inductive coupling between the coils. This would cause the second coil to apply a pulse onto the sample in its region even when it does not receive power from its own transmitter.

- The extend of the B_1 field of one coil stretches into the region of the other coil through the hole in the RF shield. Here the sample would be directly excited by the other coil.

- Indirect non-resonant coupling of electronic components that allows power, that was directed to one channel to be transferred to the other. Here signal that is coming from one channel could be seen on the other.

The two first possibilities were eliminated by closing the hole in the RF shield between the coils, and placing two separate,cut off sample tubes in either coil. No change in the coupling strength was observed. To test the third possibility

one coil was detuned and poorly matched and the other used for excitation. In order to determine the signal origin a gradient echo z-projection experiment was used, where the field of view was chosen large enough to extend over both coils. In figure 4.3 the z-profiles of the two coils are displayed, the detuned coil is on the left, and the active coil on the right. The dashed line depicts the profile acquired on the active coil, the full line the acquisition on the detuned coil (no pulse was applied on the detuned coil). It is clear that the detuned, passive, coil picks up the signal from the active coil. As the passive coil is detuned and so unable to acquire signal within the excited bandwidth this small, but visible signal must be introduced into the passive coil circuit via non-resonant coupling of the electronic components in the probe. This could probably be removed by careful isolation of the circuits by introducing shielding.

4.2.3 Shimming

Although the main external magnetic field is designed to be very homogeneous, small deviations as a result of imperfections of the magnet are inevitable. Additional inhomogeneity is introduced upon insertion of an object into the field. This ΔB_0 originates at boundaries between materials of different magnetic susceptibility and can broaden the line width of the spectrum into a few hundred Hertz. Evening out these deviations in the main field is called 'shimming the magnet', which can be done with a set of resistive coils, that carry currents controlled by the user. These coils are designed to produce magnetic fields in the shape of the orthogonal spherical harmonic functions, as the field distribution can be represented in this basis. In high resolution spectroscopy still mostly manual shimming is used, where a simple small flip angle experiment is set up in a loop and the effect of the shim fields on the free induction decay (FID) is observed. The current in the shim coils is changed in order to minimise the rate of signal decay (see figure 4.4).
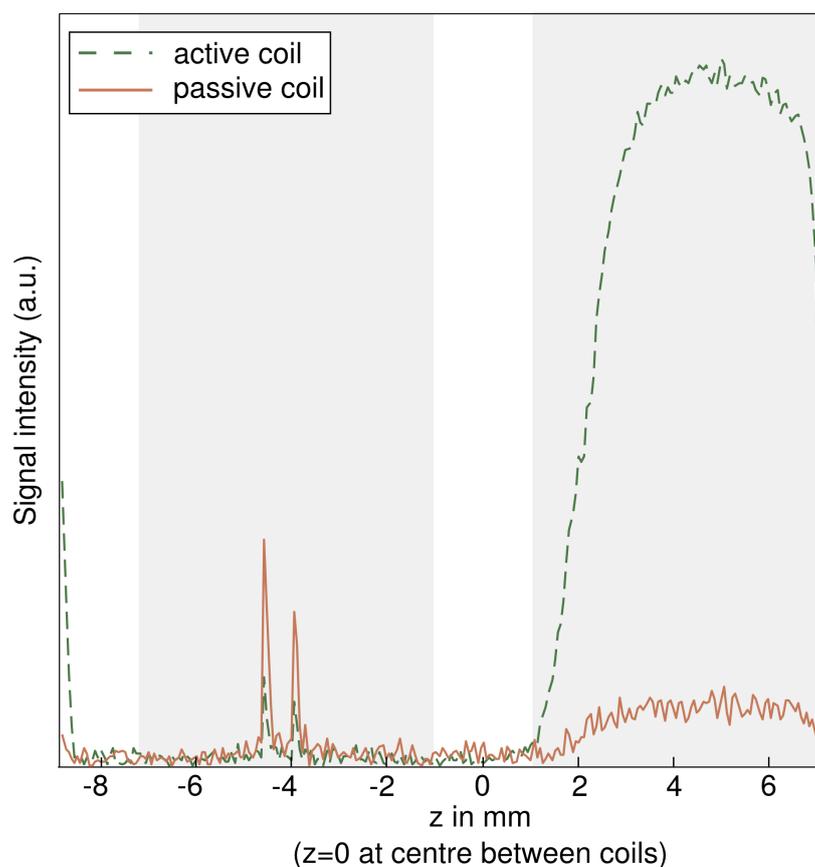
Figure 4.3: z projection along the sample tube. The passive coil is detuned beyond excitation bandwidth. The excitation of the active coil is visible in the profile of the passive coil. The grey shaded area marks the location of the sensitive region for each coil. The spikes in the sensitive region on the left has been attributed to receiver noise due to the large spectral width.

Achieving good shim settings for both coils of the dual coil probe at the same time proved to be difficult, as firstly the large amount of copper shielding that is situated around the coils for decoupling introduces a lot of susceptibility boundaries and secondly these susceptibility effects can look very different for each coil. Manual shimming is possible using a modified BRUKER acquisition software which displays the two FIDs simultaneously but it is difficult and time consuming to find the best possible compromise. Hence field map based shimming appeared to be a useful solution. This is based on acquiring maps of the
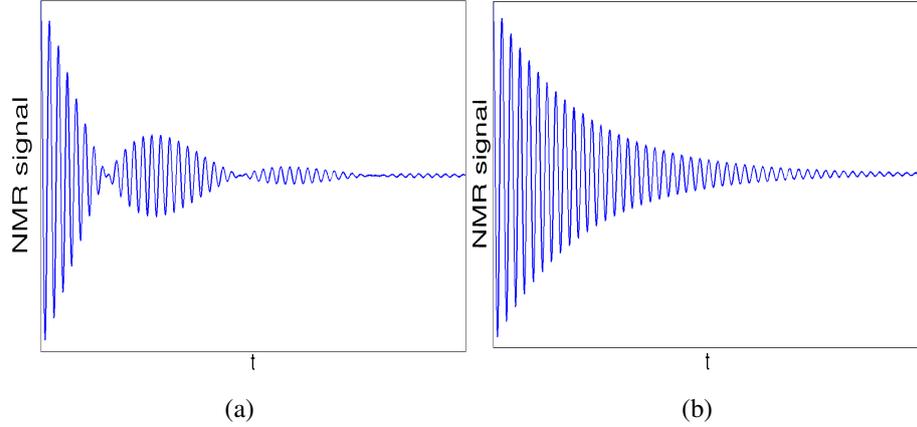
Figure 4.4: Simulated FIDs received from (a) a poorly-shimmed sample and (b) a well-shimmed sample.

distribution of the B_0 field and calculating the contribution of each spherical harmonic component to this field [74].

Mapping B_0

The B_0 field map can be obtained by acquiring gradient echo based images with incremented echo times *TE*. For the acquisiton of B_0 field maps on the two coil probe the FLASH MRI sequence has been used [75]. The local field distortions ΔB_0 modify the phase of the spins, so the phase difference $\Delta\phi$ that is accumulated in the time ΔTE due to these local deviations is related by

$$\Delta\phi(\mathbf{r}) = -\gamma\Delta B_0\Delta TE. \qquad (4.2.1)$$

In principle, only two different echo times are required to obtain $\Delta\phi(\mathbf{r})$ but to account for phase wrapping a third experiment is acquired. The phase ϕ for each complex image voxel with value $a + \iota b$ was calculated with

$$\phi = arctan(\frac{b}{a}).$$

After unwrapping in the phase, ΔB_0 was calculated using equation (4.2.1).

Calibration of the shims

The shim fields are calculated using spherical harmonics of up to second or-
der and additionally the third order Z shim. The following components were
included: $\{X,\ Y,\ Z,\ Z^2,\ X^2,\ Y^2,\ XY,\ X^2-Y^2,\ XZ,\ YZ,\ XY,\ Z^3\}$. The shim
fields are calculated in MATLAB using the *meshgrid()* function to define a grid
of points, which then are used to calculate the spherical harmonics functions.
For calibration, first a reference field map was acquired and then each shim sep-
arately changed to obtain the modification in the ΔB_0 field each shim causes for
a certain change in the shim units. Corrections were carried out for imperfec-
tions in the alignment of the gradient and shim coil configuration by shifting the
origin of the previously defined grid to match the obtained shim fields.

Shimming routine

For the shimming routine, written in MATLAB, the resolution and the field of
view (FOV) for the two coil unshimmed ΔB_0 imaging datasets is read in and a
grid of points in real space. is calculated. From this the spherical harmonics
functions are determined. A mask is applied for the ΔB_0 map of both coils to
cut out the regions extending outside the RF coil because an attempt to shim
the larger inhomogeneities in those regions might result in a worse shim at the
center of the coils. The two ΔB_0 map are combined into one, and then divided
by a matrix describing the calibrated shim fields on the previously defined grid.
This yields the shim currents required to minimise the deviation from the homo-
geneous field.

The shims have been calibrated for the dual coil probe and a 10 mm BRUKER
micro-imaging probe. For both probes the agreement between simulation and
experiment is very good, i.e. less than 3% deviation of the resulting field from
the calculated prediction. In figure 4.5 and 4.6 the outcome of shimming the
dual coil probe is illustrated. The root mean square of the combined ΔB_0 field

before shimming is 1.38 mT, the simulation predicts 0.56 mT for after shim-
ming and obtained was = 0.59 mT. This is a shimming efficacy of 56.5%, which
becomes significantly larger (over 80%) if only one coil is shimmed. In order
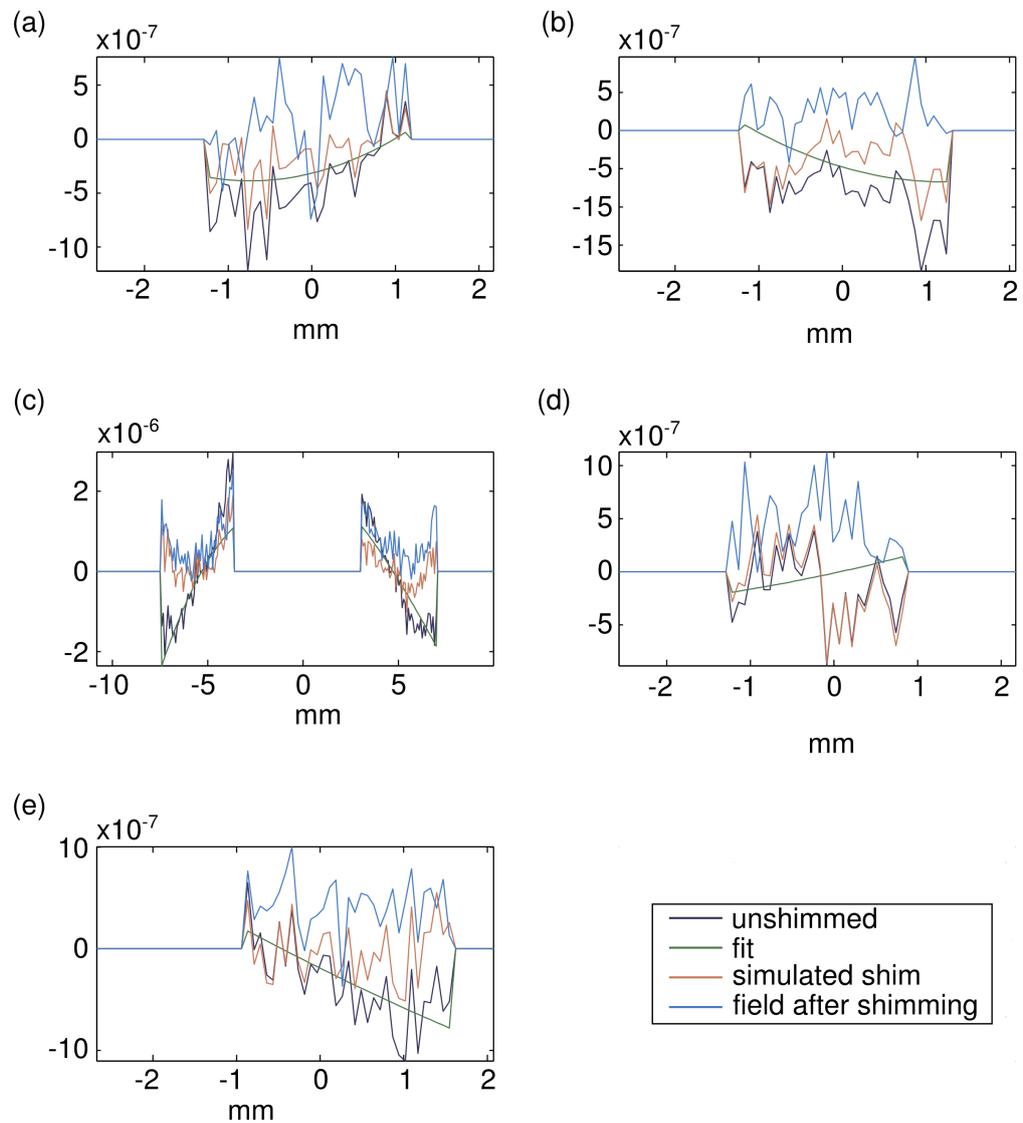
Figure 4.5: Fieldmap profiles before and after shimming. On the y axis the ΔB_0
field in units of Tesla is shown. The field of view was 5x5x20 mm^3. (a) x axis,
upper coil (b) y axis, upper coil (c) z axis, both coils (d) x axis, lower coil (e) y
axis, lower coil

to test the line shape, a slice selective excitation has to be used as the field map
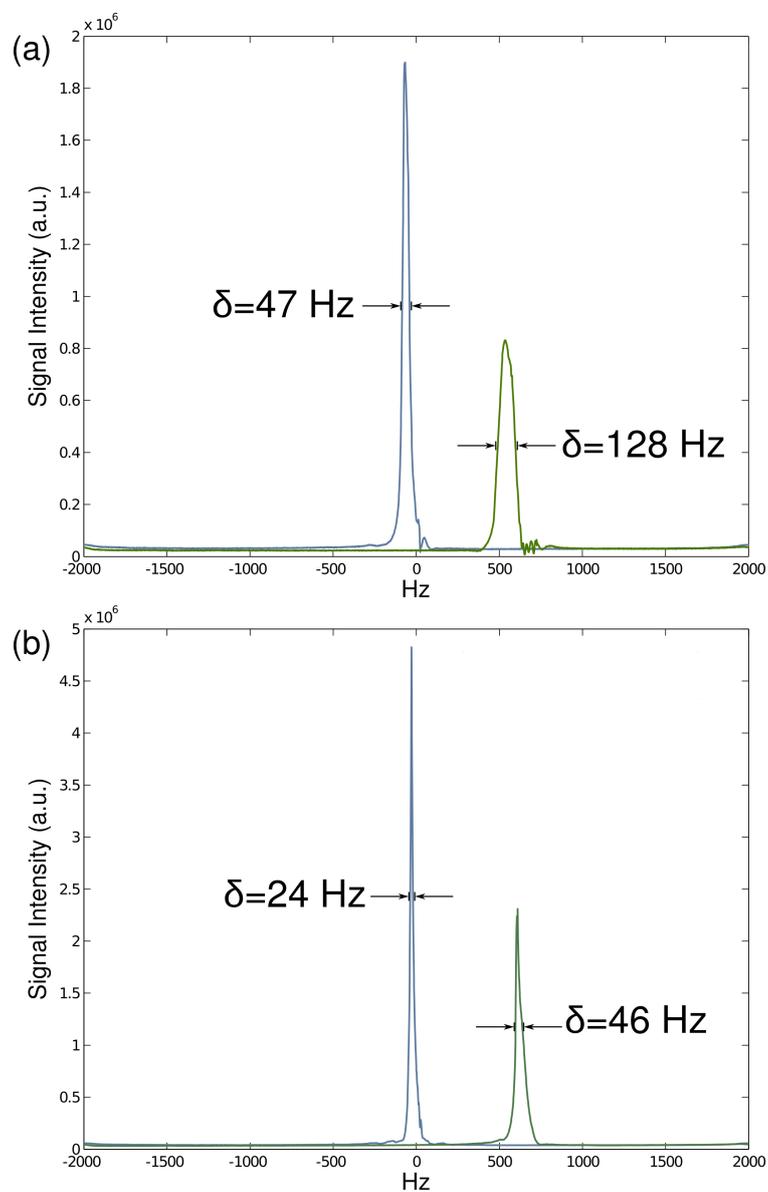
Figure 4.6: Linewidths for before (green line) and after the autoshimming. (a)
upper coil, (b) lower coil. Linewidths at full width-half maximum δ are indicated in the figure.

was masked before the shimming routine. This was done to avoid shimming the outer coil regions which are intrinsically more inhomogeneous. For slice selection a Gaussian RF pulse under a z-gradient was used, with the pulse duration and gradient strength matched to excite the slice for which the shimming routine was carried out. The line width of the two coils could be reduced to 22 Hz and 21 Hz respectively when each coil is shimmed separately. For simultaneous shimming a line width of around 35 Hz is reliably achieved in both coils, with the lower coil always achieving a narrower line width than the upper. For the Bruker imaging probe the line width was reduced to 26 Hz from originally 57 Hz.

Conclusion

The shimming procedure gives good predictions for the obtainable ΔB_0 field. However, the line widths that can be obtained are still quite broad in terms of high resolution NMR, where sub-Hertz line widths are standard. It was tried to incorporate higher order shims but the resulting line widths did not decrease further. It can be seen from figure 4.5 that the field maps obtained from the small sample volume are quite noisy. The fact that additional shim components did not improve line widths was attributed to this. An additional problem is that the local ΔB_0 at each coil appears to be very different. The lower coil consistently obtained a narrower line width and higher signal intensity compared to the higher coil. This probably stems from the homebuilt nature of the probe and coils, which are not perfectly shaped. In the next section it will be shown that it was still possible to obtain fast 2D spectra form both coils simultaneously.

4.2.4 Fast 2D Experiments

In a one dimensional spectroscopic experiment the signal is collected as a function of a single time constant and sub-sequential Fourier transformation yields

the NMR spectrum. Additional information on nuclear connectivity can be ex-
tracted by adding another time constant to the experiment. The signal then de-
pends on two different variables $S(t_1, t_2)$ and Fourier transformation results in
a 2D spectrum. One effect of using additional dimensions is the reduction of
spectral overlap in samples containing many resonances. The general scheme
for a conventional 2D sequence is

excitation - evolution period t_1 - mixing - detection t_2.

The t_1 dimension is sampled by repetition of the experiment with different evo-
lution delays. The duration of the whole experiment depends on the number of
t_1 increments used. As the sample has to relax to thermal equilibrium between
each t_1 data collection step, this can be on a time scale of minutes and up to
hours. Depending on the design of the scheme different homo- or heteronuclear
correlations can be recorded. These can then be used for molecular structure
determination and characterisation [2].

A new approach, which dramatically increases the speed of the acquisition of
multidimensional spectroscopy experiments, has been introduced by L.Frydman
[48]. In his 'ultrafast' 2D sequences the necessity for experiment repetition
with different t_1 delays has been removed by spatially encoding the different
evolution times along the direction of the tube. This effectively divides the
sample into different sub-samples, where each evolves with a different t_1 delay.
Such partitioning can be achieved by applying a field gradient $G = \frac{d\omega}{dz}$ along the
sample tube, and then using frequency swept chirp pulses to subsequently excite
the different slices. In order to compensate for the de-phasing of the spins due to
the effect of the gradient this excitation element has to be followed by a reversed
gradient of the same duration and amplitude so only the internal frequencies of
the chemical shift and J-couplings are left to evolve. An excitation scheme of
this kind results in a helical winding of the magnetisation, with respect to the
rotating frame, where the pitch of the helix is given by $\exp iC\Omega_i(z - z_0)$. Ω_i

corresponds to the chemical shifts, z_0 is the reference position at the middle of the sample and $C = \frac{\Delta t_1}{z - z_0}$ is a constant relating the local evolution delay to the slice position.

These helices can be unwound by a read out gradient with echo times of the single resonances depending on how tightly wound the helix was, as well as its polarity. The t_2 dimension is scanned by using the echoplanar spectroscopic imaging (EPSI) technique developed by P. Mansfield [76]. During an oscillating gradient train the helices are un- and rewound and at the same time evolve under J-couplings and chemical shifts. This results in two complete data sets from the positive and negative gradients that can be individually processed. The acquired signal is given by [48]:

$$S(t_1(z), t_2) = \frac{\rho_0}{4\pi^2} \int_{\omega_1} \int_{\omega_2} d\omega_1 d\omega_2 I(\omega_1, \omega_2) \exp^{\iota C \omega_i (z - z_0)} \exp^{\iota \omega_2 t_2},$$

where ρ_0 is the distribution of the spins in the sample, which is assumed to be homogeneous and $\omega_{1,2}$ are the frequencies in the respective acquisition dimension. One striking feature of this kind of acquisition scheme is that Fourier transformation is only needed in the t_2 dimension because the timing of the echoes appearing under the acquisition gradient is dependent on the frequencies Ω_i, and so the spectrum in this dimension appears without Fourier transformation. In figure 4.7 an example of the raw data is given, which shows the chemical shift peaks appearing during the acquisition gradient train.

The acquisition time can be reduced to several tens of milliseconds, using this ultra-fast technique. Due to the single shot nature this approach readily lends itself to hyperpolarisation techniques such as dissolution DNP [49]. The fast 2D acquisition scheme is very versatile, depending on the mixing sequence it can be used for many different pulse programmes such as COSY, TOCSY, HSQC, HETCOR ([48]) and in principle others.

For the dual coil probehead the fast 2D COSY sequence was implemented, which gives information on homo-nuclear correlations. The conventional COSY
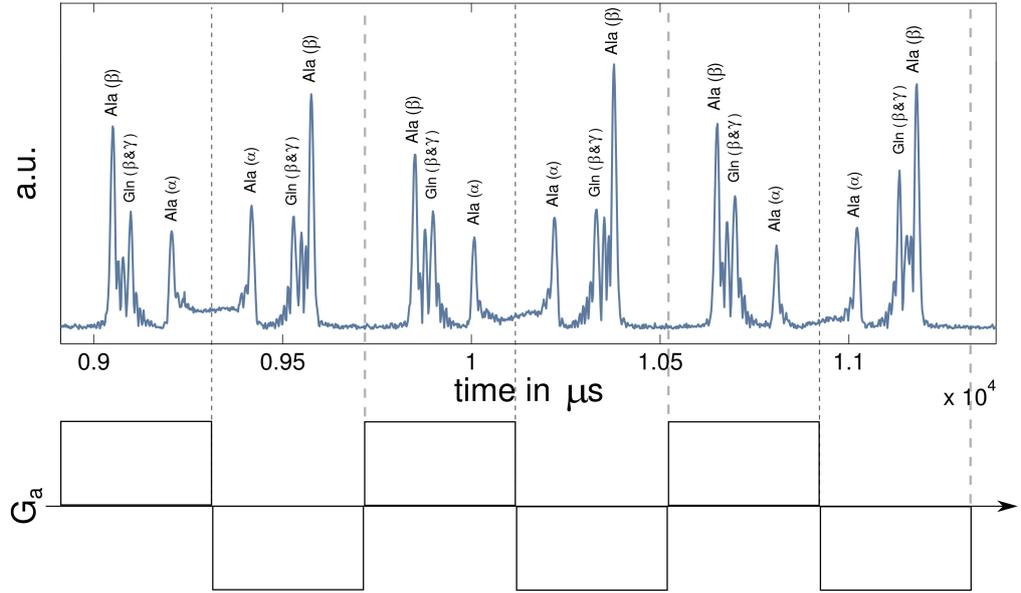
Figure 4.7: Demonstration of the fact that Fourier transformation is not required
in the direct dimension. Signal of sample containing 1M Alanine-Glutamine
Dipeptide dissolved in D_2O, acquired under a fast 2D acquisition gradient train
with $G_a = 2.45 \cdot 10^{-4} \frac{T}{mm}$. The raw data belong to the lower coil spectrum displayed in figure 4.9.

consists of two $\frac{\pi}{2}$ pulses spaced by a t_1 delay, which is incremented N times.
During the time t_1 the magnetisation undergoes modulations under the Hamiltonian $2\pi J \hat{I}_{1z} \hat{I}_{2z}$, with the coupling constant J. These modulations are probed and
projected out by the second hard pulse. The resulting 2D spectrum contains diagonal[2] and cross peaks which indicate correlation of the nuclei corresponding
to these resonances.

For the fast 2D COSY the first $\frac{\pi}{2}$ hard pulse is replaced by the phase sensitive
excitation scheme presented in [50] and a read out gradient train is placed after
the second $\frac{\pi}{2}$ pulse. The spectral width for both dimensions is

$$SW_1 = \frac{1}{T_a} \qquad SW_2 = \frac{\Delta O G_a T_a}{2 G_e \tau_p}, \qquad (4.2.2)$$

given that the excitation gradient and band width is matched to the sample

---

[2] which just state the obvious that all peaks are correlated with themselves

length. T_a is the duration of the acquisition gradient, ΔO the chirp excitation bandwidth, G_a the acquisition gradient strength, G_e the excitation gradient strength and τ_p the excitation pulse length.

The pulse sequence used is depicted in figure 4.8 for the simultaneous acquisition scheme. The chirp pulses, which are centered around $z = 0$ for a standard probe, have been shifted into the coil regions by a frequency offset. As for the dual coil probe the useful sample length is short compared to that of a standard high resolution probe the acquisition gradient had to be large ($\approx 0.25\frac{\text{mT}}{\text{m}}$) to be able to obtain sufficient spectral width. The EPI style acquisition gradient was cycled 64 times. Due to imperfections, the gradient reversals in the EPI acquisition train do not cancel each other out exactly, which causes the echoes to drift. This has to be accounted for by shearing the matrix in post-processing to ensure a straight line of echoes in the t_2 dimension is obtained prior to Fourier transformation. The small gradient before the echo train in figure 4.8 is used to shift the echoes to the center of the gradient lobes. It is also possible to use slightly different values for $+G_a$ and $-G_a$ to account for the drifting of the echoes during acquisition. Figure 4.9 shows the spectra acquired simultaneously from the dual coil probe for a sample of 1 M of an Alanine-Glutamine Dipeptide dissolved in D_2O. The acquisition time was 95 ms. It is obvious from figure 4.9 that the signal to noise ratio for the lower coil is better than for the upper, something that has already been noticed for the auto-shimming procedure. Some cross peaks are weakly or not resolved at all but it is shown that in principle it is possible to carry out fast 2D experiments on a multi-coil probehead.
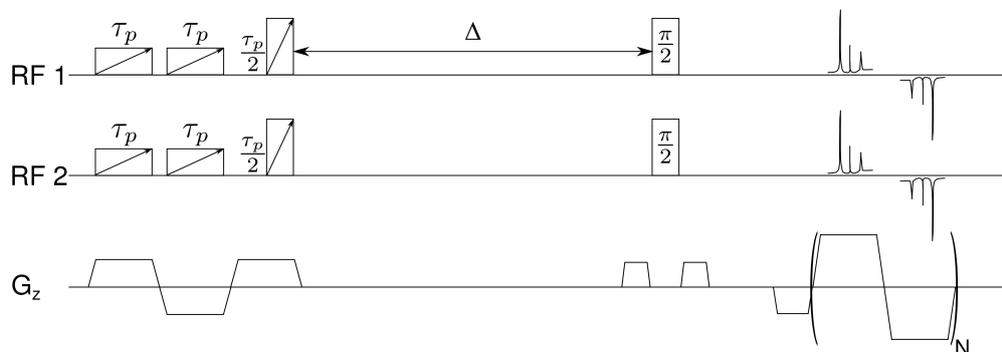
Figure 4.8: Fast 2D COSY sequences for the dual coil probe. The parameters used were $T_a = 141\mu s + 2x100\mu s$ ramping time, acquisition gradient $G_a = 2.45 \cdot 10^{-4} \frac{T}{mm}$, excitation gradient $0.2 \cdot 10^{-4} \frac{T}{mm}$, τ_p=5ms, ΔO=40kHz.
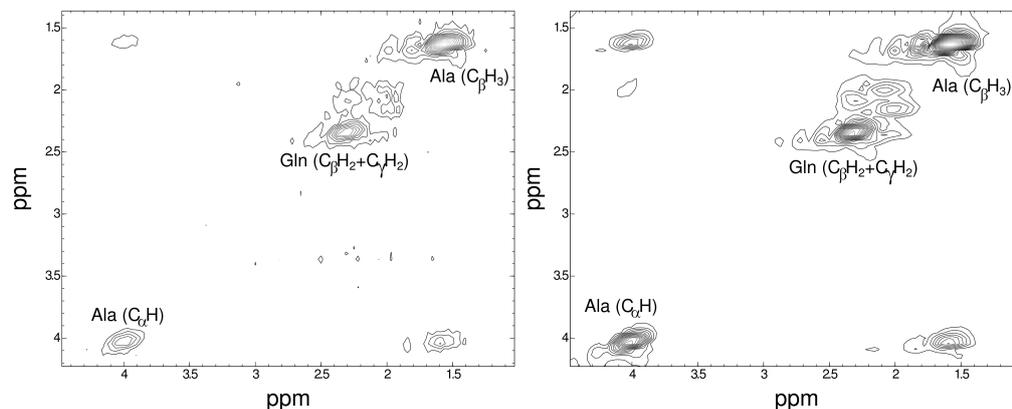
Figure 4.9: Phase sensitive fast 2D COSY Spectra of 1 M Alanine-Glutamine Dipeptide in D_2O acquired simultaneously on two channels within 90 ms. Left: upper coil, right: lower coil. Sample volume: 25 mL per coil.

Conclusions

It has been shown that it is possible to carry out fast 2D experiments using a dual
RF coil probe. It has also been found that there are limitations which leave room
for improvement. It should be possible to compensate for the low sensitivity of
the probe by using a hyperpolarised sample. The main problem is the fact that
shimming cannot be improved further with the field map based approach due to
the small sample volumes which make the ΔB_0 maps very noisy. An inherent
problem for the fast 2D spectroscopy is the small sample length which then leads
to the requirement of using strong acquisition gradients. This constitutes a large
demand on the hardware. One issue that was mostly eliminated was the cross
talk between the coils. The residual signal from one RF-coil is not visible in the
spectrum of the other RF-coil in fast 2D experiments. A possible explanation
is the inherent signal to noise limitation of fast 2D experiments due to the short
acquisition time.

4.3 Towards a six coil probe

Building on the experience gained from work with the dual coil probe head, a
first prototype of a probe comprising six RF-coils has been constructed in col-
laboration with BRUKER Biospin. The observe nucleus was chosen to be ^{13}C,
for its biological relevance as well as its low gyromagnetic ratio and natural
abundance. The latter two factors make it a nucleus that is normally difficult to
access for dynamical studies. Using the six RF-coil probe in conjunction with
DNP would make it possible to acquire data displaying dynamics in the sam-
ple. To aid the construction, simulations were carried out on Microwave Studio
from CST Studio Suite^{TM} 2010, which is based on finite element analysis. The
estimated inductance and capacitance of the coils as well as coupling parame-
ters and B_1 field distributions were obtained from these simulations. The coil

geometry was chosen to be an extension of the two coil probe, with three sad-
dle coils in a plane which is shielded from another plane with three coils by
a grounded copper sheet. A sketch of the coil geometry can bee seen in figure
4.10. Choosing this geometry means that the coils have to be shielded from each
other in-plane as well as through-plane. When choosing the coil dimensions one
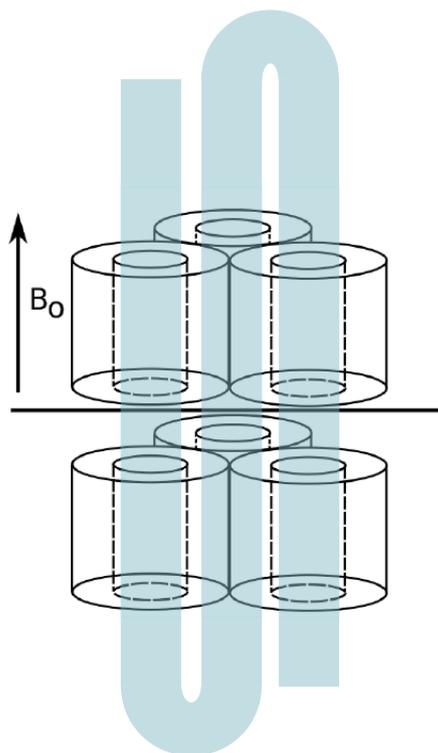
Figure 4.10: Sketch of six shielded and stacked saddle coils. The thick black
line in the middle symbolises the shield between the two stacks. The flow path
for the sample injection is schematically drawn in blue.

has to take into account that a smaller sample volume enables easier shimming,
whereas a larger sample volume gives a better SNR. As a compromise the coil
inner diameter (ID) was chosen to be 1.5 mm, which can accommodate a rigid
carrier tube to affix the RF coil as well as a sample tube of 0.9 mm diameter.
The sample tube itself cannot function as the carrier as it is flexible to make it
possible to maintain a single flow path through all coils. The length of the coil
was then chosen to be 5 mm.

4.3.1   Simulation results

CST simulation solvers

CST offers several solvers for the simulation of a resonant structure. The Eigenmode solver calculates a specified number of Eigenmodes of a given structure. In order to avoid an infinite number of over-modes, a user defined frequency range as well as the number of modes have to be set in the programme. In this case the used frequency range was [0 ,1000] MHz and and the number of modes was one. The resonance frequency and the corresponding magnetic and electric fields are then calculated for the user defined resonant structure. The Eigenmode solver is very fast but interpretation of its results is only straight forward if just one resonant structure is calculated. When more circuits are to be considered in the simulation, one can use the transient solver, where discrete ports of the different resonant structures can be driven separately. A Gaussian input signal is used, the parameters for the pulse are determined from the frequency range defined at the start of the simulation. In all simulations the frequency range of [0 ,1000] MHz was used. The circuit is tuned and matched with lumped elements, the parameters of which have to be determined by the user. This is done in an iterative process until the power absorption of the resonant circuit becomes maximal.

One coil

For the simulation of a single RF coil resonant circuit a saddle coil with the aforementioned dimensions was constructed in CST. The RF coil was then connected to a capacitor, that was also constructed in CST by the user. The capacitance was adjusted by modifying the size of the plates as well as the electric permeability constant of the material between the plates until the desired resonance frequency of 100 MHz was achieved. The capacitance will be discussed

in more detail below.

In order to test the effect of the necessary shielding around the coil on the B_1 field, four different simulations were carried out: one with a shield ID of 4 mm, then 5 mm, 6 mm and for reference one simulation without a shield. The calculated RF distribution was then masked by a tube of 1 mm diameter, which defined the region of the sample. The values for the magnetic energy inside this region as well as the magnetic field in the direction of the B_1 field are summarised in Table 4.1. The geometry of a coil without and with shield is shown in figure 4.11. The magnetic energy and field strength decrease with the smaller

(a) (b)
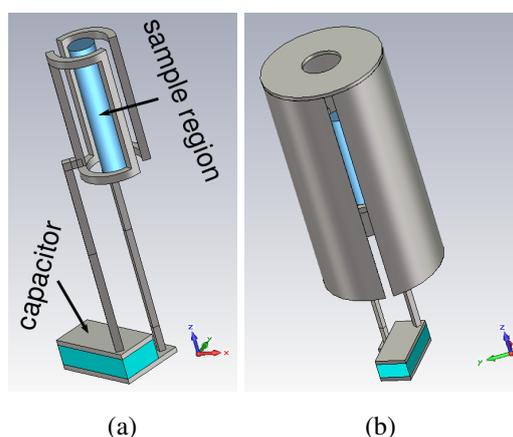
Figure 4.11: Geometry of simulation coil with and without shield of ID 6 mm. The blue cylinder inside the coils indicates the sample region for which the magnetic field strength and energy density was calculated.

shield diameter. The sample volume for which these values have been calculated extends from one end of the coil to the other in the z direction. As the B_1 field drops towards the ends of the coil, the standard deviations are quite large. The ratio of the standard deviation and the mean of the magnetic field strength for the three cases remains similar, at around 0.24, which means that the field does not become significantly more inhomogeneous for a smaller shield diameter. From figure 4.12, where the field profiles along the center of the coil in the

Table 4.1: Mean and standard deviation of the magnetic energy and field strength for the three different shield diameters.

	Magnetic Energy $\left[\frac{J}{m^3}\right]$		Magnetic field strength $\left[\frac{A}{m}\right]$		
ID [mm]	mean	standard deviation	mean	standard deviation	mean wrt. no shield
4	$7.7 \cdot 10^6$	$2.4 \cdot 10^6$	$3.3 \cdot 10^6$	$0.8 \cdot 10^6$	76%
5	$10.1 \cdot 10^6$	$2.9 \cdot 10^6$	$3.8 \cdot 10^6$	$0.9 \cdot 10^6$	88%
6	$11.2 \cdot 10^6$	$3.5 \cdot 10^6$	$4.0 \cdot 10^6$	$0.9 \cdot 10^6$	93%
no shield	$12.9 \cdot 10^6$	$4.1 \cdot 10^6$	$4.3 \cdot 10^6$	$0.9 \cdot 10^6$	100%

direction of the B_1 field are plotted, it is clear that the magnetic field strength
decreases with a smaller shield diameter.
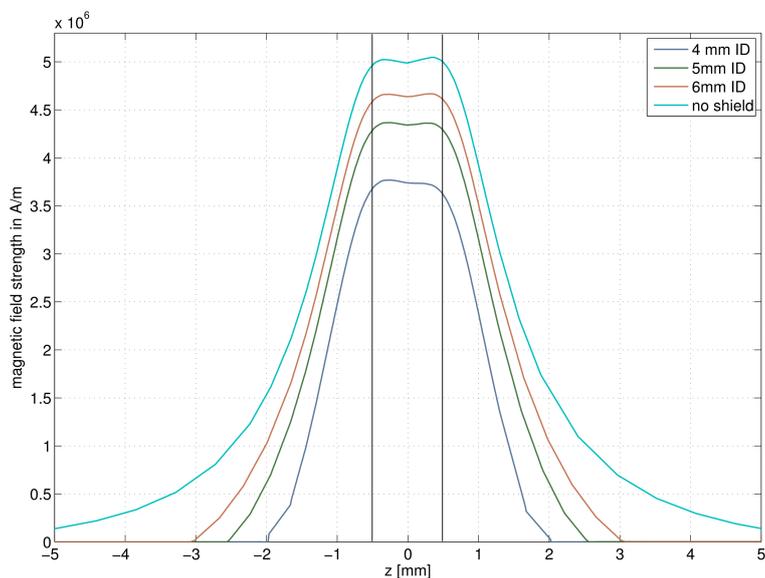
Figure 4.12: Magnetic field profiles along the coil B_1 field axis. The black lines
indicate the region of the sample. The legend denotes the shield inner diameter.

The resonance frequency of the circuit increases with decreasing shield diame-
ter. Starting of at 100.7 MHz for a coil with no shield the resonance frequency
increases to 116.7 MHz for the smallest shield diameter (see Table 4.2). This

Table 4.2: Change of the resonance frequency with shield diameter.

ID [mm]	-	6	5	4
ω [MHz]	100.7	104.1	106.6	116.7

has to be taken into account when selecting the capacitance of the resonant cir-
cuit. The 6 mm ID shield has been chosen for use in the probe as a compromise
between drop in B_1 field and spatial restrictions.

The capacitors needed to tune and match the circuit to 100 MHz were found
using the transient solver. This was done by changing the tuning and matching

capacitance iteratively until the best power absorption was achieved by the circuit . The values that were obtained in this way are C_t=121 pF and C_m=13pF. The coil inductance is then determined as 19 nH, which is a low value but not unexpected considering the small dimensions of the coil. The variable capacitors that will be used have a maximum value of 8 pF, this means that in order to obtain the required C_t of 121 pF a second capacitance of 113 pF has to be put in parallel. This results in a small tuning range, so the circuit has to be pre-tuned very close to the spectrometer base frequency. An alternative would be to wind the coil with two loops in order to increase the inductance. This would result in a decrease of the required tuning capacitance, hence increasing the tuning range. Winding a coil this way is mechanically very difficult to achieve due to the small dimensions of the coil and the brittleness of the susceptibility matched material. The exact geometry of the real probe will invariably differ slightly, therefore these calculations are used to get starting values for the construction.

Two coils in different planes

The coil configuration in the dual RF-coil probe was such that the B_1 field directions were perpendicular to one another to ensure decoupling. Due to the space constraints of the six-coil probe it was checked whether a parallel set-up, which would be easier to construct, would increase the coupling by a large amount. Two simulations were carried out, using the transient solver to drive one RF-circuit and detect the magnetic energy transferred to the other. The RF-circuits were positioned on either side of the centre shield (which took into account the hole for the sample tube) in a position that resulted in parallel or perpendicular B_1 field directions. The magnetic energy transfer from one sample region to the other was found to be one order of magnitude lower for a perpendicular arrangement than for a parallel setting ($3.9 \cdot 10^{-8} \frac{J}{m^3}$ instead of $2.29 \cdot 10^{-7} \frac{J}{m^3}$). This is not a dramatic decrease, indicating that the shield is responsible for most of the decoupling. Considering the spatial restrictions within the coil and the easier ar-

145

rangement of the coils in parallel, the gain in decoupling was deemed not to be
significant enough to justify the greater construction difficulty that would arise
from a perpendicular arrangement of the coils.

Six coils

The coupling for the complete six RF-coil configuration was calculated, includ-
ing the shields surrounding each RF-coil as well as a shield between the coil
planes which had 3 holes of 1 mm diameter to accommodate the sample tube.
For the simulation, one of the six RF-coils was driven with a Gaussian pulse and
the resulting magnetic energy density in the six sample regions was calculated.
For easier reference the coils where numbered, this is schematically shown in
figure 4.13. The transfer of energy from the active coil to the passive coil re-
gions is summarised in Table 4.3. These values are very small. From Table 4.3
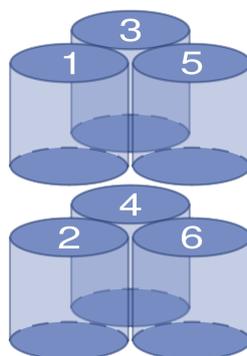
Figure 4.13: Numbering of the coils. The active coil is number one.

it becomes clear that the decoupling of coils in the same plane is slightly more
critical than the decoupling of coils in opposite planes. The fact that coil 4 has a
higher value for the induced magnetic energy than coils 5 and 6 stems from the
fact that it lies exactly opposite to coil 1. The finished design of the six RF-coil
probe is shown in figure 4.14.

Table 4.3: Transfer of magnetic energy from one coil to the others in % and
dB with respect to the energy in the first coil based on simulations using the
transient solver.

coil	2	3	4	5	6
transfer in %	$1.8e-7$	$4.2e-5$	$1.3e-12$	$4.2e-5$	$1.3e-12$
transfer in dB	-201	-146	-319	-146	-319
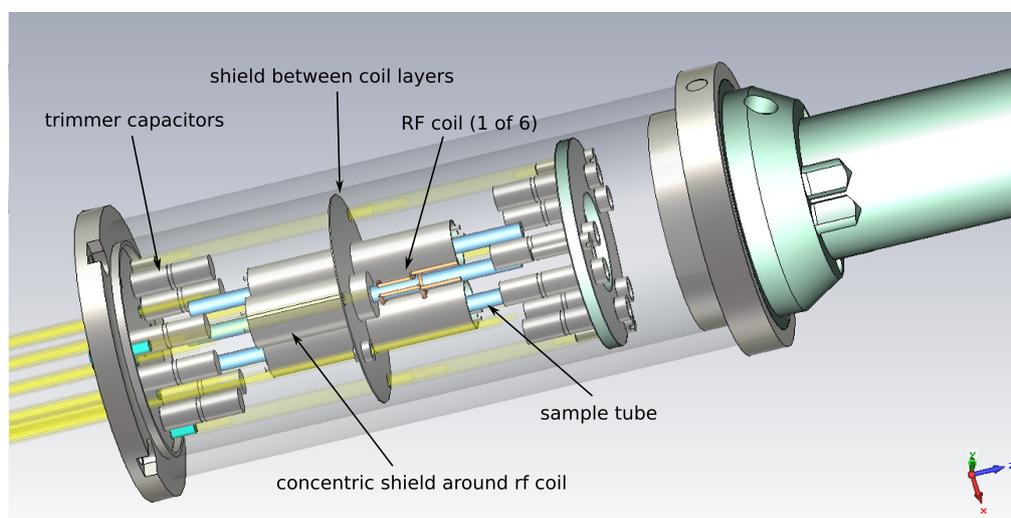
Figure 4.14: 6 coil probe configuration. Each RF-coil is shielded from the others
by a concentrical shield. Three coils are in one plane, which is separated from
the second plane by a shield with holes in order to allow the sample coil to
extend through both planes. One of shields around the coil has been removed
in order to allow a better view on the coil. The sample tubes are depicted in
blue, and are also cut for easier viewing. Design by T. Marquardsen at Bruker
BioSpin GmbH.

Additional simulation details

The quality of the simulations depends on the mesh that is defined: the smaller
the mesh cells, the more accurate the result, but the longer the simulation dura-

tion. In order to determine whether reasonable accuracy was achieved, the mesh
cell size was decreased iteratively to check whether the resonance frequency of
the circuit would change. When a change of less than 0.5 MHz was registered,
the meshing was deemed to produce sufficiently accurate results. The smallest
mesh step needed in order to resolve the coil structure was 0.02 mm, although
not all cells were the same size. CST determines a non-uniform mesh that al-
lows to speed up the simulation by finding the parts of the structure that are
uniform over a larger region and increasing the mesh cell size there. The energy
of the entire system is normalised to 1, so to test if the simulation has converged,
the integral of the energy was calculated. In all transient solver simulations the
integral added up to a value of around 1.14, which means that the results of the
simulations are accurate within a range of 14%. For the Eigenmode solver sim-
ulations the integral added up to 1.05, so here a slightly higher accuracy can be
assumed. As it was not the intention to find exact values but to make qualitative
statements and comparisons between simulations that would help to modify the
existing probe design, this accuracy was deemed sufficient[3].

Summary

In the original design the shield diameter around the coil was 4 mm. From the
simulations it was seen that this would reduce the B_1 field strength by 24%, so
as a compromise between space restrictions and B_1 field strength a 6 mm ID
was chosen. In the simulations the tuning capacitance C_t, needed to obtain the
desired 100 MHz resonance frequency, was found to be 121 pF. In the real probe
the capacitances that were used ranged between 120 pF and 138 pF, thus the
simulated value was of the same order of magnitude. The matching capacitance

---

[3]Deviations of the constructed probe from the simulated circuit will probably change the
values for capacitance and inductance. Additionally there will probably be stray capacitance
and inductance present in the probe that is not considered in the simulations, hence there is little
point to try and make the simulation very accurate.

in the simulations was 13 pF, whereas in the real probe the values used were
between 10 and 20 pF. Also here the correct order of magnitude was predicted
by the simulations. It was found that the coupling from one coil to another on the
other side of the shield in the xy plane is very small, whereas more care has to be
taken to decouple the three coils in the same plane. Judging from this ,it might
be beneficial to extend the shield around each coil all the way up to the plane
that mounts the capacitors in order to avoid coupling of the leads of the coils.
Alternatively one could consider to separate the coils by three compartments
arranged in an arrangement similar to a pie sliced in three parts.

4.3.2 Initial performance results

Figure 4.15 shows the probe before it was sealed with a protective cover. The
shielding around the coils is visible, as well as between them. The capacitors are
located on the platforms below and above the coils. All six channels were pre-
tuned to the same frequency using a network analyser. The matching efficiency
was very similar for all coils, implying a symmetric set-up of the electronics.
The probe was loaded with ^{13}C labelled methanol for pulse power calibration.
The $\frac{\pi}{2}$ pulse durations for each coil are summarised in Table 4.4. The values
are very similar, indicating that the efficiency of power transfer is on the same
order for each coil. The first coil is fitted with an additional resonant circuit and

Table 4.4: $\frac{\pi}{2}$-pulse duration in μs at an input power of 10 W.

1	2	3	4	5	6
11.5	11	10	10	10.5	9.0

double tuned to the ^{13}C and deuterium frequencies. The deuterium signal can be
used by the lock channel to assist in shimming the probehead. The ^{13}C channel
belonging to the double tuned RF coil is fitted with a high frequency filter, which
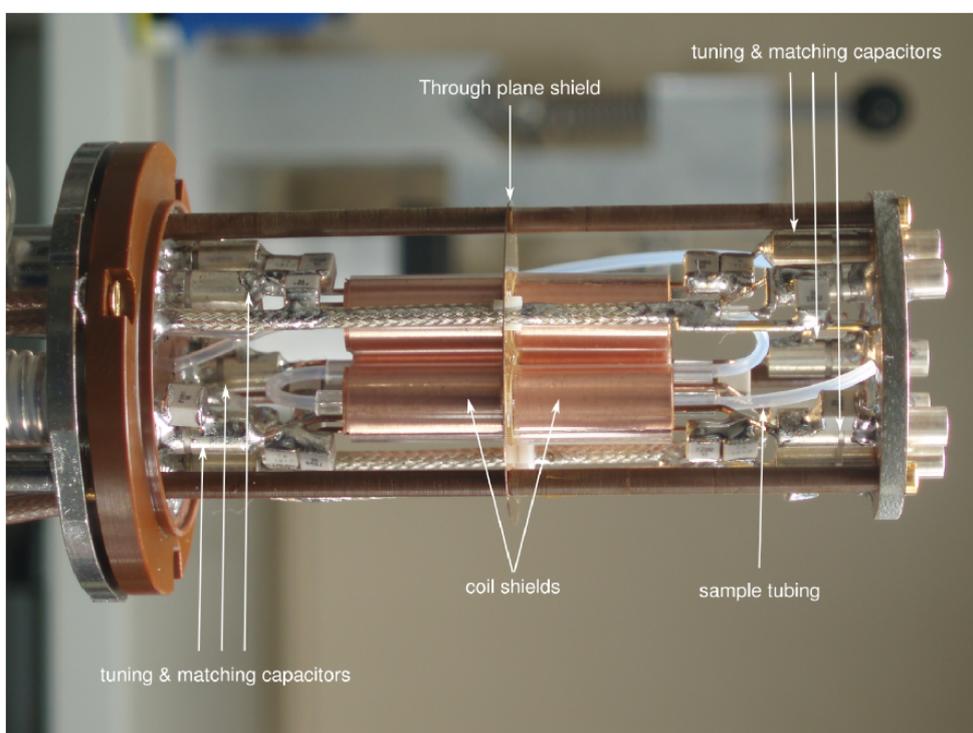
Figure 4.15: Probe with six RF-coils. Designed and built by T. Marquardsen at Bruker BioSpin GmbH.

could be responsible for the slightly longer $\frac{\pi}{2}$ pulse duration compared to the other coils.

It was found that when the probe is shimmed solely to the deuterium spectrum of the first coil, the quality of the remaining five coils is severely degraded. Hence the attempt was made to shim on the ^{13}C spectrum of all coils, which is very time consuming due to the low SNR of the carbon signal. The line width of the spectrum of the well shimmed first coil is 2.5 Hz. The best compromise in signal strength found to date resulted in line widths ranging from 18 to 55 Hz. There is room for improvement if additional effort is made to find a compromise in the shim settings. The spectra of all coils are depicted in figure 4.16, both for simultaneous excitation on all coils as well as single excitation on each coil separately. Small differences in the spectra for either case are apparent, which indicate a certain amount of coupling. The coupling determined on the network analyser was determined to be approximately -25 dB for the coils in one plane and -35 dB through-plane, which is significantly larger than what was expected from the simulations. The simulations took into account the probe-head region including the tuning circuit but the capacitors were positioned closer to the coils than they are in the real probe. This means that the part of the leads that was unshielded was shorter in the simulation than in the actual probe, which probably leads to an underestimation of the coupling. In hindsight it would have been better to extend the coil leads out further in the simulations. As was seen in the two-coil probe project, the NMR spectra are a great deal more sensitive to coupling than the network analyser, hence in order to test signal transfer between the coils an experiment was devised where a $\frac{\pi}{2}$ was applied to one coil and the signal was recorded on all RF-coils. The signals were integrated and normalised to the integral of the active coil. The results are summarised in Table 4.5. The signal appearing on the channels where no excitation was applied was found to be substantial (up to 40% signal transfer) in some cases. Table 4.5 confirms the simulation results that the coils in one plane couple strongest.
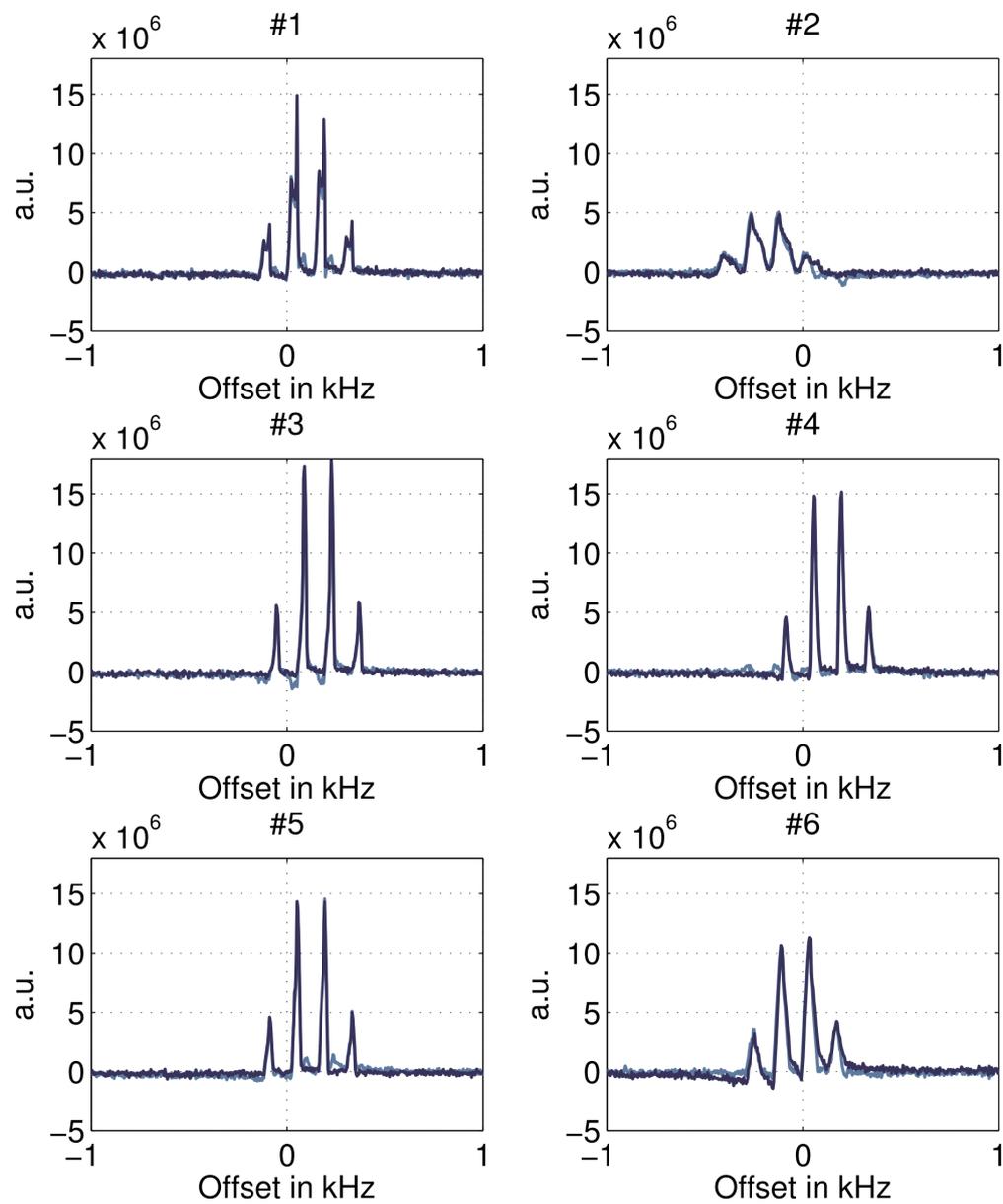
Figure 4.16: Spectrum of ^{13}C-methanol from all coils acquired separately in single excitations (dark blue line) and at the same time (light blue line). Spectra acquired with four averages.

The through plane coupling of coil three and four stand out particularly, on all other coils through plane coupling remains relatively small. The values given in Table 4.5 lack the reciprocity which one would expect if signal spillage from one coil to the other was the main reason for signal appearing on the non-active coils. The shimming is not the same for each coil, and so the signal intensities vary but the normalisation of the integral should have accounted for this if the coupling was of purely inductive origin. As the shimming is different for each

Table 4.5: Integral of signal appearance in other coils after excitation on one coil in % of spectrum integral of excitation coil. The active coil is indicated above the Table.

	active coil:	1	2	3	4	5	6
	1	100	6	15	7	21	1
	2	0	100	0	9	2	13
Observe coils	3	18	10	100	11	22	2
	4	10	28	11	100	5	14
	5	24	3	17	4	100	3
	6	6	40	2	30	8	100

coil, most spectra have a different resonance offset. This can help to pinpoint the origin of the signal appearance on the non-active coils. In figure 4.17 the results for the experiment described above for the case when an excitation pulse is applied on coil 3 and 4 are shown. It can be seen in the figure, that resonances also appear outside the active coil peaks, particularly for coil number four being active, which indicates that direct excitation of the sample in the passive coils due to power transfer through the leads might take place. To test if this was the case, a $45°$ pulse was applied to one coil, and a $180°$ pulse on another. This way, the magnetisation of the sample in the second coil should be inverted and not appear. If pulse power transfer takes place, the flip angle of the first coil should
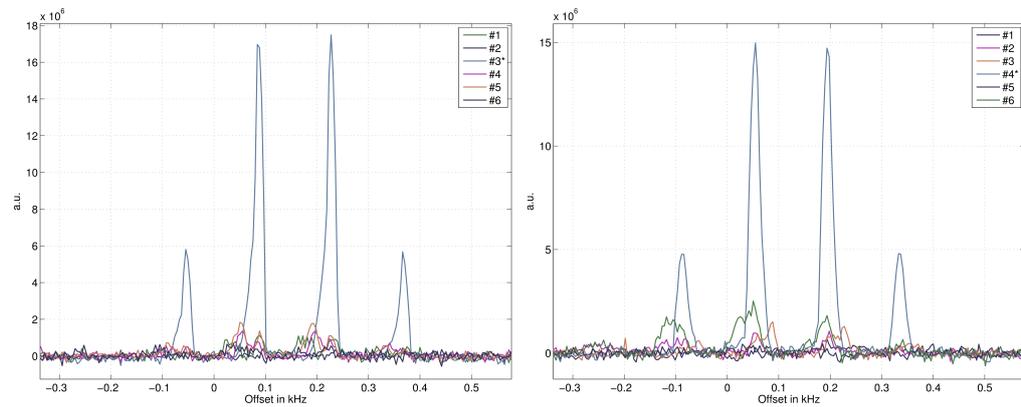
Figure 4.17: Comparison of signal transfers for active coil number 3 (left) and 4(right). The active coil is marked with an asterisk.

be increased with respect to no pulse being applied to the second coil. The same can be repeated using a $180°$ pulse that is phase shifted by $180°$. In this case the flip angle in the first coil should be reduced with respect to the experiment where no pulse is applied to the second coil. The result of the experiment for three and four is shown in figure 4.18. The ratio of the intensities $\frac{I_{in}}{I_{fin}}$ is related
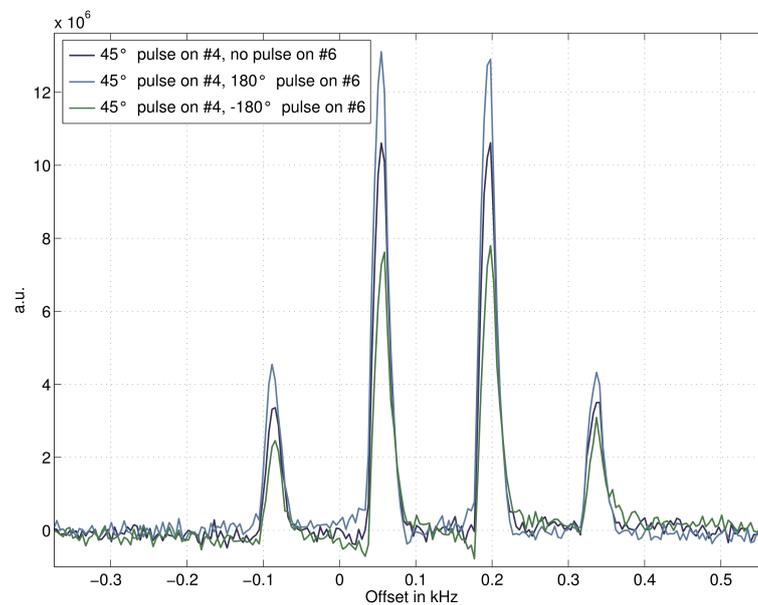
Figure 4.18: Modification of the $45°$ pulse on coil number four by a $180°$ pulse on coil number six.

to the flip angles β by:

$$\frac{I_{in}}{I_{fin}} = \frac{\sin\beta_{in}}{\sin\beta_{fin}}.$$

For the experiment displayed in figure 4.18 the flip angle was increased by 16.7°
for the in-phase 180° pulse and decreased by 14.3° for the anti-phase 180° pulse.
Using the B_1 field obtained from the pulse calibration, one gets an additional
$\delta\omega_1$ of 12.5 kHz. This translates into a power transfer of 8% of the 10W pulse
that is applied to the second coil. Combined with the fact that the initial signal
is stronger on coil four due to the better shimming, this could explain the larger
signal transfer from coil six to four than vice versa (see Table 4.5): The signal
appearance on the passive coil is a superposition of signal spillage from the
active coil and a small pulse being applied to the passive coil as a result of pulse
power transfer. As the shimming is better for the fourth coil, the signal that is
a result of the applied small pulse is larger than for coil six in the equivalent
experiment. The same experiment has also been carried out for coil 3 and 4 as
well as 3 and 4. The power transfer from 3 to 5 was found to be only 2%, the
transfer for coil 3 to 4 was 14%.

The coupling is quite substantial at the moment, hence it is not advisable to
perform sequential acquisition experiments, where one coil is applying a pulse
whilst another is still acquiring data, as this could damage the receiver.

The signal transfer from one RF-coil to another could stem from the fact that
the shielding around each coil does not extend completely over the leads going
from the RF-coil to the capacitors, as can be seen from figure 4.15. Another
possibility is coupling via the capacitors of the coils in the same plane as these
are in close vicinity to one another. Both of these origins of coupling could be
alleviated by adding shielding.

4.3.3   Summary

A probe with six RF coils, tuned to the same resonance frequency, has been presented. It was shown from the pulse calibrations that the efficiency of all the coils is largely the same. As expected, shimming proved to be difficult but a compromise that enabled to get a spectrum on all six coils has been found. Additional effort can be made to improve the shimming but in order to test the coupling between the coils the shimming was sufficient. The automatic shimming procedure presented for the two-coil probe is not applicable due to the different observe nucleus, which results in a much lower SNR, but a different strategy could be devised, which uses the information of the different resonance offsets of each coil.

The coupling was found to be quite large between certain coils. In-plane coupling was found to be the most dominant, which was expected from the simulation results. The coupling expected from the simulations was much lower than that found in reality. This could be due to the fact that the leads in the simulations did not extend far enough out of the shields around the RF coils.

Investigations into the nature of the coupling has found a superposition of two mechanisms: firstly the appearance of signal of a different coil in the first coil, secondly the transfer of RF power from one coil to another, resulting in the application of a small RF pulse in an otherwise passive coil. The coupling has to be reduced before it is possible to carry out sequential acquisition experiments, where one coil is still acquiring data whilst another is pulsing, in order to prevent receiver damage.

4.4   Conclusions

It was shown that the concept of a probe with multiple coils tuned to the same RF frequency is possible. As one might expect, great care has to be taken to

minimise coupling. Once this is achieved the six-coil probe could be used with hyper-polarised samples, acquiring data at different time points. One step to improve the spectra and experiment flexibility further is to incorporate double tuning to ^{13}C and ^{13}H for the six coil probe. Then polarisation transfer schemes such as HSQC or HMBC could be used, either in fast 2D fashion or in the small flip angle style used by C.Hilty's group [77].

CHAPTER 5

Outlook

Since the start of the work presented by the author, DNP has been transformed from being an exotic topic to a focus point of major NMR conferences. This was mainly driven by recent advances in hardware development, which led to the development of commercially available polarisers. New opportunities in applied research, mainly in the areas of chemistry and biomedicine, have since opened up. Despite DNP being widely used, the underlying mechanisms are poorly described by a quantitative theory. As was mentioned at the start, for true insight to be gained from theory, the models used have to be based on quantum mechanics with its unfavourable scaling in propagator size. In this thesis methods were introduced which allow to greatly reduce the size of the matrix dimensions needed to describe the system dynamics. The latest development of a projection method has allowed the scaling to be reduced to N from initially 4^N.

Thus far the projection method has been devised for the solid effect, the extension to incorporate more electrons remains to be made in future work. In principle there is no limitation on the inclusion of more electrons, as long as the largest spin-spin interaction remains small compared to the nuclear Larmor frequency.

Currently the number of spins accessible in simulations is on the order of 10^4,

which is still much smaller than Avogadro's number. In order to make comparisons of the results of the simulations to a real experiment, DNP could be performed on crystals, allowing periodic boundary conditions to be introduced in the simulation.

With the number of spins that can now be simulated, it should be possible to make comparisons to thermodynamical models of DNP. Investigation into the diffusion of spin polarisation through space is now also possible.

In the last chapter a novel way of data acquisition for NMR has been introduced. It was seen that the principle of using several RF coils at different locations of the sample is feasible. Practical limitations were thus far the coupling between the coils as well shimming. A second generation probe with 6 RF coils is currently being build by BRUKER, in which the coils including all leads of the coil circuit have been isolated carefully by a compartmented design. The materials used in this probe are highly adapted to high resolution NMR and should introduce only small susceptibility effects, allowing for easier shimming.

With this probe in place, DNP experiments with molecules exhibiting dynamics can be carried out using the fast shuttling spectrometer introduced in [46]. One additional modification of the multi-coil probe could be the incorporation of double tuning, to allow polarisation transfer schemes to be carried out and to acquire on the more sensitive ^{13}C nucleus.

Irreducible spherical tensor operators

The irreducible tensor (IST) operators can be constructed from the basis operators $\{\hat{E}, \hat{I}_z, \hat{I}_-, \hat{I}_+\}$. They are derived from the spherical harmonics which are the eigenfunctions of the angular momentum operators [5]. As a reminder, the angular momentum operators are

$$\hat{L}_x = -i\hbar(y\,p_z - z\,p_y) \quad \hat{L}_y = -i\hbar(z\,p_x - x\,p_z) \quad \hat{L}_z = -i\hbar(x\,p_y - y\,p_x),$$

which obey the well known commutation relation

$$\left[\hat{L}_i, \hat{L}_j\right] = -i\varepsilon_{ijk}\hat{L}_k, \quad \text{where } i, j, k \in [x, y, z].$$

The total angular momentum operator $\hat{L}^2 = \hat{L}_x^2 + \hat{L}_y^2 + \hat{L}_z^2$ obeys the commutation relation $\left[\hat{L}^2, L_i\right] = 0$, which means that $\hat{L}^2$ shares its eigenfunctions with $\hat{L}_i$. It is helpful to use the notation $|l, m\rangle$ for these shared eigenfunctions. The eigenvalues of $\hat{L}_z$ and $\hat{L}^2$ are:

$$\hat{L}^2|l, m\rangle = l(l+1)|l, m\rangle \text{ and } \hat{L}_z|l, m\rangle = m|l, m\rangle,$$

It turns out that the spherical harmonics functions $Y_{lm}(\theta, \phi)$ are the eigenfunctions $|l, m\rangle$. The irreducible tensor operators $\hat{T}_{lm}$ associated with $Y_{lm}(\theta, \phi)$ are

obtained by transforming $Y_{lm}(\theta, \phi)$ into Cartesian coordinates $Y_{lm}(x, y, z)$ and re-placing the terms with the corresponding angular momentum operator [7]. For example:

$$Y_{1-1}(\theta, \phi) = \sqrt{\frac{3}{8\pi}}\, e^{-i\phi} \sin\theta \rightarrow Y_{1-1}(x, y, z) = \sqrt{\frac{3}{8\pi}}\frac{x + iy}{r} \rightarrow \hat{T}_{1-1} = \frac{1}{\sqrt{2}}\hat{I}_-$$

The single spin IST are thus [2]:

$$\hat{T}^{(1)}_{00} = \hat{E},$$

$$\hat{T}^{(1)}_{1-1} = \frac{1}{\sqrt{2}}\hat{I}_-, \quad \hat{T}^{(1)}_{01} = \hat{I}_z, \quad \hat{T}^{(1)}_{11} = \frac{1}{\sqrt{2}}\hat{I}_+$$

and the two spin IST operators are:

$$\hat{T}^{(2)}_{20} = \sqrt{\frac{2}{3}}\left[\hat{I}_{1z}\hat{I}_{2z} - \frac{1}{4}\left(\hat{I}_{1-}\hat{I}_{2+} + \hat{I}_{1+}\hat{I}_{2-}\right)\right]$$

$$\hat{T}^{(2)}_{2\pm1} = \mp\frac{1}{2}\left(\hat{I}_{1z}\hat{I}_{2\pm} + \hat{I}_{1\pm}\hat{I}_{2z}\right)$$

$$\hat{T}^{(2)}_{2\pm2} = \frac{1}{2}\hat{I}_{1\pm}\hat{I}_{2\pm}$$

Higher order terms are not needed as all Hamiltonians encountered in this thesis are bilinear at maximum. The advantage of using IST operators is that their ranks do not mix under rotation, one IST simply gets transformed into a linear combination of IST's of the same rank:

$$\hat{\hat{R}}(\alpha, \beta, \gamma)\hat{T}_{lm} = \sum_{m'} \hat{T}_{lm}\mathscr{D}^l_{m'm}(\alpha, \beta, \gamma),$$

where $\hat{\hat{R}}(\alpha, \beta, \gamma)$ is a general rotation around the Euler angles and $\mathscr{D}^l_{m'm}(\alpha, \beta, \gamma)$ are the Wigner rotation matrices.

Krylov Bogoliubov averaging method

The Krylov Bogoliubov averaging method can be used on functions that can be expressed as $\frac{\mathrm{d}x}{\mathrm{d}t} = \varepsilon X(t,x)$, where ε is a small parameter [67]. The equation of motion was brought into this form in section 3.4.1:

$$\frac{\partial}{\partial \tau}|\hat{\rho}(\tau)\rangle = \varepsilon \left[\hat{\hat{A}}(\tau)\hat{\rho}(\tau) + \hat{\hat{y}}\right],$$

with (B.0.1)

$$\hat{\hat{A}}(\tau) = \hat{\hat{h}}_0 + e^{-i\tau}\hat{\hat{h}}_+ + e^{i\tau}\hat{\hat{h}}_- \quad \text{and} \quad \hat{\hat{y}} = \hat{\hat{\gamma}}|\hat{\rho}_{th}\rangle.$$

Equation (B.0.1) can then be rewritten using time independent coefficients if a change of variables of $|\hat{\rho}\rangle$ is performed:

$$|\hat{\rho}(\tau)\rangle = \left[1 + \varepsilon\hat{\hat{C}}(\varepsilon,\tau)\right]|\hat{\rho}'\rangle + \varepsilon\hat{\hat{c}}(\varepsilon,\tau)$$

using $|\hat{\rho}'(\tau)\rangle$ for which (B.0.2)

$$\frac{\partial}{\partial \tau}|\hat{\rho}'\rangle = \varepsilon \left[\hat{\hat{B}}(\varepsilon)|\hat{\rho}'\rangle + \hat{\hat{b}}(\varepsilon)\right].$$

The coefficients $\hat{\hat{C}}(\varepsilon,\tau)$, $\hat{\hat{c}}(\varepsilon,\tau)$, $\hat{\hat{B}}(\varepsilon)$ and $\hat{\hat{b}}(\varepsilon)$ have to be determined. To achieve this, first the time derivative of $|\hat{\rho}\rangle$ in (B.0.2) is taken and the expression

for $\frac{\partial}{\partial \tau}|\hat{\rho}'\rangle$, also from (B.0.2), plugged in:

$$
\frac{\partial}{\partial \tau}|\hat{\rho}(\tau)\rangle =
$$
$$
\varepsilon \frac{\partial}{\partial \tau}\hat{\hat{C}}(\varepsilon, \tau)|\hat{\rho}'\rangle + \left[1 + \varepsilon \hat{\hat{C}}(\varepsilon, \tau)\right] \frac{\partial}{\partial \tau}|\hat{\rho}'\rangle + \varepsilon \frac{\partial}{\partial \tau}\hat{c}(\varepsilon, \tau) =
$$
$$
\varepsilon \frac{\partial}{\partial \tau}\hat{\hat{C}}(\varepsilon, \tau)|\hat{\rho}'\rangle + \left[1 + \varepsilon \hat{\hat{C}}(\varepsilon, \tau)\right] \varepsilon \left[(\varepsilon)|\hat{\rho}'\rangle + \hat{b}(\varepsilon)\right] + \varepsilon \hat{\hat{B}} \frac{\partial}{\partial \tau}\hat{c}(\varepsilon, \tau).
$$

This can be equated to the original expression of $\frac{\partial}{\partial \tau}|\hat{\rho}(\tau)\rangle$ in (B.0.1):

$$
\varepsilon \frac{\partial}{\partial \tau}\hat{\hat{C}}(\varepsilon, \tau)|\hat{\rho}'\rangle + \left[1 + \varepsilon \hat{\hat{C}}(\varepsilon, \tau)\right] \varepsilon \left[\hat{\hat{B}}(\varepsilon)|\hat{\rho}'\rangle + \hat{b}(\varepsilon)\right] + \varepsilon \frac{\partial}{\partial \tau}\hat{c}(\varepsilon, \tau) =
$$
$$
\varepsilon \left[\hat{\hat{A}}(\tau)|\hat{\rho}(\tau)\rangle + \hat{y}\right].
$$

Using B.0.2 one gets:

$$
\varepsilon \frac{\partial}{\partial \tau}\hat{\hat{C}}(\varepsilon, \tau)|\hat{\rho}'\rangle + \left[1 + \varepsilon \hat{\hat{C}}(\varepsilon, \tau)\right] \varepsilon \left[\hat{\hat{B}}(\varepsilon)|\hat{\rho}'\rangle + \hat{b}(\varepsilon)\right] + \varepsilon \frac{\partial}{\partial \tau}\hat{c}(\varepsilon, \tau) =
$$
$$
\varepsilon \hat{\hat{A}}(\tau) \left[1 + \varepsilon \hat{\hat{C}}(\varepsilon, \tau)\right] |\hat{\rho}'\rangle + \varepsilon^2 \hat{\hat{A}}(\tau)\hat{c}(\varepsilon, \tau) + \varepsilon \hat{y}.
$$

One can split this into two independent equations, one with terms containing $|\hat{\rho}'\rangle$ and one with terms not containing $|\hat{\rho}'\rangle$

$$
\frac{\partial}{\partial \tau}\hat{\hat{C}}(\varepsilon, \tau) = \hat{\hat{A}}(\tau) \left[1 + \varepsilon \hat{\hat{C}}(\varepsilon, \tau)\right] - \left[1 + \varepsilon \hat{\hat{C}}(\varepsilon, \tau)\right] \hat{\hat{B}}(\varepsilon)
$$
$$
\frac{\partial}{\partial \tau}\hat{c}(\varepsilon, \tau) = \varepsilon \hat{\hat{A}}(\tau)\hat{c}(\varepsilon, \tau) + \hat{y} - \left[1 + \varepsilon \hat{\hat{C}}(\varepsilon, \tau)\right] \hat{b}(\varepsilon)
$$
(B.0.3)

The unknown coefficients can be expanded in terms of ε:

$$
\hat{\hat{C}}(\varepsilon, \tau) = \sum_{k=0}^{\infty} \varepsilon^k \hat{\hat{C}}_k(\tau), \quad \hat{\hat{B}}(\varepsilon) = \sum_{k=0}^{\infty} \varepsilon^k \hat{\hat{B}}_k,
$$
$$
\hat{c}(\varepsilon, \tau) = \sum_{k=0}^{\infty} \varepsilon^k \hat{c}_k(\tau), \quad \hat{b}(\varepsilon) = \sum_{k=0}^{\infty} \varepsilon^k \hat{b}_k
$$

and inserted into the equations B.0.3:

$$
\frac{\partial}{\partial \tau} \left[\hat{\hat{C}}_0(\tau) + \varepsilon \hat{\hat{C}}_1(\tau) + \varepsilon^2 \hat{\hat{C}}_2(\tau) + \ldots\right] =
$$
$$
\hat{\hat{A}}(\tau) \left[1 + \varepsilon \hat{\hat{C}}_0(\tau) + \varepsilon^2 \hat{\hat{C}}_1(\tau) + \ldots\right] - \left[1 + \varepsilon \hat{\hat{C}}_0(\tau) + \varepsilon^2 \hat{\hat{C}}_1(\tau) + \ldots\right] \left[\hat{\hat{B}}_0 + \varepsilon \hat{\hat{B}}_1 + \ldots\right]
$$
$$
\frac{\partial}{\partial \tau} \left[\hat{c}_0(\tau) + \varepsilon \hat{c}_1(\tau) + \varepsilon^2 \hat{c}_2(\varepsilon) + \ldots\right] =
$$
$$
\varepsilon \hat{\hat{A}}(\tau) \left[\hat{c}_0(\tau) + \varepsilon \hat{c}_1(\tau) + \ldots\right] + \hat{y} - \left[1 + \varepsilon \hat{\hat{C}}_0(\tau) + \varepsilon^2 \hat{\hat{C}}_1(\tau) + \ldots\right] \left[\hat{b}_0 + \varepsilon \hat{b}_1 + \ldots\right]
$$

Ordering into equations of the same order of ε gives:

$$\frac{\partial}{\partial \tau}\hat{\hat{C}}_0(\tau) = \hat{\hat{A}}(\tau) - \hat{\hat{B}}_0$$

$$\frac{\partial}{\partial \tau}\hat{\hat{C}}_1(\tau) = \hat{\hat{A}}(\tau)\hat{\hat{C}}_0(\tau) - \hat{\hat{B}}_1 - \hat{\hat{C}}_0(\tau)\hat{\hat{B}}_0$$

$$\ldots$$

$$\frac{\partial}{\partial \tau}\hat{\hat{C}}_{k+1}(\tau) = \hat{\hat{A}}(\tau)\hat{\hat{C}}_k(\tau) - \sum_{j=0}^{k}\hat{\hat{C}}_{k-j}(\tau)\hat{\hat{B}}_j$$

and

$$\frac{\partial}{\partial \tau}\hat{\hat{c}}_0(\tau) = \hat{\hat{y}} - \hat{\hat{b}}_0$$

$$\frac{\partial}{\partial \tau}\hat{\hat{c}}_1(\tau) = \hat{\hat{A}}(\tau)\hat{\hat{C}}_0(\tau) - \hat{\hat{B}}_1 - \hat{\hat{C}}_0(\tau)\hat{\hat{B}}_0$$

$$\ldots$$

$$\frac{\partial}{\partial \tau}\hat{\hat{c}}_{k+1}(\tau) = \hat{\hat{A}}(\tau)\hat{\hat{c}}_k(\tau) - \sum_{j=0}^{k}\hat{\hat{C}}_{k-j}(\tau)\hat{\hat{b}}_j.$$

The coefficients $\hat{\hat{C}}_k(\tau)$ and $\hat{\hat{c}}_k(\tau)$ are periodic in time. Hence the time average as well as the time average of the derivative of these coefficients has to be zero. As an example, for k=0:

$$\hat{\hat{B}}_0 = \overline{\hat{\hat{A}}(\tau)} = \hat{\hat{h}}_0$$

and

$$C_0(\tau) = \int \left(\hat{\hat{A}}(\tau) - \overline{A(\tau)}\right) d\tau =$$
$$\int \left(\hat{\hat{h}}_0 + e^{-i\tau}\hat{\hat{h}}_+ + e^{i\tau}\hat{\hat{h}}_- - \hat{\hat{h}}_0\right) d\tau = i\left(e^{-i\tau}\hat{\hat{h}}_+ - e^{i\tau}\hat{\hat{h}}_-\right)$$

In general, the coefficients can be found with:

$$\hat{\hat{B}}_{k+1} = \overline{\hat{\hat{A}}(\tau)\hat{\hat{C}}_k}$$

$$\hat{\hat{b}}_{k+1} = \overline{\hat{\hat{A}}(\tau)\hat{\hat{c}}_k}$$

$$\hat{\hat{C}}_{k+1} = \int \left[\hat{\hat{A}}(\tau)\hat{\hat{C}}_k - \hat{\hat{B}}_{k+1} - \sum_{j=0}^{k}\hat{\hat{C}}_{k-j}\hat{\hat{B}}_j\right] d\tau$$

$$\hat{\hat{c}}_{k+1} = \int \left[\hat{\hat{A}}(\tau)\hat{\hat{c}}_k - \hat{\hat{b}}_{k+1} - \sum_{j=0}^{k}\hat{\hat{c}}_{k-j}\hat{\hat{b}}_j\right] d\tau$$

The first three steps result in the following coefficiens

$$\hat{\hat{B}}_0 = \hat{\hat{l}}_0, \quad \hat{\hat{B}}_1 = i\left[\hat{\hat{l}}_+, \hat{\hat{l}}_-\right], \quad \hat{\hat{B}}_2 = -\left(\hat{\hat{l}}_+\left[\hat{\hat{l}}_-, \hat{\hat{l}}_0\right] + \hat{\hat{l}}_-\left[\hat{\hat{l}}_+, \hat{\hat{l}}_0\right]\right)$$

$$\hat{\hat{b}}_0 = 1, \quad \hat{\hat{b}}_1 = 0, \quad \hat{\hat{b}}_2 = \hat{\hat{l}}_+\hat{\hat{l}}_- + \hat{\hat{l}}_-\hat{\hat{l}}_+.$$

Inserting these coefficients in the equation of motion in (B.0.2) and returning to the original time $t = \frac{\tau}{\omega_I}$ one gets the Hamiltonian described in section 3.4.1.

Error analysis data for averaged Hamiltonian

The averaged Hamiltonian has been tested for a range of parameters. In summary, the absolute error is on the order of 10^{-3} or less, whereas the relative error is mostly below 1%. On occasions where the relative error rises above 1% the polarisation build up for the input parameters was very small, effectively yielding in a division by a very small number in the error calculation. Hence in some instances the relative error is large, even when the absolute deviation is still very small. Three different configurations were tested, hence convering different interaction strengths. In addition the pyramid configuration (see figure C.1) has been scaled, in order to account for stronger interactions. In the following sections the range of parameters tested and the incurred errors are presented. All the given errors are the largest errors over the time course of the simulation.

C.1 Pyramid

The configuration of the nuclei and electron is shown in figure C.1. The arrangement has been chosen to result in a range of interaction strengths. The electron is at the origin of the coordinate system, whereas spins I_1 and I_3 lie on the x axis

at coordinates $(l_1,0,0)$ and $(0,0,l_3)$, spins I_2 and I_4 on the y axis at $(0, l_2, 0)$ and $(0, l4,0)$. The fifth spin lies on the z axis at $(0,0,l_5)$. The coefficients l_i are given in the figure caption of C.1. The entire geometry is rotated around the x axis by 5deg. Keeping the following relaxation parameters fixed several microwave and
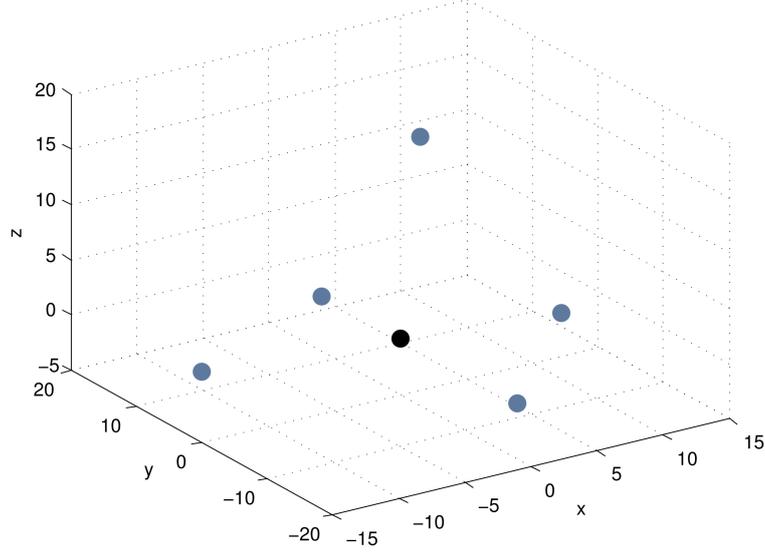
Figure C.1: Pyramid configuration. Axis units in Å. Nuclei are depicted in black, the electron in blue. $l_1=-l_2=12$ Å, $-l_4=l_5=18$ Åand $l_3=-15$ Å.

interaction strengths have been tested, which are summarised in table C.1.

$$r_{1e} = 10^3 \text{ Hz} \qquad r_{2e} = 10^6 \text{ Hz} \qquad r_{1n} = 10^{-2} \text{ Hz} \qquad r_{2n} = 10 \text{ Hz} \quad \text{(C.1.1)}$$

For a fixed ω_1 of 0.75 MHz the relaxation parameters have been varied. The corresponding errors are summarised in table C.2.

C.2   Chain

The chain contains nuclei five that are spaced 11.1 ± 1.6 Å apart. The nuclei have been chosen not to be exactly equidistant in order to have a slight variation in the coupling parameters. The initial relaxation time parameters used are:

$$r_{1e} = 10^3 \text{ Hz} \qquad r_{2e} = 10^6 \text{ Hz} \qquad r_{1n} = 10^{-2} \text{ Hz} \qquad r_{2n} = 10^3 \text{ Hz.} \quad \text{(C.2.1)}$$

Table C.1: Errors using the relaxation parameters given in (C.1.1). When indicated, the interaction parameters have been changed. The errors given are the largest error over the time course of the simulation

ω_1 in MHz	absolute error	relative error [%]
0.75	$8.43 \cdot 10^{-4}$	0.8
1.00	$8.54 \cdot 10^{-4}$	0.8
1.50	$9.40 \cdot 10^{-4}$	0.5
7.50	$1.98 \cdot 10^{-4}$	0.2
ω_1=1.5MHz		
interaction strengths scaled by factor 2	$1.60 \cdot 10^{-3}$	1.0
interaction strengths scaled by factor 8	$4.50 \cdot 10^{-3}$	4.2

Table C.2: Errors using relaxation parameters indicated in table. The highlighted terms have been changed with respect to the initial values from (C.1.1). ω_1=0.75 MHz and configuration the used is the initial configuration shown in figure C.1.

relaxation rates in Hz	absolute error	relative error [%]
$r_{1n} = 10^{-2}, r_{2n} = 10, r_{1e} = 10, r_{2e} = 10^6$	$2.50 \cdot 10^{-4}$	15.0
$r_{1n} = 10^{-2}, r_{2n} = 10, r_{1e} = 100, r_{2e} = 10^6$	$7.14 \cdot 10^{-4}$	5.4
$r_{1n} = 10^{-3}, r_{2n} = 10, r_{1e} = 10, r_{2e} = 10^6$	$3.03 \cdot 10^{-3}$	0.7
$r_{1n} = 10, r_{2n} = 10, r_{1e} = 10^3, r_{2e} = 10^6$	$8.75 \cdot 10^{-5}$	0.7
$r_{1n} = 10^{-2}, r_{2n} = 100, r_{1e} = 10, r_{2e} = 10^6$	$7.17 \cdot 10^{-4}$	0.6
$r_{1n} = 10^{-2}, r_{2n} = 1000, r_{1e} = 10, r_{2e} = 10^6$	$7.01 \cdot 10^{-4}$	0.3
$r_{1n} = 10^{-2}, r_{2n} = 10, r_{1e} = 10, r_{2e} = 10^4$	$8.42 \cdot 10^{-4}$	0.7
$r_{1n} = 10^{-2}, r_{2n} = 10, r_{1e} = 10, r_{2e} = 10^8$	$9.41 \cdot 10^{-4}$	1.1
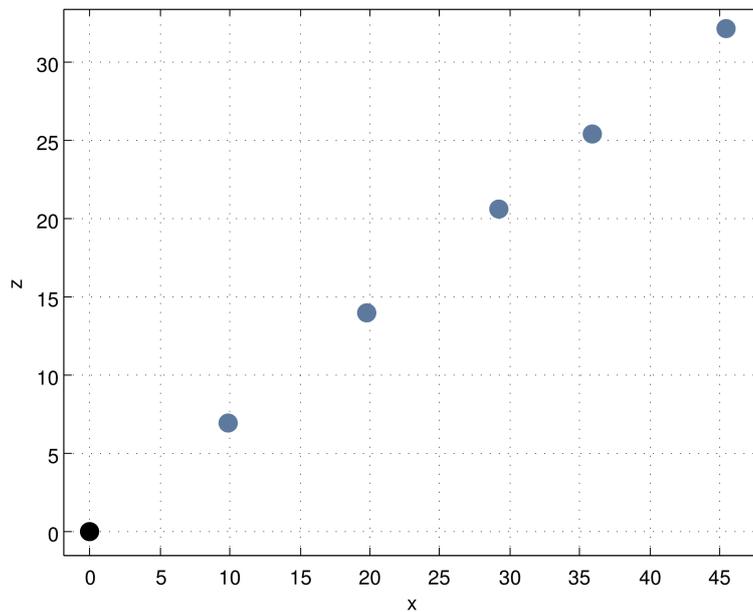
Figure C.2: Chain configuration. Axis units in Å. Nuclei are depicted in black, the electron in blue.

Using these parameters the following ω_1's were tested:

Table C.3: Errors using the relaxation parameters given in (C.2.1).

ω_1 in MHz	absolute error	relative error [%]
0.75	$4.93 \cdot 10^{-4}$	1.2
1.00	$4.84 \cdot 10^{-4}$	0.7
1.50	$3.82 \cdot 10^{-4}$	0.7

Additionally, for a fixed microwave power of ω_1=1.5 MHz the relaxation parameters given in table C.4 have been tested.

Table C.4: Errors using relaxation parameters indicated in table. The highlighted terms have been changed with respect to the initial values from (C.2.1). ω_1=1.5 MHz.

relaxation rates in Hz	absolute error	relative error [%]
$r_{1n} = 10^{-3}$, $r_{2n} = 10$, $r_{1e} =10$, $r_{2e} = 10^6$	$7.80 \cdot 10^{-5}$	0.7
$r_{1n} = 10^{-3}$, $r_{2n} = 10$, $r_{1e} =100$, $r_{2e} = 10^6$	$4.6 \cdot 10^{-4}$	0.7

C.3 Grid

The grid configuration is shown in figure C.3. Again several parameters have been tested and the associated errors are summarised in tables C.5 and C.6. In
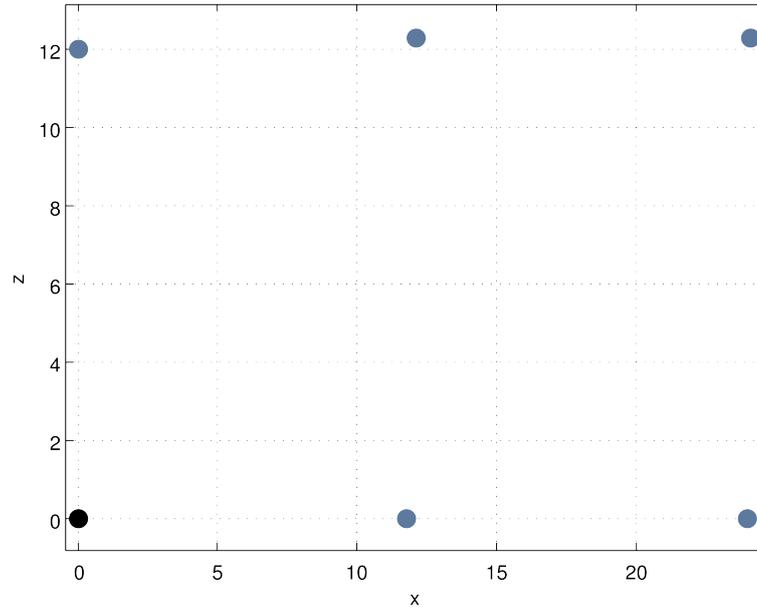
Figure C.3: Grid configuration. Axis units in Å. Nuclei are depicted in black, the electron in blue.

table C.5 the errors for simulations using the relaxation parameters from (C.2.1) and several values for ω_1 are listed. In table C.6 the errors for several relaxation parameters are listed, using a fixed microwave power of 1.5 MHz.

Table C.5: Errors using the relaxation parameters given in (C.2.1).

ω_1 in MHz	absolute error	relative error [%]
0.75	$1.80 \cdot 10^{-3}$	1.0
1.00	$1.90 \cdot 10^{-3}$	0.9
1.50	$1.90 \cdot 10^{-3}$	0.8
5	$7.91 \cdot 10^{-4}$	0.5

Table C.6: Errors using relaxation parameters indicated in table. The highlighted terms have been changed with respect to the initial values from (C.2.1). ω_1=1.5 MHz.

relaxation rates in Hz	absolute error	relative error [%]
$r_{1n} = 10^{-3}$, $r_{2n} = 10$, $r_{1e} = 10$, $r_{2e} = 10^6$	$5.94 \cdot 10^{-4}$	1.2
$r_{1n} = 10^{-3}$, $r_{2n} = 10$, $r_{1e} = 100$, $r_{2e} = 10^6$	$3.30 \cdot 10^{-3}$	1.13

Operators for the projection method

The operators for the projection method, $\hat{\mathscr{L}}_{ii}$ and $\hat{\mathscr{L}}_{ik}$, are obtained from the matrix representation of $\hat{\mathscr{L}}$ in the respective basis: $\langle \hat{O}_i | \hat{\mathscr{L}} | \hat{O}_j \rangle$. $\hat{O}_i$ and $\hat{O}_j$ are basis operators belonging to either the Zeeman order subspace $\mathfrak{L}_1$ or the non-Zeeman subspace $\mathfrak{L}_2$. For example if $i = 1$ and $j = 2$ one obtains a matrix element of $\hat{\mathscr{L}}_{12}$. As mentioned in 3.7 the basis of $\mathscr{L}_1$ is comprised of the operators $\{\hat{S}_z, \hat{I}_{1z}, \hat{I}_{2z}, \hat{I}_{1z}\hat{I}_{2z}...\}$, whereas the subspace $\mathscr{L}_2$ contains all other basis operators. When working with the averaged Hamiltonian, the basis of $\mathscr{L}_2$ contains only zero quantum coherence basis operators. Using the averaged Hamiltonian defined in 3.4.1 one gets the following matrix representations for the partitioned Liouvillian:

$$\hat{\mathscr{L}}_{11} = -diag\left(R'_1, r'_{11}, \ ...,r'_{1n}\right)$$

$$\text{with } R'_1 = R_1 + \frac{\omega_1^2}{\omega_I^2}\left(R_2 - R_1\right) \quad \text{and} \quad r'_{1k} = r_{1k} + \frac{|B_k|^2}{\omega_I}\left(R_1 + r_{2k} - r_{1k}\right)$$

$$k \in [1,n]$$

n is the number of nuclei in the sample.

$$\hat{\mathscr{L}}_{21} = \begin{pmatrix} Q \\ Q^* \end{pmatrix} \text{with } Q_{k1} = \frac{i\omega_1 B_{k+}}{4\omega_I} \quad \text{and} \quad Q_{k,k+1} = -\frac{i\omega_1 B_{k+}}{4\omega_I}$$

$$\hat{\hat{\mathcal{L}}}_{12} = (Q' \, Q'^*) \quad \text{with} Q_{k1} = \frac{i\omega_1 B_{k-}}{4\omega_I} \quad \text{and} \quad Q_{k,k+1} = -\frac{i\omega_1 B_{k-}}{4\omega_I}$$

$$\hat{\hat{\mathcal{L}}}_{22} = \begin{pmatrix} P & 0 \\ 0 & P^* \end{pmatrix}, \quad \text{with} P = diag(P_1, \dots, P_n).$$

the operators P_k are defined as

$$P_k = -R_2 - r_{2k} + i \sum_{j \neq k} A'_{jk} \hat{\hat{I}}_z, \quad \text{with} \quad A'_{jk} = A_j - 2d_{jk}$$

Bibliography

[1] M.H. Levitt. *Spin Dynamics, Basics of Nuclear Magnetic Resonance*. John Wiley and Sons, 2001.

[2] G. Bodenhausen, R.R. Ernst, and A. Wokaun. *Principles of NMR in One and Two dimensions*. Oxford University Press, Oxford, 1988.

[3] A. Abragam. *The Principles of Nuclear Magnetism*. Oxford University Press, 1961.

[4] M. Goldman. *Quantum Description of High-Resolution NMR in Liquids*. Oxford University Press, Oxford, 1988.

[5] J. Sakurai. *Modern Quantum Mechanics*. Addison-Wesley Publishing Company, Inc., 1994.

[6] R.A. Wind, M.J. Duijvestijn, C. van der Lugt, A. Manenschijn, and J. Vriend. Applications of dynamic nuclear polarization in ^{13}C- NMR in solids. *Prog. in NMR Spect.*, 17:33–67, 1985.

[7] I. Kuprov. Spin dynamics, Lecture notes, 2009. Oxford University.

[8] M. Mehring and V.A. Weberruß. *Object-Oriented Magnetic Resonance*. Academic Press, 2001.

[9] L. Di Bari and M. Levitt. The Homogeneous Master Equation and the Manipulation of Relaxation Networks. *Bull. Magn. Reson.*, 16(92):94–114, 1994.

[10] A Abragam and M Goldman. Principles of dynamic nuclear polarisation. *Rep. Prog. Phys.*, 41(2):395–467, 1978.

[11] http://www.bruker-biospin.com/av1000-dir.html, 2009.

[12] F. Bloch, W.N. Hansen, and M. Packard. Nuclear induction. *Phys. Rev.*, 69(127), 1946.

[13] E.M. Purcell, H.C. Torrey, and R.V. Pound. Resonance absorption by nuclear magnetic moments in solids. *Phys. Rev*, 69:37–68, 1946.

[14] A.W. Overhauser. Polarization of nuclei in metals. *Phys. Rev.*, 92(2):411–415, 1953.

[15] T.R. Carver and C.P. Slichter. Polarization of nuclear spins in metals. *Phys. Rev.*, 92(1):212–213, 1953.

[16] C.R. Bowers and D.P Weitekamp. Transformation of symmetrization order to nuclear-spin magnetization by chemical reaction and nuclear magnetic resonance. *Phys. Rev.*, 57(21):2645–2648, 1986.

[17] B.M. Goodson. Nuclear magnetic resonance of laser-polarized noble gases in molecules, materials, and organisms. *J. Magn. Reson.*, 155(2):157 – 216, 2002.

[18] I. Solomon. Relaxation processes in a system of two spins. *Phys. Rev.*, 99(2):559–565, 1955.

[19] K.H. Hausser and D. Stehlik. Dynamic nuclear polarisaton in liquids. *Adv. Magn. Reson.*, 3(79), 1968.

[20] K.-N Hu, S. Vikram, M. Rosay, and R.G. Griffin. High freqency dynamic nuclear polarisation using mixtures of TEMPO and trityl radicals. *J. Chem. Soc*, 126, 2007.

[21] C. Song, K.-N. Hu, T.M. Joo, C.-G.and Swager, and R.G. Griffin. TO-TAPOL: A biradical polarizing agent for dynamic nuclear polarization experiments in aqueous media. *J. Am. Chem. Soc.*, 128(35):11385–11390, 2006.

[22] K.-N. Hu, H.-h. Yu, T. M. Swager, and R.G. Griffin. Dynamic nuclear polarization with biradicals. *J. Am. Chem. Soc.*, 126(35):10844–10845, 2004.

[23] T. Guiberteau and D. Grucker. Dynamic nuclear polarization at very low magnetic fields. *Phys. Med. Biol.*, 43(7):1887–92, 1998.

[24] D.A. Farrar, C .T .and Hall, G.J. Gerfen, S.J. Inati, and R.G. Griffin. Mechanism of dynamic nuclear polarization in high magnetic fields. *J. Chem. Phys.*, 114(11):4922–4933, 2001.

[25] M. Goldman. *Spin Temperature and Nuclear Magnetic Resonance in Solids*. Oxford University Press, Oxford, 1970.

[26] F. Neese. ORCA - An ab initio, density functional and semiempirical program package. http://www.thch.uni-bonn.de/tc/orca/.

[27] M. Thaning. Free Radicals, 2000. U.S. Patent, No. 6,013,810.

[28] J. Granwehr, J. Leggett, and W. Köckenberger. A low-cost implementation of EPR detection in a dissolution DNP setup. *J. Magn. Reson.*, 187(2):266 – 276, 2007.

[29] V. Denysenkov, M.J. Prandolini, A. Krahn, M. Gafurov, B. Endeward, and T.F. Prisner. High-field DNP spectrometer for liquids. *Appl. Magn. Reson*, 34(3-4):289–299, 2008.

[30] V. Denysenkov, M.J. Prandolini, M. Gafurov, D. Sezer, B. Endeward, and T.F. Prisner. Liquid state DNP using a 260 GHz high power gyrotron. *Phys. Chem. Chem. Phys.*, 12(22):5786–5790, 2010.

[31] M. Reese, D. Lennartz, T. Marquardsen, P. Höfer, A. Tavernier, P. Carl, T. Schippmann, M. Bennati, T. Carlomagno, F. Engelke, and C. Griesinger. Construction of a liquid-state NMR DNP shuttle spectrometer: First experimental results and evaluation of optimal performance characteristics. *Appl. Magn. Reson*, 34(3-4):301–311, 2008.

[32] A. Krahn, P. Lottmann, T. Marquardsen, A. Tavernier, M.-T. Turke, A. Reese, M.and Leonov, M. Bennati, P. Höfer, F. Engelke, and C. Griesinger. Shuttle DNP spectrometer with a two-center magnet. *Phys. Chem. Chem. Phys.*, 12(22):5830–5840, 2010.

[33] M. Rosay, V. Weis, K.E. Kreischer, R.J. Temkin, and R.G. Griffin. Two-dimensional ^{13}C-^{13}C correlation spectroscopy with magic angle spinning and dynamic nuclear polarization. *J. Am. Chem. Soc.*, 124(13):3214–3215, 2002.

[34] M. Rosay, J.C. Lansing, K.C. Haddad, W.W. Bachovchin, J. Herzfeld, R.J. Temkin, and R.G. Griffin. High-frequency dynamic nuclear polarization in MAS spectra of membrane and soluble proteins. *J. Am. Chem. Soc.*, 125(45):13626–13627, 2003.

[35] C.-G. Joo, K.-N. Hu, J.A. Bryant, and R.G. Griffin. In situ temperature jump high-frequency dynamic nuclear polarization experiments: Enhanced sensitivity in liquid-state NMR spectroscopy. *J. Am. Chem. Soc.*, 128(29):9428–9432, 2006.

[36] C.-G. Joo, A. Casey, C.J. Turner, and R.G. Griffin. In situ temperature-jump dynamic nuclear polarization: Enhanced sensitivity in two dimensional ^{13}C-^{13}C correlation spectroscopy in solution. *J. Am. Chem. Soc.*, 131(1):12–13, 2009.

[37] J.H. Ardenkjær-Larsen, B. Fridlund, A. Gram, G. Hansson, L. Hansson, M.H. Lerche, R. Severin, M. Thaning, and K. Golman. Increase in signal-

to-noise ratio of > 10,000 times in liquid-state NMR. *Proc. Nat. Acad. Sci. U.S.A.*, 100(18):10158–10163, 2003.

[38] H. Zeng, Y. Lee, and C. Hilty. Quantitative rate determination by dynamic nuclear polarization enhanced NMR of a Diels-Alder reaction. *Anal. Chem.*, 82(21):8897–8902, 2010.

[39] C. Hilty and S. Bowen. Applications of dynamic nuclear polarization to the study of reactions and reagents in organic and biomolecular chemistry. *Org. Biomol. Chem.*, 8(15):3361–3365, 2010.

[40] S. Meier, M. Karlsson, P.R. Jensen, M. H. Lerche, and J.O. Duus. Metabolic pathway visualization in living yeast by DNP-NMR. *Mol. BioSyst.*, 7(10):2834–2836, 2011.

[41] K. Golman, R. in't Zandt, M. Lerche, R. Pehrson, and J.H. Ardenkjær-Larsen. Metabolic imaging by hyperpolarized ^{13}C magnetic resonance imaging for in vivo tumor diagnosis. *Cancer Res.*, 66(22):10855–10860, 2006.

[42] A. Hu, S.and Balakrishnan, R Bok, B. Anderton, P.E. Z. Larson, S.J. Nelson, J. Kurhanewicz, D.B. Vigneron, and A. Goga. ^{13}C-Pyruvate Imaging Reveals Alterations in Glycolysis that Precede c-Myc-Induced Tumor Formation and Regression. *Cell Metab.*, 14(1):131–142, 2011.

[43] F.A. Gallagher, M.I. Kettunen, S.E. Day, D. Hu, J.H. Ardenkjær-Larsen, R. in't Zandt, P.R. Jensen, M. Karlsson, K. Golman, M.H. Lerche, and K.M. Brindle. Magnetic resonance imaging of pH in vivo using hyperpolarized ^{13}C-labelled bicarbonate. *Nature*, 453:940–943, 2008.

[44] I. Park, P.E. Z. Larson, M.L. Zierhut, S. Hu, R. Bok, T. Ozawa, J. Kurhanewicz, D.B. Vigneron, S.R. Van den Berg, C. D. James, and S. J. Nelson. Hyperpolarized ^{13}C magnetic resonance metabolic imaging: application to brain tumors. *Neuro-Oncology*, 12(2):133–144, 2010.

[45] D.M. Wilson, K.R. Keshari, P.E.Z. Larson, A.P. Chen, S. Hu, M. Van Criekinge, R. Bok, S.J. Nelson, Macdonald J.M., D.B. Vigneron, and J. Kurhanewicz. Multi-compound polarization by DNP allows simultaneous assessment of multiple enzymatic activities in vivo. *J. Magn. Reson.*, 205(1):141 – 147, 2010.

[46] R. Leggett, J.and Hunter, R. Granwehr, J.and Panek, A.J. Perez-Linde, A.J. Horsewill, J. McMaster, G.M. Smith, and W. Köckenberger. A dedicated spectrometer for dissolution DNP NMR spectroscopy. *Phys. Chem. Chem. Phys.*, 12(22):5883–5892, 2010.

[47] R. Panek, J. Granwehr, J.and Leggett, and W. Köckenberger. Slice-selective single scan proton COSY with dynamic nuclear polarisation. *Phys. Chem. Chem. Phys.*, 12(22):5771–5778, 2010.

[48] L. Frydman, A. Lupulescu, and T. Scherf. Principles and features of single scan two dimensional NMR spectroscopy. *J. Am. Chem. Soc.*, 125:9204–9217, 2003.

[49] L. Frydman and D. Blazina. Ultrafast two-dimensional nuclear magnetic resonance spectroscopy of hyperpolarized solutions. *Nat. Phys.*, 3(6):415–419, 2007.

[50] N.S. Andersen and W. Köckenberger. A simple approach for phase-modulated single-scan 2D NMR spectroscopy. *Magn. Reson. Chem.*, 43:795–797, 2005.

[51] F.A. Gallagher, M.I. Kettunen, D. Hu, P.R. Jensen, R. in 't Zandt, M. Karlsson, S.J. Gisselsson, A.and Nelson, T.H. Witney, S.E. Bohndiek, G. Hansson, T. Peitersen, M.H. Lerche, and K.M. Brindle. Production of hyperpolarized $[1,4-^{13}C_2]$ malate from $[1,4-^{13}C_2]$ fumarate is a marker of cell necrosis and treatment response in tumors. *P.N.A.S.*, 106(47):19801–19806, 2009.

[52] M.I. Kettunen, D. Hu, T.H. Witney, R. McLaughlin, F.A. Gallagher, S.E. Bohndiek, S.E. Day, and K.M. Brindle. Magnetization transfer measurements of exchange between hyperpolarized [1-^{13}C] pyruvate and [1-^{13}C] lactate in a murine lymphoma. *Magn. Reson. Med.*, 63(4):872–880, 2010.

[53] R.I. Hunter, P.A.S. Cruickshank, D.R. Bolton, P.C. Riedi, and G.M. Smith. High power pulsed dynamic nuclear polarisation at 94 GHz. *Phys. Chem. Chem. Phys.*, 12(22):5752–5756, 2010.

[54] N. Pomplun and S.J. Glaser. Exploring the limits of electron-nuclear polarization transfer efficiency in three-spin systems. *Phys. Chem. Chem. Phys.*, 12(22):5791–5798, 2010.

[55] Y. Hovav, A. Feintuch, and S. Vega. Dynamic nuclear polarization assisted spin diffusion for the solid effect case. *J. Chem. Phys.*, 134(7), 2011.

[56] Y. Hovav, A. Feintuch, and S. Vega. Theoretical aspects of dynamic nuclear polarization in the solid state - the solid effect. *J. Magn. Reson.*, 207(2):176 – 189, 2010.

[57] R. Bruschweiler and R.R. Ernst. A cog-wheel model for nuclear-spin propagation in solids. *J. Magn. Reson.*, 124(1):122–126, 1997.

[58] I. Kuprov, N. Wagner-Rundell, and P.J. Hore. Polynomially scaling spin dynamics simulation algorithm based on adaptive state-space restriction. *J. Magn. Reson.*, 189(2):241 – 250, 2007.

[59] H.J. Hogben, M. Krzystyniak, G.T.P. Charnock, P.J. Hore, and Ilya Kuprov. Spinach - A software library for simulation of spin dynamics in large spin systems. *J. Magn. Reson.*, 208(2):179 – 194, 2011.

[60] M.C. Butler, J.-N. Dumez, and L. Emsley. Dynamics of large nuclear-spin systems from low-order correlations in Liouville space. *Chem. Phys. Lett.*, 477(4-6):377–381, 2009.

[61] J.-N. Dumez, M.C. Butler, and L. Emsley. Numerical simulation of free evolution in solid-state nuclear magnetic resonance using low-order correlations in Liouville space. *J. Chem. Phys.*, 133(22), 2010.

[62] A. Karabanov, I. Kuprov, G. Charnock, A. van der Drift, L. Edwards, and W. Köckenberger. On the accuracy of the state space restriction approximation for spin dynamics simulations. *J. Chem. Phys.*, 135(8), 2011.

[63] N. Bloembergen, E.M. Purcell, and R.V. Pound. Relaxation Effects in Nuclear Magnetic Resonance Absorption. *Phys.Rev.*, 73(7):679–712, 1948.

[64] M.H. Levitt and L. Di Bari. Steady state in magnetic resonance pulse experiments. *Phys. Rev. Lett.*, 69(21):3124–3127, 1992.

[65] I. Kuprov. Diagonalization-free implementation of spin relaxation theory for large spin systems. *J. Magn. Reson.*, 209(1):31 – 38, 2011.

[66] A. Karabanov, A. van der Drift, Edwards L., I. Kuprov, and W. Köckenberger. Quantum mechanical simulation of solid effect dynamic nuclear polarisation using Krylov-Bogolyubov time averaging and a restricted state-space. Submitted for publication., 2011.

[67] N.M. Krylov and N.N. Bogoliubov. *Introduction to non-linear mechanics.* Princetone University Press, 1947.

[68] U. Haeberlen and J.S. Waugh. Coherent averaging effects in magnetic resonance. *Phys.Rev.*, 175(2):453–467, 1968.

[69] N. Vijayasarathi, Y. Hovav, A. Feintuch, S. Vega, and Goldfarb. D. EPR detected polarization transfer between Gd^{3+} and protons at low temperature and 3.3 T: The first step of dynamic nuclear polarization. *J. Chem. Phys.*, 132(21):214504–214516, 2010.

[70] J.-N. Dumez, M.C. Butler, E. Salager, B. Elena-Herrmann, and L. Emsley. Ab initio simulation of proton spin diffusion. *Phys. Chem. Chem. Phys*, 12(32):9172–9175, 2010.

[71] E. MacNamara, T. Hou, G. Fisher, S. Williams, and D. Raftery. Multiplex sample NMR: an approach to high-throughput NMR using a parallel coil probe. *Anal. Chim. Act.*, 395:9–6, 1999.

[72] G. Fisher, C. Petucci, E. MacNamara, and D. Raftery. ^{13}C NMR probe for the simultaneous acquisition of multiple samples. *J. Magn. Reson.*, 138:160–163, 1999.

[73] H. Wang, L. Ciobanu, and A. Webb. Reduced data acquisition time in multi-dimensional nmr spectroscopy using multiple-coil probes. *J. Magn. Reson.*, 173(1):134 – 139, 2005.

[74] M. Poole and R. Bowtell. Volume parcellation for improved dynamic shimming. *Magn. Reson. Mat. Phys. Biol. Med.*, 21(1):31–40, 2008.

[75] A. Haase, J. Frahm, D. Matthaei, W. Hanicke, and K.-D Merboldt. FLASH imaging. rapid NMR imaging using low flip-angle pulses. *J. Magn Reson.*, 67(2):258 – 266, 1986.

[76] P. Mansfield. Spatial mapping of the chemical shift in NMR. *Magn. Reson. Med.*, 1(3):370–386, 1984.

[77] H. Zeng, S. Bowen, and C. Hilty. Sequentially acquired two-dimensional NMR spectra from hyperpolarized sample. *J. Magn. Reson.*, 199(2):159–165, 2009.